Measurements of the Ratio of W and Z Production and the W Boson Decay Width at CDF

by

Katherine Ann Copic

A dissertation submitted in partial fulfillment
of the requirements for the degree of
Doctor of Philosophy
(Physics)
in The University of Michigan
2007

Doctoral Committee:

Professor Myron K. Campbell, Chair
Professor Christopher R. Monroe
Professor Jianming Qian
Associate Professor Peter E. Van Keken
Assistant Professor Leopoldo A. Pando Zayas

ABSTRACT

Measurements of the Ratio of W and Z Production

and the W Boson Decay Width at CDF

by

Katherine Ann Copic

Chair: Myron K. Campbell

We present a new method of measuring the ratio of W and Z production and decay (R) at the CDF experiment. We analyze 307 pb^{-1} of proton-antiproton collisions at the Fermilab Tevatron center-of-mass energy of 1.96 TeV.

A single sample containing both W and Z boson candidates is selected by requiring at least one high-energy electron in an event with low hadronic activity. We estimate that less than one percent of our sample is made up of background events after a cut on the recoil energy. A maximum likelihood fit is performed on the missing transverse energy spectrum of the events to determine the relative rates of W and Z production in the common sample. This ratio is defined as:

$$\mathsf{R} = \frac{\sigma_W \cdot Br(W \to \ell\nu)}{\sigma_Z \cdot Br(Z \to \ell\ell)} = \frac{\sigma_W}{\sigma_Z} \frac{\Gamma(W \to \ell\nu)}{\Gamma(W)} \frac{1}{Br(Z \to \ell\ell)}$$

We have obtained the first result using this method for the electron channel.

$$\mathsf{R} = 10.55 \pm 0.09(\text{stat}) \pm 0.12(\text{syst})$$

We then extract the Branching Ratio of $W \to \ell\nu$ using the Branching Ratio of $Z \to \ell^+\ell^-$ measured at LEP and a theoretical value for the ratio of the cross sections.

$$Br(W \to \ell\nu) = \mathsf{R} \cdot \frac{\sigma_Z}{\sigma_W} Br(Z \to \ell^+\ell^-) = 0.1054 \pm 0.0016$$

We also obtain an indirect measurement of the W width of $\Gamma_W^{\text{tot}} = 2148 \pm 32$ MeV. This width gives us information about all the possible decays of the W boson. The

W width also constrains the sum of the CKM elements involved in W decays. We find the following value for V_{cs} , the least constrained element: $|V_{cs}| = 1.008 \pm 0.029$.

"The Standard Model has not come from a sudden inspirational flash of brilliance, be it in the bath or elsewhere! Instead it is a compact summary of experimental facts and theoretical ideas. It has taken the painstaking work of many thousands of researchers, both experimenters and theorists, over several decades to achieve the form of the model that we know today." – Peter Renton [32]

for spoons

Acknowledgments

The work in this thesis was supported by many people.

Without the decades of work by the people at CDF, Fermilab, and the Tevatron, there would be no data to analyze. Within the CDF collaboration, I have been fortunate to work with the University of Michigan group with Myron Campbell, Dave Gerdes, Dan Amidei, J. Chapman, Monica Tecchio, Ken Bloom, Claudio Ferretti, Stephen Miller, Tom Wright, Jon Ameel, Nate Goldschmidt, Fred Niell, Alexei Varganov, Mitchell P. Soderberg, Bo Jayatilaka, Tom Schwarz, and Clark Cully. Jim Degenhardt feels like an honorary member of the Michigan House – even if he was on D0. Special thanks go, of course, to Myron for all of his time and patience with me, trying to keep me focused as I organized picnics and took off to Washington DC with the Fermilab GSA. When I'm working in physics in the future, I will hear Myron saying "What is the interesting *physics* here?" and Dan saying "Look at the *data*!"

Also on CDF, Michael Schmitt (at Northwestern) and Victoria Martin (at Edinburgh) began work on the "shape method" and took me on as a collaborator. They both spent late nights working and thinking about this analysis with me, and I learned a lot from them.

The Electroweak group and W/Z subgroup were always good places to bounce ideas around. In addition to Michael and Victoria, Aidan Robson, David Dagenhart, Pasha Murat, David Waters, Chris Hays, and Eric James and Eva Halkiadakis were contributors to those groups, whose input I always valued.

Writing a thesis is not as easy as you might think. Fortunately, I had many good examples. Thanks to Doctors Canelli, Gerberich, Goldschmidt, Jayatilaka, Hahn,

Hamilton, Kirby, Manca, Ray, Robson, Varganov, Veramendi, and Whiteson. At least one person has actually looked at your theses!

There are also the people who helped to get me into physics in the first place. Professor Tye at Cornell showed a picture of the CESR ring in an introductory physics class – that got me interested in particle physics. Nari Mistry, Yulin Li, and Lawrence Gibbons hired me to work on physics for the first time. Many other Cornell professors, including Joe Rogers, were very encouraging as I switched into physics late in my undergraduate career. Jay Marx introduced me to Natalie Roe and Bob Cahn, who helped get me started with analysis at LBNL, along with the rest of the Berkeley Babar group, especially Mandeep S. S. Gill, Chris LeClerc, and Christian Wilson. Dan Huttenlocher, though not a physicist, has always been a valued academic, snowboarding, restaurant, and general life advisor.

Living in many places, I have been able to meet many amazing people. Who knows what life would be like without the friends I made at Risley, McFaddin, and Westbourne in Ithaca, at LBNL and iMarkets in SF, in the fantastic Rainbow Palace in Ann Arbor, hanging out with the cronies and the Fermiserious, at the epic Michigan House, with the Fermi Dinner Club, on the Isotopes softball team, at the Ramford House in Chicago, and at CMU and D's Six Pax in Pittsburgh. Alright everyone, let's all move to the same place now. How's Geneva, Switzerland?

I also thank my whole big, crazy family: my mother Cyndi and my father John, Steve and Eileen, John and Candace and Isabella, Liz, Steve and Caity and Ashley, my grandparents John and Ann, and Gene and Ann, and all the rest of the Coleman, Copic, Morse, Proctor, Casinelli, Brown, Wasko, Snyder, Penix, Lennington, Robertson, Ray, Kundstader, O'Laughlin, Fassanella, and Spoonhower families! Love goes to all of them, and to spoons, with whom I look forward to many more adventures.

CONTENTS

LIST OF FIGURES

Figure

LIST OF TABLES

Table

CHAPTER 1

Introduction

The study of physics includes some of the most basic questions in science. What is matter? How does it work? What are the smallest pieces of matter? How do those small pieces interact? Many observations must be brought together to find the answers to these questions. Patterns emerge, and new kinds of matter and new physical laws are discovered and verified.

1.1 Patterns Lead to Knowledge

One well-known pattern that led to a new understanding of matter is the periodic table of elements. Elements were organized in order of increasing masses, grouping those with similar properties into the same column (Figure 1.1). The last column of the table contains the unreactive elements known as the "Noble gases," while the first column contains the very reactive Alkali metals. As elements fell into place in the rows and columns, it became clearer that the periodic table displayed information about the internal structure of the atoms.

The discoveries of the protons, neutrons, and electrons inside the atom helped solve the puzzle. The elements are ordered according to the number of protons in each element, and the atomic weight is made up almost entirely of the weights of the protons and neutrons. To predict the positions of the elements in the columns, however, knowing the constituent particles is not enough. The interactions and rules governing the electrons determine the columns. Now, students learn that the Noble

gases are unreactive because their electron shells are completely full, while the Alkali metals have one electron too many to be stable. Learning which particles exist and how they interact are both important parts of developing a complete theory.

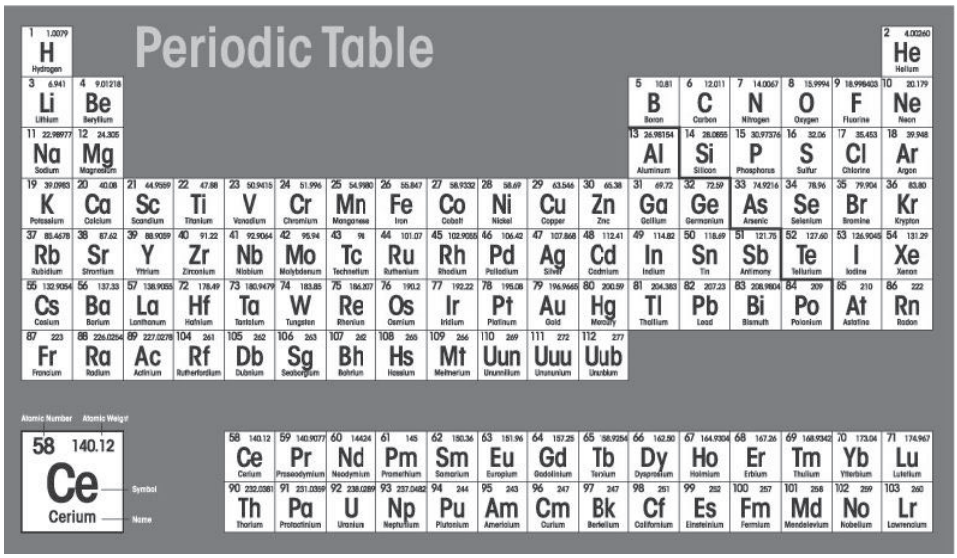

Figure 1.1. The structure of the Periodic Table of the Elements reveals information about the elements' structure and physical laws.

A similar puzzle emerged in the 1950's, when a zoo of seemingly fundamental particles appeared as experiments reached new energy scales. Physicists assembled geometric solids of related particles according to their mass, electric charge and their "strangeness" (Figure 1.2). These structures could be explained using the hypothesis that protons, neutrons, and other particles like them are made of even smaller fundamental parts called quarks. Experimental evidence has verified the existence of quarks over the last 50 years, and new rules governing the interactions of quarks have helped explain how they form larger objects, like the proton.

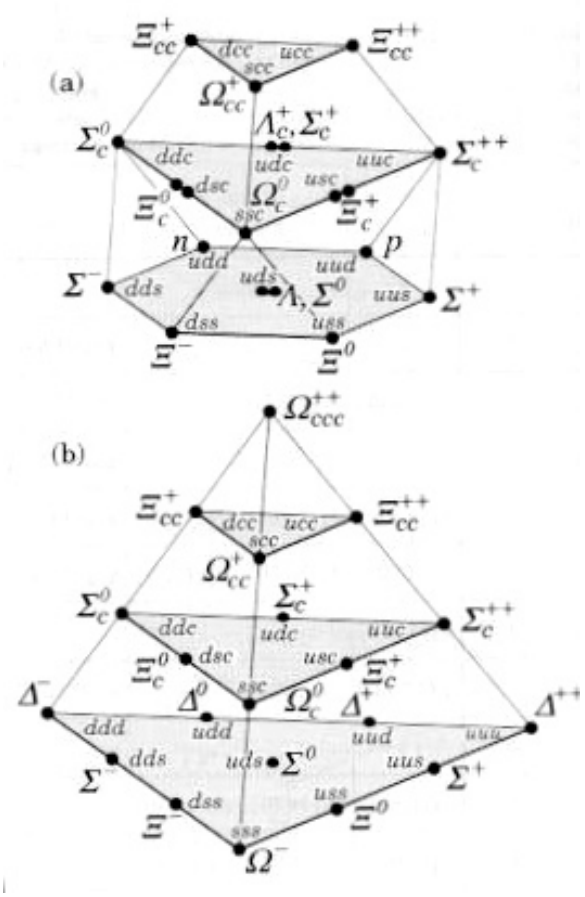

Figure 1.2. The vertices on these diagrams are all different particles, with their quark makeup written on the interior. The proton (p) is on the bottom hexagon of figure (a), with uud quarks as its components. The neutron (n) is to the left of the proton. The particles are organized by electric charge (-2, -1, 0, +1, +2), strangeness (0, 1, 2, or 3 strange quarks), and charm (0, 1, 2, or 3 charm quarks).

1.2 Mysteries in Particle Physics

1.2.1 Three Generations of Matter and Antimatter

Mysterious patterns still exist in the world of particle physics, inspiring future research.

Everyday matter is made of protons and neutrons, which are each made of up and down quarks. Four more types of quarks have been produced and studied in high-energy physics experiments (Figure 1.3). The up, charm, and top quarks are like copies of one another, except for their differing masses. The same pattern repeats for the down, strange, and bottom quarks.

A similar situation exists for the electron. Two heavier particles, the muon and tau, mirror the properties of the electron. There are also very light partners for each of these three: an electron neutrino, a muon neutrino, and a tau neutrino. Because these six particles are not as heavy as the objects made from quarks, they are called "leptons," from the Greek word for "light."

The up quark, down quark, electron and neutrino are all repeated three times in nature, but no experimental evidence has been found to show why. Moreover, the masses of the particles span a huge range (Table 1.1), for which no one has determined an underlying cause. There is also no clear connection between the first set of quarks (the up and down) and the first set of leptons (the electron and electron neutrino).

In addition to all of these types of matter particles, there are antimatter partners for each quark and lepton. The antiparticles have the same masses as the particles but opposite charges. The existence of antimatter is not puzzling; it was incorporated into the theory before it was even discovered. The overall *scarcity* of antimatter in the universe, however, remains unexplained. The current understanding of matter and its interactions, called the Standard Model, predicts almost equal amounts of matter and antimatter in the universe, but almost no antimatter has been observed. Some small differences in the way that matter and antimatter are treated have been found and accommodated theoretically, but the small deviations are not enough to explain the matter-antimatter asymmetry seen today.

1.2.2 Forces' Unsolved Problems

The study of the matter particles is only half the story, however; particles are also associated with each force. While it can be useful to think of a force as a field, like a magnetic field, the field can be quantized into small units that are particle transmitting the force.

All the physical processes known today are described using three forces. These

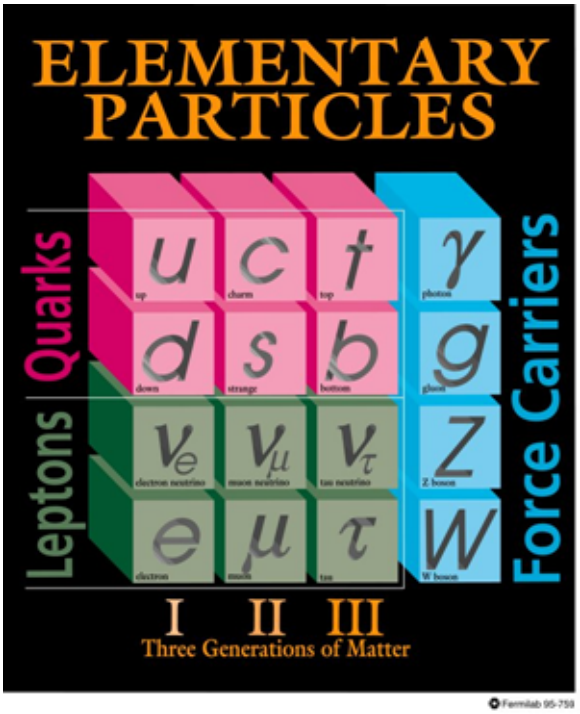

Figure 1.3. The smallest units of matter known today are quarks, leptons, and the force-carrying particles.

forces act on a microscopic level, but they have macroscopic effects. Gravity pulls matter together, and it acts on any particles with mass. The strong force is responsible for holding the nuclei of atoms together. Without it, atoms could not exist. The third force, the electroweak force, has many effects including electricity, magnetism, and the decay of atomic nuclei. Each of these forces has associated force-carrying particles.

Gravity is a very important force when predicting the behavior of an object with a large mass, like an entire galaxy, but in the small world of particle physics, gravity is completely overwhelmed by the other forces. Because of its small effect, laws of gravity can not usually be tested in particle physics experiments. New theories that predict large gravitational effects can sometimes be examined, such as those with large extra dimensions. The main problem with gravity is that its description in general relativity is irreconcilable with quantum mechanics, which describes the rest of the forces. Furthermore, quanta of the gravitational field, gravitons, have not yet

been observed.

The strong force is more difficult to see in everyday life than gravity, but it is the essential glue that holds together the nuclei of atoms. If all the protons in a nucleus are positively charged, and the neutrons have no charge, why does the nucleus stay bound together? The protons and neutrons are held in the nucleus by the same force that binds quarks together to form protons and neutrons. The quarks each have a different strong charge that attracts them to one another, similar to the way that opposite electrical charges attract. While there are two kinds of electric charge (positive and negative), the strong force has six kinds of charge: red, blue, and green, anti-red, anti-blue, and anti-green. The particles themselves are not actually colored; the choice of colored names for the charges was made in reference to light. As +1 and -1 combine to yield 0, red, blue, and green light combine to form white light. A color-neutral particle can be formed with one red, green, and blue object, or with a color and its anti-color (red and anti-red, for example). The strong force's carrier particle is whimsically named the gluon because of its role in the nucleus. A central question regarding the strong force is that of "quark confinement." Quarks have never been observed alone, but no proof that they are confined to quark-antiquark or three quark particles yet exists. Experimental observations and theoretical developments of the strong force are still underway.

The electroweak force is conceptually more complicated than gravity and the strong force, because it contributes to many different types of macroscopic processes. Part of the complication is that it has several kinds of force-carrying particles. The photon carries the electromagnetic force, while the W^+, W^-, and Z are responsible for processes of decay. Electricity and magnetism were considered separate phenomena, until they were united mathematically in the 1860's in Maxwell's equations. This formulation combined the two processes into electromagnetic waves and gave more insight than looking at either one alone. Nearly 100 years later, in the 1960's, the

electromagnetic and weak forces were unified in a theoretical framework by Glashow, Weinberg, and Salam. [24, 41, 34] The unification required a new field that allows the W and Z to be very massive, while the photon remains massless. The new field is the "Higgs" field, and it should also have an associated particle called the Higgs boson. Many questions remain about the electroweak unification and the Higgs. Despite its prediction, the Higgs particle has not yet been observed, and the theory does not explain why particles have the curious range of masses that they do (see Table 1.1).

1.3 Searching for Answers

These big questions about the properties of matter are answered with many measurements over time, filling in the types of particles, how they are produced, how they decay, how they attract and repel one another. With all this information, patterns of charges, masses, and interactions can lead to a deeper understanding of nature.

Making observations of atoms and their constituents can be difficult because they are so small. If a microscope could be used, the object of interest would be hit with light (a stream of photons) and the light would bounce off the target and be reflected into the viewer's eye. With dim light, a low-quality image would be available, but with a good amount of light and a lens to focus it, more detail could be observed. The quarks that make up protons and neutrons are too small to be seen with the best microscopes, but scientists can examine the atom in a similar way.

Particle physicists want to look inside very small areas, so they use a more powerful probe than a light beam. In many kinds of experiments, a beam of particles (electrons or protons, for example) is created, accelerated a to high energy, then bombarded onto a target.[1] The beam of particles interacts with the target and the particles are affected by the collision. Experimentalists build a detector to capture the outgoing particles,

[1]Particle physics is also called "high-energy physics" because of this use of a high-energy beam of particles to look inside matter.

like the eye captures and analyzes the beam of light reflecting off of a sample in a microscope.

Other experiments collide two beams of particles into one another, rather than hitting a target with one beam. When the two beams are made of matter and antimatter, sometimes the quarks and antiquarks collide. The energy of the collision includes all of the kinetic energy that the two incoming particles had, and all of the energy in their masses given by $E = mc^2$. It quickly condenses into new pairs of particles and antiparticles that travel outwards from the point of collision. Although some particles are destroyed and new particles are created in these interactions, energy and momentum are conserved at all times. The detector built around the collision point in this case captures some particles from the beams, but it also captures new particles made from the matter-antimatter energy (Figure 1.4). Looking at the outgoing particles reveals a wealth of information about the things that can be produced and their properties.

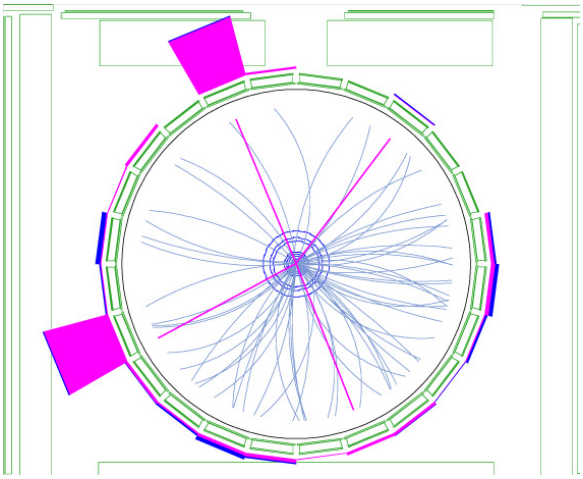

Figure 1.4. When protons and antiprotons collide in the center of the CDF experiment at Fermilab, information about the outgoing particles is recorded. The detector is shown in cross-section here. The beams collide in the center of the circles. Tracks show the paths of the outgoing particles. The pink and blue rectangles around the outside have heights proportional to the amount of energy collected in corresponding pieces of a calorimeter. The CDF apparatus, including tracking and calorimetry is described in detail in Section 2.2.

At Fermi National Accelerator Laboratory in the United States, the highest energy

man-made collisions in the world are taking place. Beams of protons and antiprotons collide every 396 nanoseconds, and two huge detectors measure of the spray of outgoing particles. These data help particle physicists explore the difficult problems and curious patterns outlined in the previous pages.

In this thesis, the production and decay of the electroweak force carriers, the W and Z particles, will be examined. Measurements of their properties help define some of the basic parameters of the Standard Model of particle physics, taking small steps towards answering some of these big questions.

Name	Electric Charge	Weak Isospin	Strong Charge	Mass
Quarks				
up	+2/3	+1/2	C	1.5 to 3.0 MeV/c^2
down	-1/3	-1/2	C	3 to 7 MeV/c^2
charm	+2/3	+1/2	C	1.25 ± 0.09 GeV/c^2
strange	-1/3	-1/2	C	95 ± 25 MeV/c^2
top	+2/3	+1/2	C	174.2 ± 3.3 GeV/c^2
bottom	-1/3	-1/2	C	4.2 ± 0.07 GeV/c^2
Leptons				
electron	-1	-1/2	0	0.51099892 ± 0.00000004 MeV/c^2
electron neutrino	0	+1/2	0	< 2 eV/c^2
muon	-1	-1/2	0	105.658369 ± 0.000009 MeV/c^2
muon neutrino	0	+1/2	0	< 0.19 MeV/c^2
tau	-1	-1/2	0	$1776.99^{+0.29}_{-0.26}$ MeV/c^2
tau neutrino	0	+1/2	0	< 18.2 MeV/c^2
Force-Carrying Particles				
photon	0	0	0	0
W^+	+1	+1	0	80.403 ± 0.029 GeV/c^2
Z	0	+1	0	91.1876 ± 0.0021 GeV/c^2
gluon	0	0	$C\overline{C}'$	0
graviton *	0	0	0	0
Higgs *	0	0	0	> 114 GeV/c^2
* Not yet observed				

Table 1.1. The indivisible units of matter [39]. The electric charge and mass of particles are familiar concepts, while the others need some explanation. The weak isospin shows how particles interact with the W and Z. It only pertains to the left-handed particles, as explained in Chapter 3. There are six kinds of strong charge: red, blue, green, anti-red, anti-blue, and anti-green. Quarks each have a charge of one color (red, for example) while gluons carry a charge of one color and anti-color, denoted here as $C\overline{C}'$ (*e.g.* red and anti-blue). There is not a strict correspondence between a particular quark type (up, down, charm) and a particular color (red, green, blue). Each quark can have any of the colors. All the other particles are neutral to the strong force. For every type of particle shown, there exists an antiparticle with equal mass and opposite charges and isospin.

CHAPTER 2

Experimental Apparatus

The Fermi National Accelerator Laboratory (Fermilab) is located near Batavia, Illinois. Fermilab was created in 1967 as a center in the United States for basic science research [42].

Fermilab hosts an accelerator complex that creates beams of particles and delivers them to many different experiments. There are two large experiments: CDF and DØ, with over 600 physicists working on each. Both CDF and DØ scientists study a wide range of physics topics including measurements of known matter particles and the fundamental forces, as well as searches for new particles and phenomena. Fermilab also runs the smaller MiniBoone and MINOS experiments, which study the properties of neutrinos. Astrophysicists there study the nature of space, cosmic rays, dark matter, and other components of the universe. They use observations from the Pierre Auger Cosmic Ray Observatory, the Cryogenic Dark Matter Search, and Sloan Digital Sky Survey. Theorists resident at Fermilab define and explore the models of the universe's largest and smallest components.

Fermilab also contributes to projects taking place at CERN, the largest European laboratory of particle physics. At CERN, the Large Hadron Collider begins operation soon near Geneva, Switzerland. Fermilab is contributing to this accelerator, as well as one of the major experiments (the CMS detector). Planning for the future, Fermilab is involved in research and development for new projects, including an accelerator that would collide electrons and positrons called the International Linear Collider.

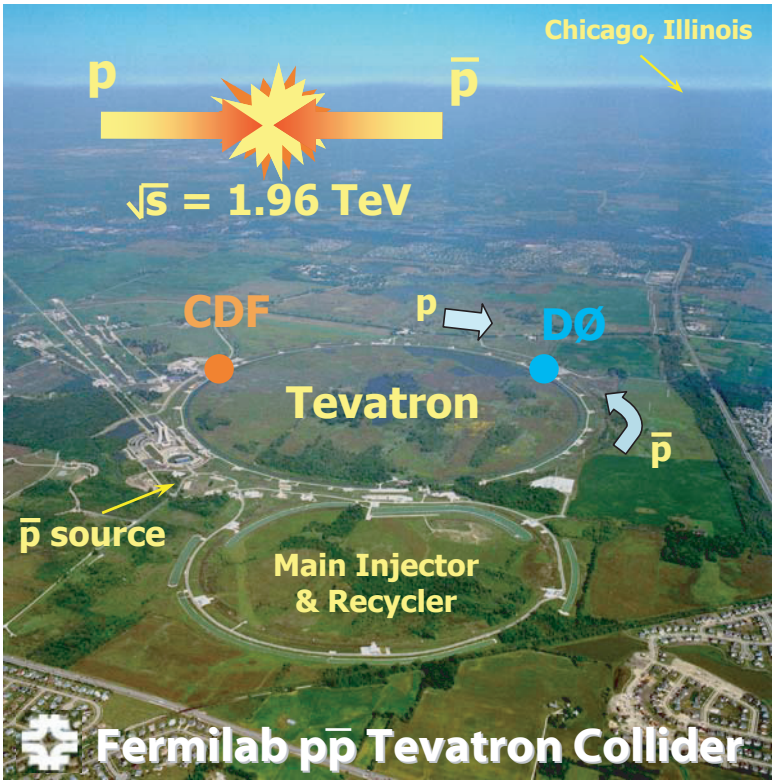

Figure 2.1. Fermi National Accelerator Laboratory is located about 40 miles outside of Chicago, IL, in the United States. This aerial view of the Laboratory shows some of the major structures, which are described in the following sections.

2.1 The Accelerator Complex

Scientists working on experiments at particle colliders depend a great deal on accelerator physicists, who create and control the beams of interacting particles. At Fermilab, a beam of protons and a beam of antiprotons collide at the center of the CDF and DØ experiments.

Once protons and antiprotons have both been injected into the Tevatron, this is the beginning of a "store." A store lasts as long as the beams are colliding. When everything is functioning well, the average duration is more than 24 hours of continuous data taking. The store ends when the number of particles in the beams is low enough and there are available antiprotons to begin a new store.[1]

[1]A store can also end due to a malfunction where the beams are disrupted and lost. If the machines lose control of the protons and antiprotons, the beams are directed to absorbers where they lose their energy without damaging the accelerator or detectors.

To create these collisions, electric and magnetic fields are used by the accelerator physicists. Two important facts of nature are used: charged particles are accelerated by an electric field, and their path is curved by a magnetic field (Equations 2.1 and 2.2) [22].

$$\vec{F} = m\vec{a} = q\vec{E} \tag{2.1}$$

$$\vec{F} = m\vec{a} = q(\vec{v} \times \vec{B}) \tag{2.2}$$

One of Newton's three laws describes the force ($\vec{F}$) on a particle as equal to its mass (m) times acceleration ($\vec{a}$). The acceleration due to an electric force depends only on the mass, charge (q) and the electric field ($\vec{E}$). The magnetic force is proportional to $\vec{v} \times \vec{B}$. The cross product of the velocity $\vec{v}$ and the magnetic field $\vec{B}$ is always perpendicular to the two arguments, so the magnetic force is always perpendicular to the motion of the particle. This causes the curvature in the magnetic field.

$$F = qvb = \frac{vp}{\rho} \tag{2.3}$$

$$p = \rho q B \tag{2.4}$$

This curvature keeps the beam traveling in a circle in the underground ring of the accelerators. Track curvature will also be useful later for measuring the momentum of a particle (p) using a known magnetic field strength, the charge of the particle, and the radius of curvature (ρ), shown in Equation 2.4.

The protons (with charge +1) and antiprotons (with charge -1) are accelerated and curved in opposite directions by the fields; this allows the protons and antiprotons to travel inside the same structure, in opposite directions.[2]

[2]To allow the beams the freedom to travel, the beam pipe must be evacuated and kept at a typical operating pressure of 10^{-7} torr, which is similar to the vacuum of space near earth.

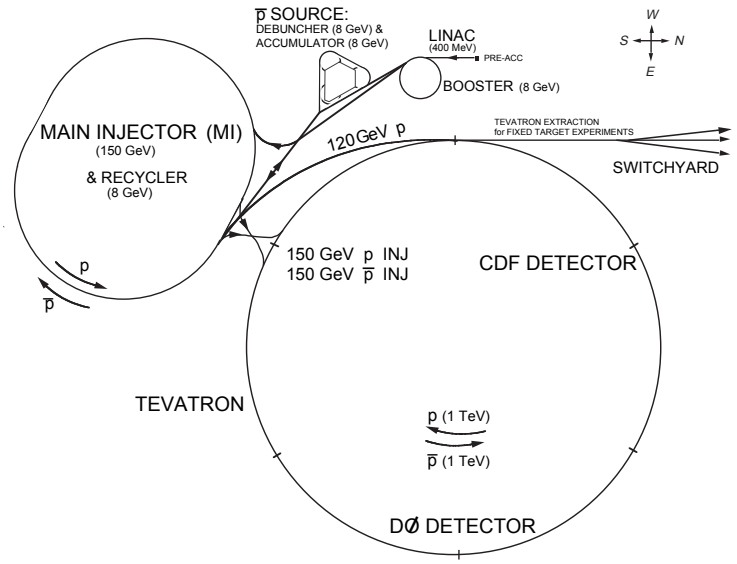

Figure 2.2. The Tevatron accelerator chain creates a beam of 1 TeV protons and 1 TeV antiprotons which collide about 2 million times per second at the CDF and DØ experiments. The protons begin at the Cockcroft-Walton preaccelerator ("Pre-Acc") while the antiprotons ("$\overline{p}$'s") are created at the "$\overline{p}$-source". Experiments other than CDF and DØ are serviced by protons from the switchyard.

To accelerate the protons and antiprotons, different types of machines are used; all of them rely on the simple rules above.

2.1.1 The Protons

Protons begin their time at Fermilab in a small bottle of hydrogen gas inside the Cockcroft-Walton Preaccelerator (Figure 2.3). Hydrogen atoms have one proton and one electron, so removing the electrons could yield the protons that are needed to form the beam. Instead, H^- ions are formed: the electron is stripped away with an electric field, then the protons interact with cesium where they pick up two electrons. These H^- ions are useful in a later transition between accelerator systems.

The electric field that accelerates the ions is caused by the Cockcroft-Walton, a device that generates a high voltage with a low current using capacitors and diodes. The H^- ions travel through a high voltage gap of 750,000 V created in this Preaccelerator, giving them an initial energy of 750 keV.

Each one of the systems following the Preaccelerator is designed to take an in-

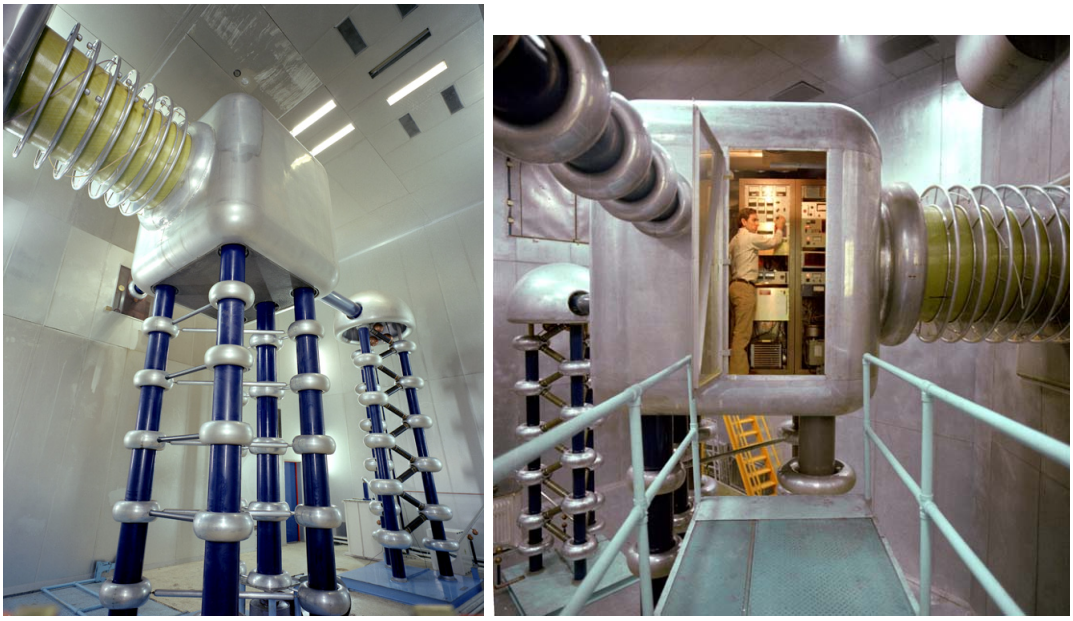

Figure 2.3. The Cockcroft-Walton Preaccelerator's curvy shapes are useful as well as stylish. The curvature helps prevent charge from collecting on the surfaces, which could lead to a lightning-like arc. On the right, the interior is shown. The small bottle of hydrogen gas is located inside the box where the man is standing. The H^- ions leave through the tube on the right-hand side, to the Linac, passing through a potential difference of 750,000 V on the way.

coming beam of particles with a specific energy and increase it. The next step is the Linear Accelerator (Linac) which increases the ions' energy from 750 keV to 400 MeV. The Linac is 150 m long, and it accelerates charged particles using Radio-Frequency (RF) cavities (Figure 2.4). RF cavities create an oscillating electromagnetic field that is varied as ions pass through to create acceleration.

Because of the oscillating nature of the Linac, the stream of particles is grouped into bunches of ions, separated by gaps. The Linac creates a pulse of particles with a length of 20 ms, but the next accelerator is a circle with a circumference that only holds 2.2 ms of beam, so the beam overlaps itself several times in the transition. To aid in the transition, the H^- beam goes though a thin carbon foil to remove the electrons from the ions, leaving a beam of protons. Stripping off the electrons is an irreversible process, which allows the spatial distribution to be changed without

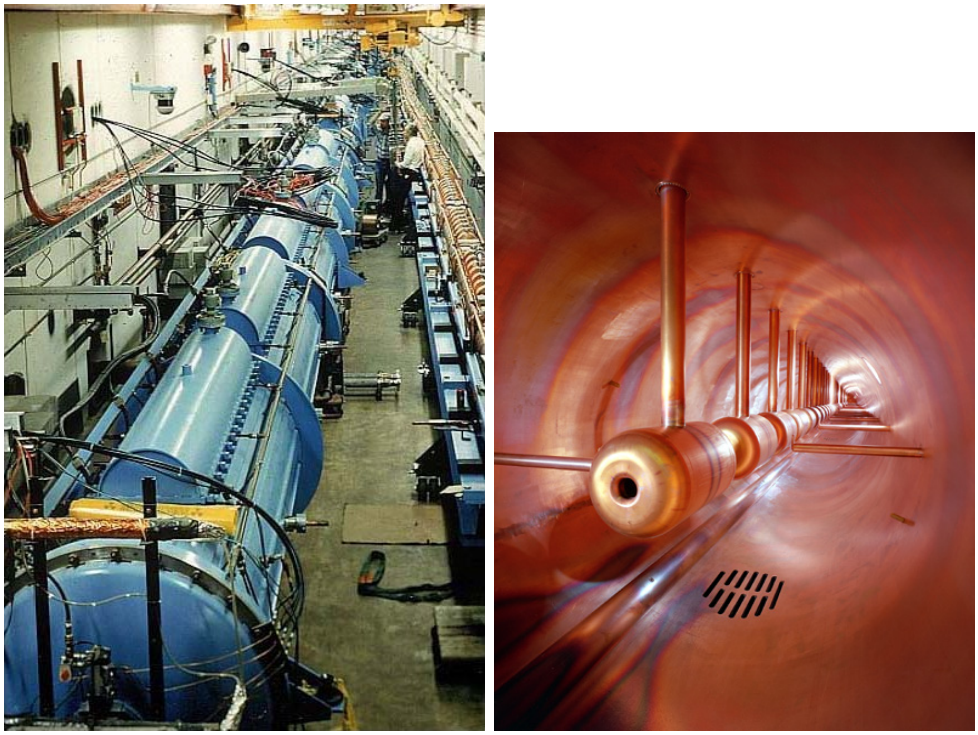

Figure 2.4. The H^- ions are accelerated in Linear Accelerator, made up of the light blue tanks (left). The acceleration happens inside, in the spaces between the cavities (right).

changing the momentum distribution.[3] Stripping off the electrons helps create a tightly-packed, low-dispersion beam of protons.

After the Linac, the beam of particles enters the Booster ring, which is a synchrotron, 75 m in diameter. In a synchrotron, the particles travel around, getting a boost of energy every time they complete a revolution. The magnetic field changes in careful synchrony with the traveling beam, since the particles curve along the same path but with increasing energy. The protons travel around the Booster approximately 20,000 times. When they leave the Booster, their energy has increased from 400 MeV to 8 GeV.

The Main Injector is the next accelerator to increase the energy of the protons. This 3 km circumference synchrotron is the newest of the accelerators, beginning operation in 1998. The Main Injector accelerates protons for two purposes at Fermilab.

[3] If it were a reversible process, the change would not be allowed according to Liouville's Theorem.

The protons are used in collisions in the Tevatron and also for producing antiprotons. For the first set, the protons reach an energy of 150 GeV before being transferred to the Tevatron. For antiproton production (discussed in the next section) they only reach 120 GeV.

Figure 2.5. The Tevatron was built in a tunnel that used to hold another accelerator above it. As the Tevatron began operation, the Main Ring accelerator was removed. The Tevatron magnet in the photo above is painted red.

The Tevatron is a tunnel with a 1 km radius, located 10 m underground (Figure 2.5). It is instrumented with superconducting magnets which bend the particles and antiparticles in opposite directions, so protons travel clockwise and antiprotons, counterclockwise. The beams of protons and antiprotons are accelerated in the Tevatron to their peak energy, 980 GeV in each beam. They travel in a helical orbit in the same beam pipe, intersecting only in the centers of the two experiments on the Tevatron ring: CDF and DØ.

2.1.2 The Anti-Protons

While the protons used in the collisions are readily available from hydrogen atoms, the antiprotons must be created. At Fermilab, the machinery for creating antiprotons and forming them into a controlled beam is called the antiproton source (Figure 2.6).

Successfully manufacturing this beam of antiprotons is one of the most difficult parts of running the Fermilab accelerator complex.

Figure 2.6. The Fermilab Antiproton Source (1986-present): The three buildings in the center of the photograph are above the Accumulator ring. In the top of the photograph, the Main Injector can be seen. Below, the circular Booster ring is visible, and to the left is the Tevatron.

Protons from the Main Injector are used to create the antiprotons. When they are guided into a target, the result is a shower of many secondary particles and antiparticles. The outgoing particles are focused through a collection lens made of lithium (Figure 2.7). Lithium is used because it is the least dense solid conductor, minimizing scattering and absorption of particles traversing it. Current in the cylindrical lens creates a magnetic field which increases with the radius to focus the beam, as shown below.

$$\oint B \cdot d\ell = \mu_0 I_{\text{encl}} \tag{2.5}$$

$$2\pi r B = \mu_0 I_{\text{encl}} \tag{2.6}$$

$$B = \frac{\mu_0 I_{\text{encl}}}{2\pi R^2} \cdot r \tag{2.7}$$

The first line shows the relationship between the path integral of the the magnetic field (B) and the current enclosed (I_{encl}), with the usual constant (μ_0). Integrating and isolating B reveals the increasing field with increasing radius (r) where R is the radius of the cylinder.

After the lens, a magnetic field bends negative particles (including the antiprotons) into a beam pipe which goes to the Debuncher ring. For every one or two antiprotons that are captured and stored, it takes 100,000 protons striking the target.

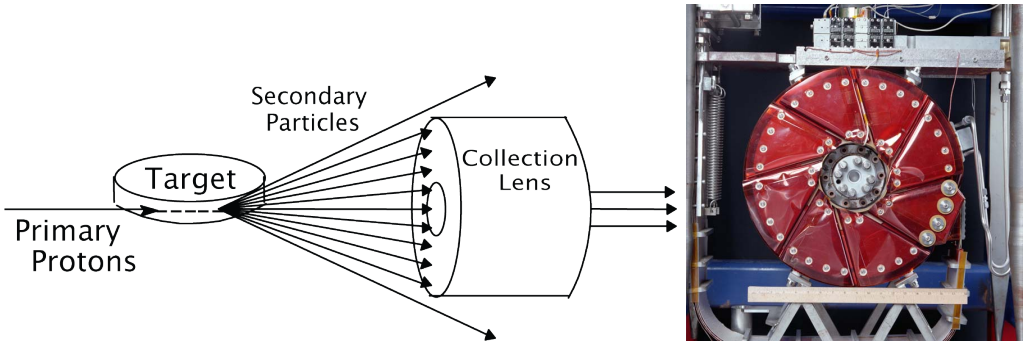

Figure 2.7. The target that the protons hit is a nickel disc, about 2 cm thick and 10 cm in diameter. It is slowly rotated so that the entire disc is bombarded evenly with protons. The collection lens is the solid circle in the center of the red material on the right.

The next goal for the antiprotons is to create a beam in which the momenta are uniform and near 8 GeV. If the particles have very different momenta, their transfer from system to system will be less efficient, and the subsequent systems will move the beam less efficiently. The Debuncher is a triangular underground ring which does some shaping of the antiprotons in momentum space, creating a beam with a wide position distribution but a tight momentum distribution. The protons come from the Main Injector in 82 bunches, 1.5 seconds apart. The secondary particles coming from

the target retain the same bunch structure as the original protons. Antiprotons only remain in the Debuncher for the time between proton pulses.

Next, the antiprotons are transferred to the Accumulator, where more are added each time the proton beam strikes the target. When there are a sufficient number to be transferred, they go into the Main Injector and Tevatron. The Accumulator is in the same triangular tunnel as the Debuncher. Antiprotons are "momentum stacked" here until the beginning of a new store.

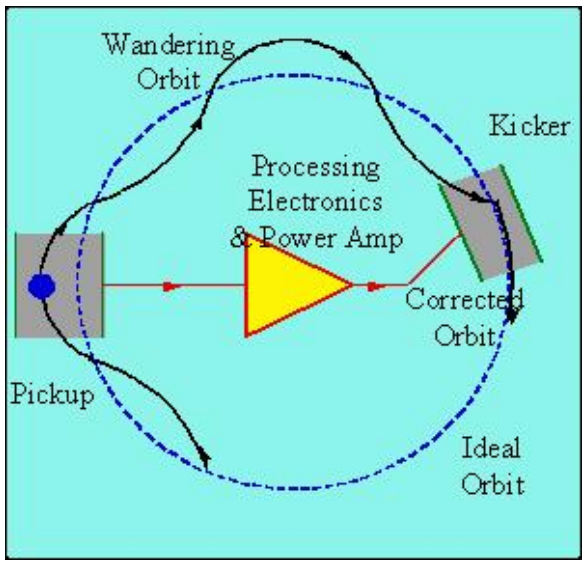

Figure 2.8. As the antiprotons travel in their triangular path, they undergo stochastic cooling, in which the average transverse momentum is reduced. The properties of the beam are measured on one side of the ring and corrected on the other.

Since 2004, another ring called the "Recycler" has also been used to hold antiprotons until they are used in collisions. It is 3 km in circumference, in the same tunnel as the Main Injector. The Recycler was originally designed to reclaim antiprotons that remained at the end of a store, to be reused in the next store. Implementing the recycling proved too difficult, but the machinery is still put to use. Antiprotons are transferred from the Accumulator to the Recycler, where they are stored at 8 GeV using permanent magnets.

In the Recycler, the beam is cooled using electron cooling. A very controlled beam

of electrons is circulated alongside the less-controlled antiprotons, and the two beams interact. The electrons start out cooler, and the antiprotons scatter the electrons until the two bunches are in thermal equilibrium. This is the first successful implementation of this technique for such high-energy beams. The cooling produces a more compact antiproton beam, which increases the number of interactions when the proton and antiproton beams collide.

After enough antiprotons are accumulated, they are injected into the Tevatron. The antiprotons are separated into four bunches with 396 ns spacing, accelerated up to 150 GeV, and sent off for collisions. This takes place nine times, yielding 36 bunches of antiprotons.

2.1.3 Defining Luminosity

Luminosity is used in particle physics to describe the density of collisions, and the number of collisions over time.[4] Increasing the number of collisions helps increase the odds of observing rare new phenomena.

The instantaneous luminosity is a measure of the density of the beams. Important parameters are the number of particles in the proton and antiproton beams (n_p and $n_{\overline{p}}$), and the frequency with which the beams cross (f). The luminosity is inversely proportional to the cross-sectional areas of the beams (σ_p and $\sigma_{\overline{p}}$): if the beams have a smaller cross section, they are more densely packed, and more collisions occur (Equation 2.8). Instantaneous luminosity has units of $\mathrm{cm}^{-2}\ \mathrm{s}^{-1}$, or $\mathrm{b}^{-1}\ \mathrm{s}^{-1}$. [5]

$$\mathcal{L} = f\frac{n_p n_{\overline{p}}}{4\pi\sigma_p\sigma_{\overline{p}}} \tag{2.8}$$

[4]Both instantaneous and integrated luminosities are often called simply "luminosity." The type of luminosity in question is determined from the context.

[5]The unit of area "b" for "barn" has been used in particle and nuclear physics since the 1940's when it was a classified term, used for obfuscation. It was declassified in 1948 and its usage persists in the field, though it is not an SI unit [31]. One b^{-1} is equal to $10^{-24}\mathrm{cm}^{-2}$, approximately the size of a uranium nucleus.

Though the beam parameters vary with each store, the number of protons can reach 1×10^{13}, while the number of antiprotons is usually about a factor of ten lower, near 2×10^{12}. The frequency is 1.7 MHz. The beam cross sections are approximately 100 μm each. At Fermilab, the instantaneous luminosity has been increasing as the accelerator runs (Figure 2.9) with new world records set in the last year. The highest luminosity reached was $2.85 \times 10^{32} \text{cm}^{-2}\text{s}^{-1}$, on February 18, 2007.

Integrated luminosity is a measure of interactions over a period of runs, given by the integral of the instantaneous luminosity with respect to time. It is measured in "inverse barns" to allow easy comparison to cross sections, which are usually stated in barns. See Section 3.2.1 for more discussion of luminosity in calculations for physical processes. The integrated luminosity for the current running period of the Tevatron is shown in Figure 2.10.

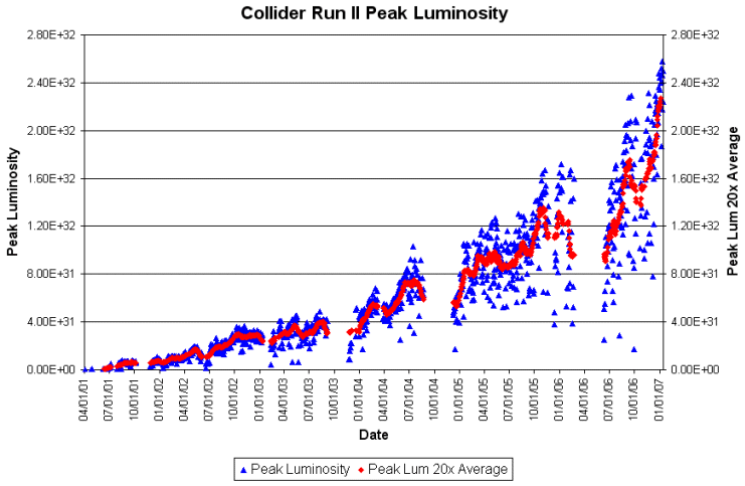

Figure 2.9. The instantaneous luminosity at the Tevatron collider is increasing with time. Gaps indicate time periods when no data was being taken. Each blue triangle corresponds to one store, while the red triangles are each the average of 20 stores. The axes are given in units of $1/(\text{cm}^2\ \text{s})$.

2.2 The CDF Apparatus

The goal of the CDF experiment is to record the results of the collisions of protons and antiprotons by measuring the properties of the outgoing particles. The scientists

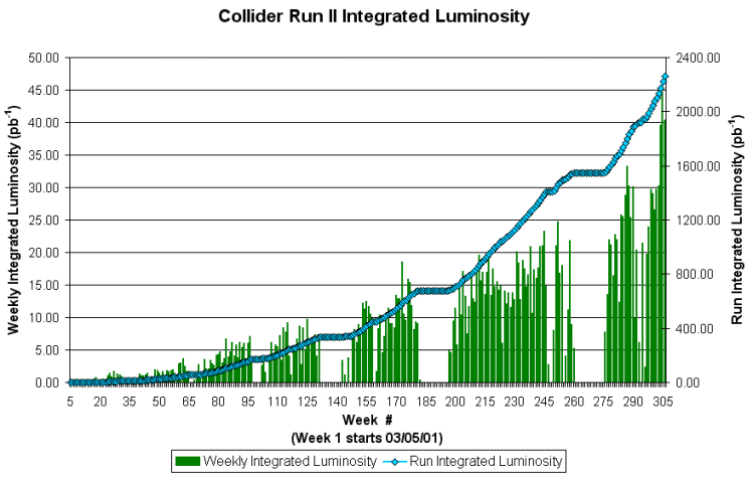

Figure 2.10. The integrated luminosity increases with each store. The green bars show the total data taken for each week. The blue diamonds show the total integrated luminosity since 2001. The axes are in units of inverse picobarns, or $1/(10^{-40}\mathrm{m}^2)$.

who work on this experiment designed, built, and maintain the apparatus as it collects data up to 24 hours each day for most of the year.

The CDF experiment has been operating at Fermilab since the late 1980's. It was designed with discovery in mind: evidence of the top quark had not yet been observed, and the W and Z particles had just been discovered at CERN. With the dataset gathered at CDF, it is possible to test many different kinds of theories at once. This is done by looking for new types of matter and by making precise measurements of the properties and interactions of the known particles.

In particle physics research, the basic unit of analysis is a record of an "event." Each time the proton and antiproton beams collide in the center of the detector, the experiment records data about the collision. Each event is completely independent of the ones previous to it and following it.

When the beams cross, many outcomes are possible. It is possible that there is very little interaction, that the protons and antiprotons pass each other by. In this case, the event that is recorded has very few particles observed. A more interesting outcome occurs when one or more protons hits one or more antiprotons, and they

produce a number of secondary particles. This process is complicated by the fact that protons and antiprotons are each made of three quarks, so any number of the quarks may be interacting. Both particles also contain gluons, and these may participate as well. To complicate things even further, the three main quarks (known as the valence quarks) are accompanied by a sea of other pairs of quarks and antiquarks constantly popping in and out of existence. Since a proton contains up, up and down quarks and and antiproton contains antiup, antiup, and antidown, one expects many up-antiup reactions, for example. But sometimes up-anticharm processes are observed. This can occur when the anticharm quark is one of these sea quarks.

The outcomes of the collisions occur in a statistical distribution that should be predicted by the Standard Model. The detector is constructed to obtain as much information about the particles involved in the interaction, such as the spatial point where the interaction took place, and the number of outgoing particles, their charges, momenta, and energies. The concentric systems that make up the CDF apparatus (Figures 2.11 and 2.12) each have a role to play in providing this information.

2.2.1 Tracking Systems

Tracking systems provide information about charged particles. As they interact with the material in the tracking system, a series of positions and times are accumulated. These time-space points are reconstructed into a track. The number of tracks indicates the number of charged particles that entered the detector in the final state. Some final state particles can travel away along the beam without being detected. The tracking system is placed inside a magnetic field to curve the particles' tracks, revealing more about them. Their velocities remain constant in z after the collision, so they travel helical paths. The direction of the curvature is related to the charge of the particle according to Equation 2.4. From the curvature, the momentum can also be determined. As the momentum increases, there is less and less curvature, so the

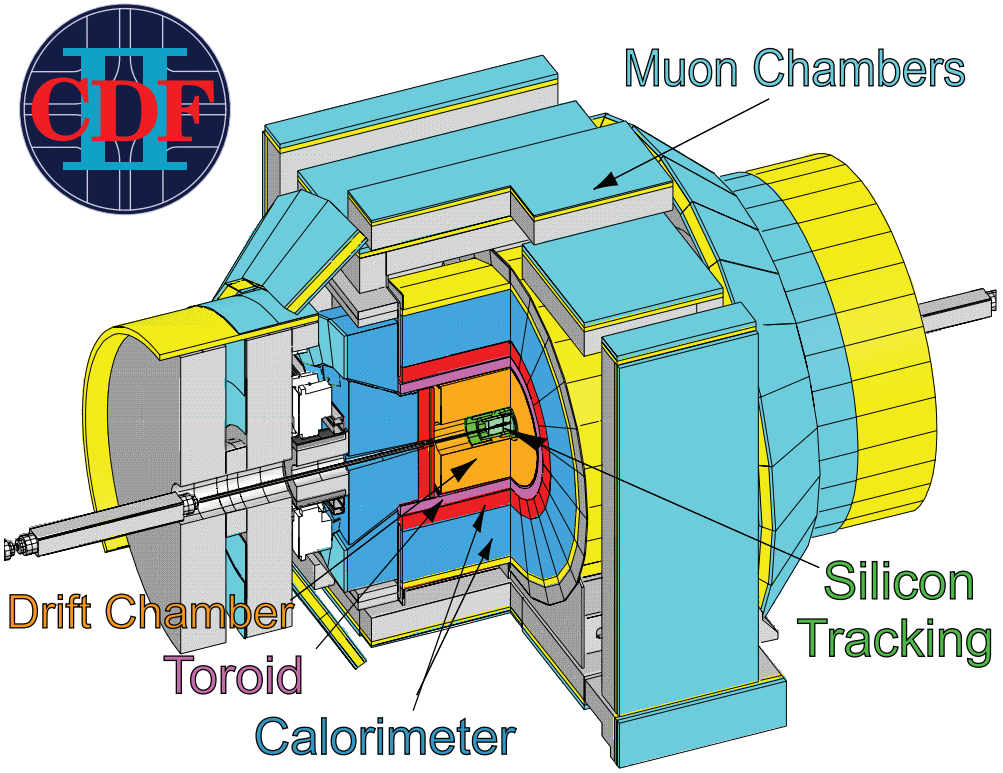

Figure 2.11. The CDF Experiment (with one quarter missing) and its major subsystems. The coordinate system of CDF is shown in Figure 2.13. The detector is described in detail in the Technical Design Report [13].

uncertainty on the momentum and the charge increases.

At CDF, the tracking system is surrounded by a superconducting solenoid magnet, 5 m long, with a radius of 1.5 m. The magnetic field is 1.4 Tesla, uniformly, along the beam axis. The position of the solenoid can been seen in Figure 2.12.

In addition to determining the charge and momenta of particles, tracking is also important for separating particles that came from different interaction points. Since more than one proton and antiproton can collide in any given beam crossing, all the particles in the final state may not have come from one interaction. Precise tracking information can reveal the locations of the interaction point(s), called the primary vertex or vertices.

There may also be secondary vertices in the events: these are vertices displaced from the primary one. They occur when a particle has traveled some distance away

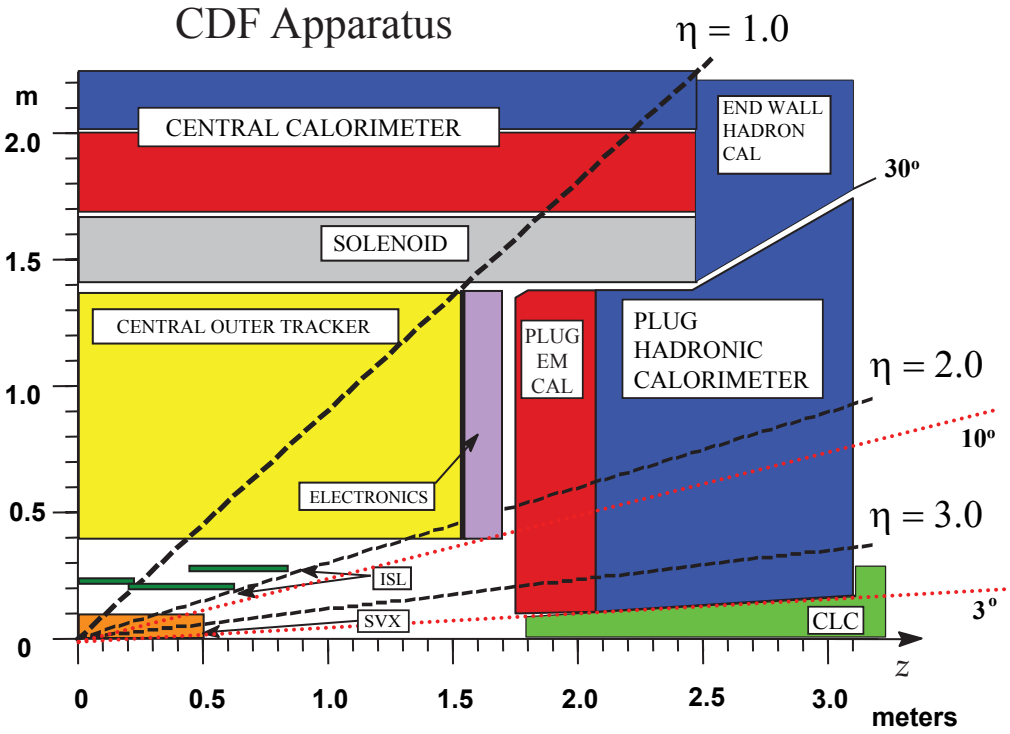

Figure 2.12. One quarter of the CDF Experiment and its major subsystems. η is defined in Figure 2.13.

from the initial collision and then it decays. Secondary vertices are most useful for studying long-lived particles, like the b quark.[6]

The Silicon Vertex Detectors

The most precise tracking system is found in the center of the detector, closest to the interaction point. Several layers of silicon wafers record the locations of particles with very high precision.

When charged particles travel through the detectors, the energy that they deposit creates pairs of electrons and positive holes (Figure 2.15). These charges drift in an electric field to the surfaces of the silicon where they are integrated, digitized, and

[6] "Long-lived" particles like b quarks have average lifetimes of over 1 ps and often travel a few millimeters before they decay, compared to shorter-lived particles like the W and Z which have lifetimes near 10^{-25} s. Short-lived particles decay too quickly to be able to distinguish their decay vertices from the primary vertex.

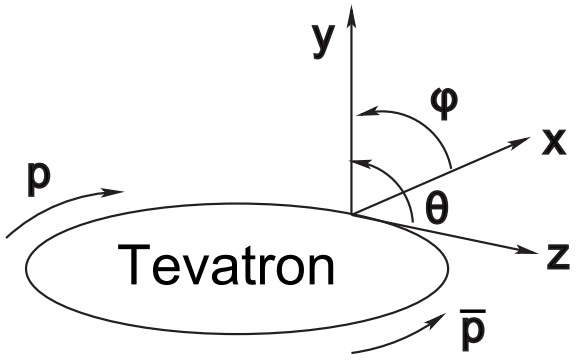

Figure 2.13. The CDF coordinate system is defined with z along the proton beam axis. The rectangular coordinates x (radially outward from the center of the Tevatron) and y (upward), and the angle θ (the polar angle) are rarely used in physics analysis. The coordinates z, ϕ (the azimuthal angle in the $x-y$ plane) and $\eta = -\ln[\tan(\theta/2)]$ (the pseudorapidity) are the most commonly used.

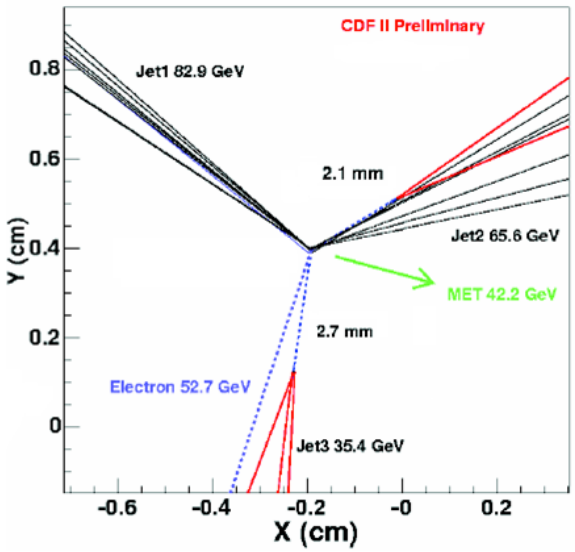

Figure 2.14. In this close-up view of one CDF event, the lines in the diagram represent particle tracks coming from the interaction point in the center. Red tracks are presumed to come from secondary vertices which are 2.1 and 2.7 mm away from the primary vertex. The innermost detector is located at a radius of 1.1 cm, outside of this diagram. The missing transverse energy (MET) corresponds to unobserved particles like neutrinos. It is calculated using conservation of energy and all the observed particles, as described in Section 5.1.1.

read out using custom electronics. Silicon, a solid semiconductor, is used because of its fast response and low ionization energy.

The silicon system at CDF is made up of three parts, built in layers as shown in Figure 2.16. There are six concentric barrels, each with twelve wedges in ϕ, followed by one or two more layers of the intermediate silicon system. Each of the three

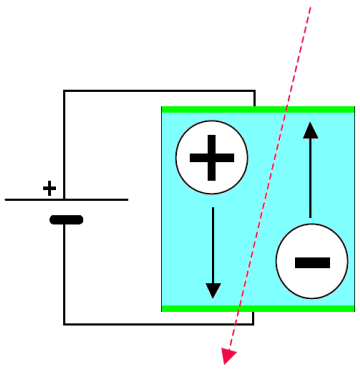

Figure 2.15. When a charged particle passes through a solid silicon detector, the charges it creates drift to the surfaces to be measured.

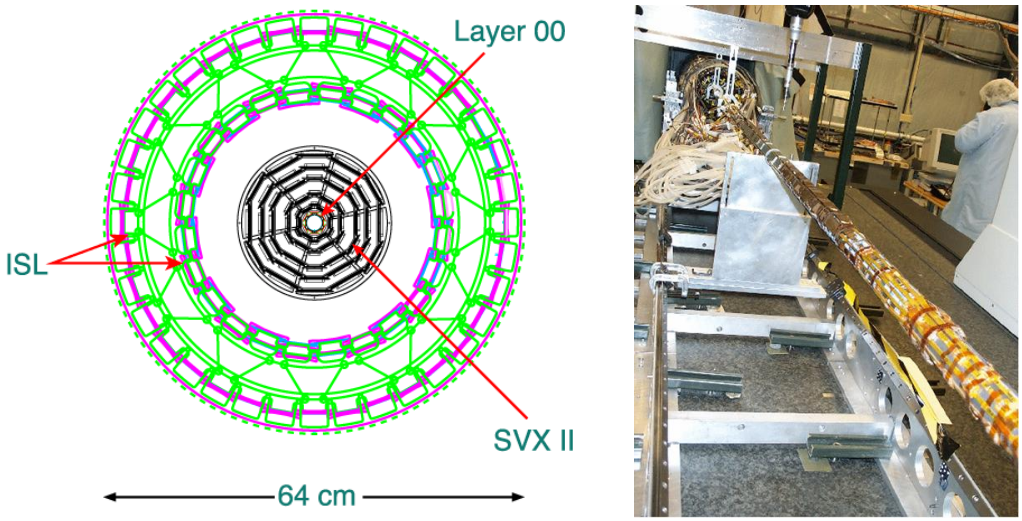

Figure 2.16. This schematic of the silicon detectors shows the cross section of all the detectors. Layer 00 is the innermost set of modules, surrounded by five layers of the Silicon Vertex detector (SVXII) and the Intermediate Silicon Layers (ISL) On the right, Layer 00 is inserted into the rest of the SVXII barrels.

subdetectors has slightly different parameters, but all operate on the same principle. Charge deposited in the silicon is recorded to provide a set of points for the construction of tracks.

The first layer, Layer 00, is closest to the beam at $r = 1.1$ cm. The width of the silicon strips in this innermost layer is 25 μm, but only every other strip is read out. This improves the resolution of the silicon tracking without compromising efficiency. The modules in this subsystem are instrumented on one side only. Each 256-strip piece of silicon is 15 mm by 78 mm. The resolution of Layer 00 is 15 μm.

The next subsystem (SVXII) has five more layers in the center of the detector, covering 48 cm to either side of $z = 0$. The radius of this part of the silicon covers $r = 2.5$ cm to 10.6 cm. Each of these five layers is instrumented on both sides, with some angle between the strips on the two surfaces. Its innermost layers, Layers 0 and 1, and Layer 3 are created with the strips at 90 degree angles, while the other two layers (2 and 4) have a small angle of 1.2 degrees between the strips. The width of the strips in these layers is 60-65 μm for the $r - \phi$ layers and 140 μm for $r - z$. The angles between the strips yield better three-dimensional tracks, at a resolution of about 20 μm.

Outside of the barrels, three additional layers of silicon (the ISL) extend the silicon tracking coverage to $|\eta| < 2$ (Figure 2.17). There is one more central layer and two layers farther out. The strips have a 112 μm pitch, and 1.2 degrees of stereo angle between the strips on either side.

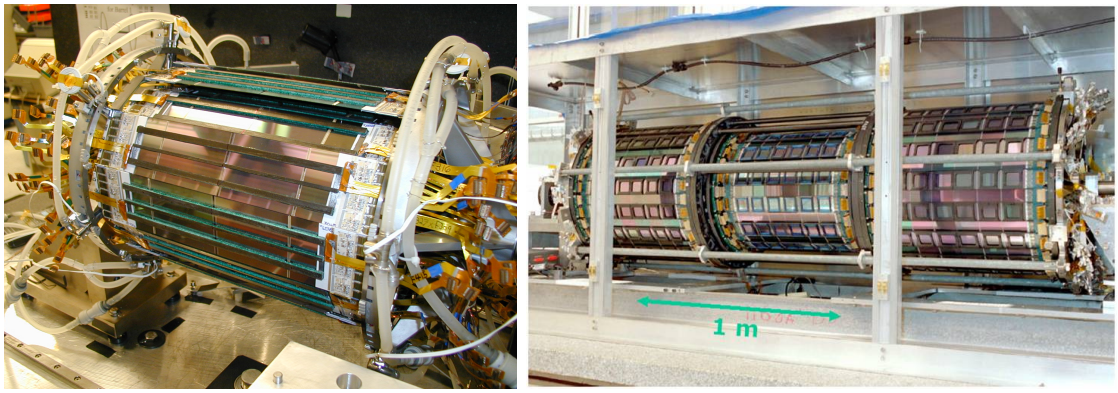

Figure 2.17. The SVXII (one part in construction, left) and ISL (finished, right) silicon detectors, combined, have over 700,000 channels. Connecting the cables for these instruments took four people on three eight-hour shifts a day seven weeks to complete! [40]

The Central Tracker

The Central Outer Tracker (COT) is located just outside of the silicon system. It is a drift chamber, in which gas is ionized by charged particles. The resulting electrons and ions drift to nearby anodes and cathodes, where they are recorded (Figure 2.18). As they near the place where they are collected, there is a strong electric field which

creates an avalanche of ions. The avalanche helps generate enough signal to be measured.

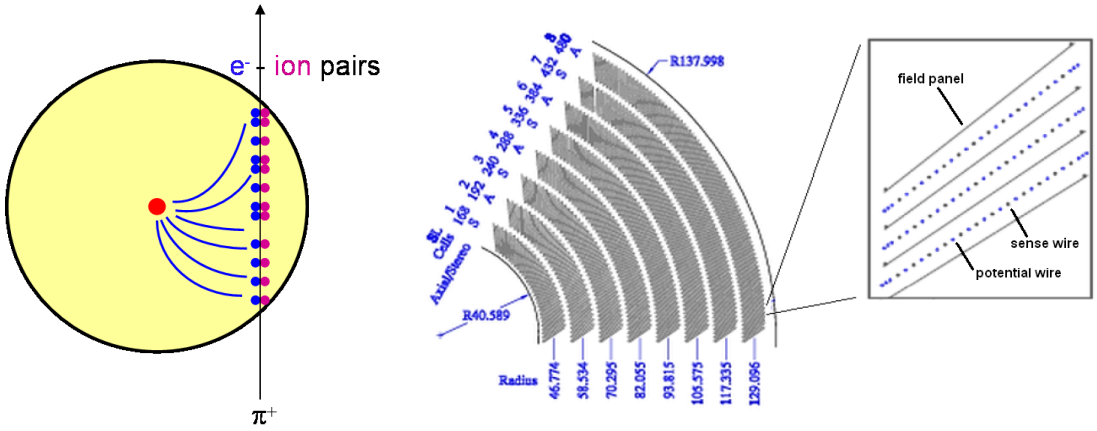

Figure 2.18. Electrons drifting to a wire supply a signal from a charged particle at left. The schematic on the right shows the number of cells in each superlayer (SL), and the radius in cm. Zooming in, the individual sense and potential wires can be seen.

At CDF, the drift chamber is a cylinder 3.1 m in length, with a 1.4 m radius [9]. This provides tracking coverage out to $|\eta| < 1.1$. A mixture of gases fills the chamber (60% Argon, 40% Ethane). The apparatus is divided into subsections: eight concentric superlayers, each with many cells of wires (Figure 2.18). Four of the superlayers have wires along the beam in the z direction, while the other four have wires strung at 2 degrees from z to provide axial (r-ϕ) measurements. The axial layers help determine the z position of the tracks with a resolution of 5 mm.

Each superlayer has a different number of cells, from 168 in the smallest layer to 480 in the largest. The cells each contain 25 gold-plated tungsten wires, 40 μm in diameter. Twelve of those wires are sense wires, while the remaining ones shape the fields. The total number of wires is 73,080 wires, 30,240 of which are sense wires, for a total load on the end plates of 36,132 kg. The cells are angled at 35 degrees to compensate for the force from the magnetic field, so that it is completely canceled by the radial component of the electric field. With these specifications, the single hit resolution of the chamber is 140 μm. The momentum resolution using only the COT

is $\sigma p_T/p_T^2 = 0.15\%$. Better resolution is obtained by adding hits from the silicon and constraining track to the position of the beam.

One important design consideration for a drift chamber is the time difference between a charged particle's passage near a wire and the detection of the electrons on the wire. This time delay is called the drift time. If the drift time is too close to the beam crossing interval, signals from two subsequent events could overlap. In the CDF COT, the maximum drift time is 177 ns. This ensures plenty of time between the 396 ns beam crossings.[7]

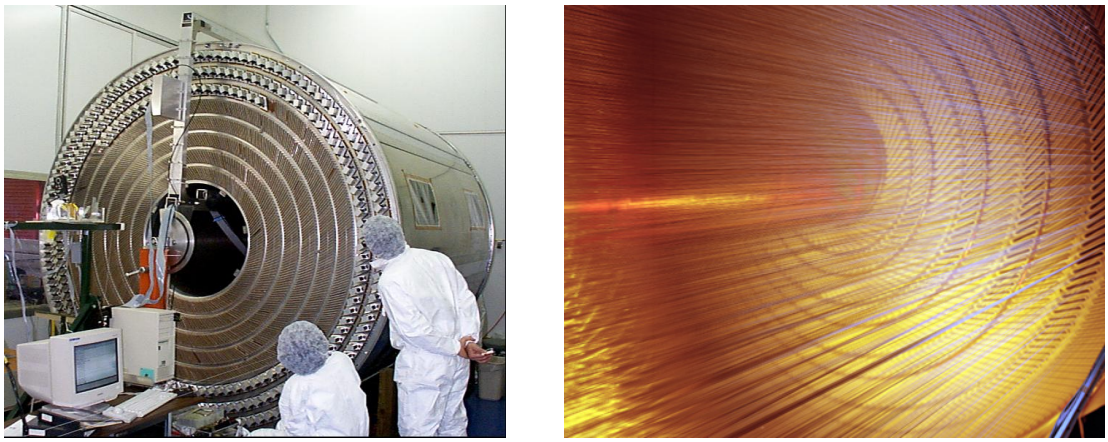

Figure 2.19. The eight superlayers in the COT can be seen in these photographs, as well as the angled cells which make up each layer. On the left, outer layers have electronics attached to groups of cells, while inner layers have not yet been instrumented. On the right, the wires inside the COT are visible.

2.2.2 Calorimetry

The calorimeter measures the energy of all particles: both charged and neutral. The calorimeter also yields position information, but with a much lower resolution than the trackers. The tracking system can measure momentum, charge, and position for charged particles, but neutral particles usually escape the tracking volume undetected.

[7]The original plan for the Tevatron Run II was to begin with 396 ns beam crossings and then switch to 132 ns. If this had happened, the gas mixture was to be changed to Argon/Ethane/CF_4, and the maximum drift time would have been 100 ns.

Physics of Calorimeters

The two forces that are most important in interactions in calorimeters are the electromagnetic force and the strong force. Most particles interact electromagnetically, and photons, electrons, muons, and taus primarily interact this way. Charged particles made up of quarks (mesons and hadrons) react electromagnetically, too, but their main interactions in material are in response to the strong force. Taking these differences in account, the CDF calorimeter has two concentric sections. The electromagnetic (EM) calorimeter records almost all of the energy from photons and electrons. The hadronic calorimeter takes care of the rest.

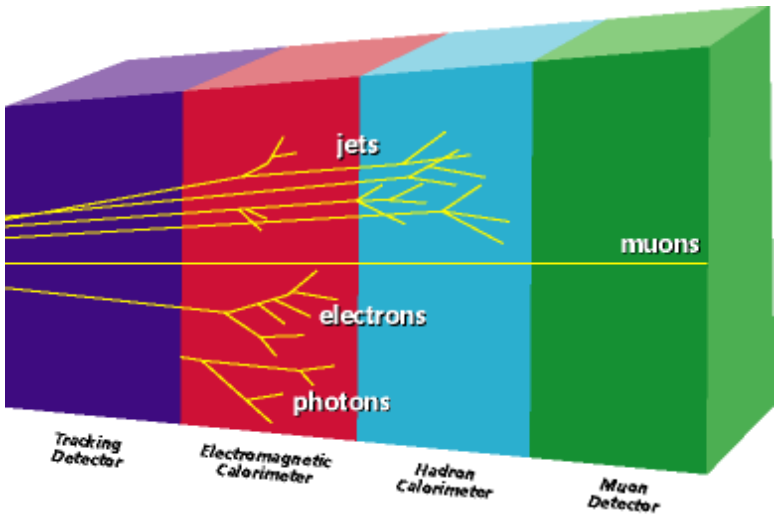

Figure 2.20. The reactions of different types of particles identify them as they pass through the detectors. All charged particles leave tracks in the tracking detector. Photons, electrons and jets of hadronic particles produce showers in the electromagnetic and hadronic calorimeters, as described in this section. Muons leave very little energy in the calorimeters, so they are detected in the muon systems, described in more depth in Section 2.2.3.

The interaction processes of the different particles dictate the types of materials used for calorimetry and the size of the calorimeters. These interactions (shown in Figure 2.20) allow particles to be identified by their traces in the various subsystems.

Photons in the EM calorimeter can have several kinds of interactions. In general, photons can be absorbed by atoms by ejecting electrons from them (the photoelectric effect), or they can lose some of their energy by interacting with electrons and

continuing along (Compton scattering). Photons can also interact with a nucleus of an atom and convert into an electron and positron pair, while conserving energy and momentum. Only 1.022 MeV of energy is needed to pair-produce the electron and positron. Photons at CDF often have energies of many GeV, and at that energy, most of their interactions are through pair production. After one pair production, there are three particles carrying the energy of the initial one: an electron, positron, and photon. These continue to interact and to produce a further shower of particles.

Electromagnetic cascades for electrons proceed through collisions with atoms (where they excite or ionize the atom) and through bremsstrahlung. Bremsstrahlung (or breaking radiation) is produced when an electron is deflected by an atomic nucleus or another charged particle. As the electron accelerates it emits a photon, which can produce another shower, as described above. An electron is particularly sensitive to bremsstrahlung because its mass is small compared to the nuclei of atoms it passes, so the electric field from the protons, concentrated in the nuclei, exerts a great pull. Conventionally and in the discussion below, the depth of the electromagnetic calorimeter is given in radiation lengths (X_0). One radiation length is the distance over which a high-energy electron loses all but $1/e$ of its energy by bremsstrahlung.

Muons are much heavier than electrons, so they travel without much bremsstrahlung at Tevatron energies. The lack of interaction through bremsstrahlung allows them to penetrate the detector much more easily. They have no strong charge, so they do not interact in that way, either. They deposit only small amounts of energy when they excite or ionize atoms as they pass through.

Hadrons are also much heavier than electrons, so they are not as affected by bremsstrahlung from the electric fields of the nuclei. They do leave some energy in the EM calorimeter when they decay into other particles. For example, a neutral pion is one frequently produced particle that decays to two photons. The photons will shower electromagnetically, as described.

Unless they decay, particles made of quarks must pass close enough to the nucleus of an atom in the material to be affected by the calorimeter. When they collide with nuclei and excite them or break them apart, additional particles are be produced. The original particle also slows down. This continues until all the particles produced in the shower are slowed and stopped in the material. The depth of material in a hadronic calorimeter is given in interaction lengths. One interaction length (λ_0) is the mean free path through which a particle travels without undergoing an inelastic nuclear interaction.

Sampling Calorimeters

The calorimeters at CDF are sampling calorimeters. They are made of alternating layers of an absorber material, like lead or steel, and layers of a scintillating material. When particles encounter the absorber, they interact with the dense material and a shower of secondary particles is created. The secondary particles enter the next layer of the detector, which is a scintillator. The total energy of the initial particle can not be measured, but it can be inferred by measuring the energy in the samples of each scintillator tile.

Scintillators are compounds which release light when energetic particles travel through them. In the calorimeter, the light that is created travels through a guide to a photomultiplier tube (PMT). The PMT converts the light into an electrical pulse that can be measured. The pulse yields the amount of light, which correlates with the amount of energy that the particles had when they went through the scintillator. Any particles that continue on through the layer of scintillator hit another absorber, starting the showering process again (Figure 2.21). A well-designed calorimeter should contain enough layers of material to completely capture the showers of incident particles, in order to accurately measure their energies.

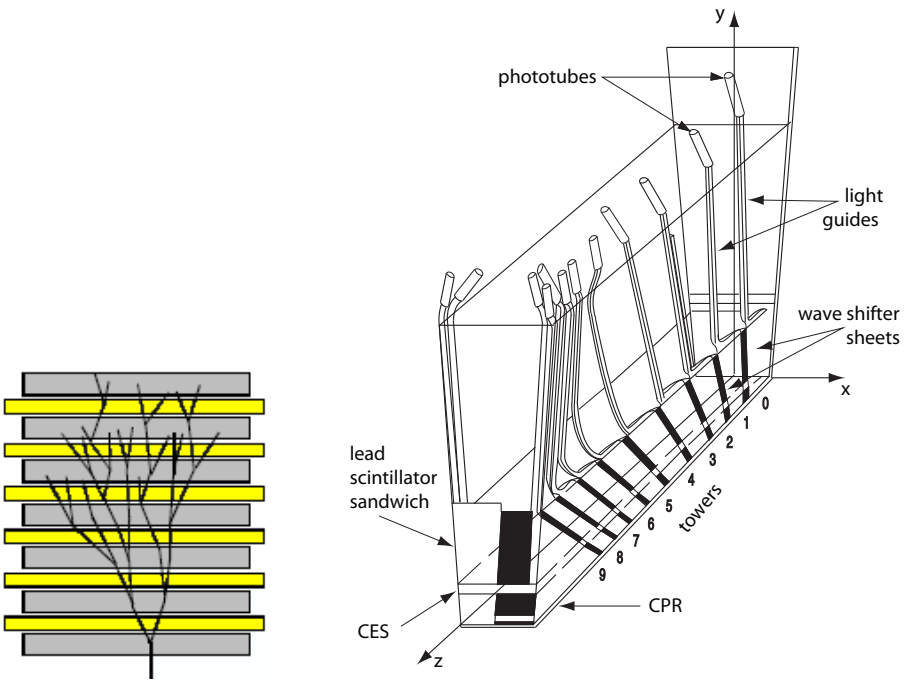

Figure 2.21. On the left, a drawing of a sampling calorimeter shows the interleaved absorber and scintillator layers. The incoming particle enters from the bottom and showers in the first absorber layer. The energy of the particles is measured in the yellow scintillator layers. On the right, the CDF EM calorimeter system occupies the lower third of a wedge of the central calorimeter. The hadronic section fills the empty part in the upper y direction.

The CDF Calorimeters

The two main subsystems of the CDF calorimeter are the electromagnetic calorimeter and the hadronic calorimeter. In the construction of these calorimeters, they were segmented into a few major sections. Each section has slightly different parameters. The electromagnetic calorimeter is divided into three parts. The central calorimeter is a large cylinder surrounding the tracking chamber, while the area closest to the beam is covered by a "plug" calorimeter on both sides of the detector. The hadronic calorimeter also has central and plug parts, as well as another system in between called the"wall" hadronic calorimeter. All of these systems are described in more detail below.

The central calorimeter is made up four free-standing arches, as shown in Figure 2.22. These large arches fit around the center of the CDF tracking systems, two

on each side, to cover all 360 degrees of ϕ. The arches are divided into 12 units called wedges. Each wedge covers 15 degrees of ϕ, and it is further segmented in η into "towers."

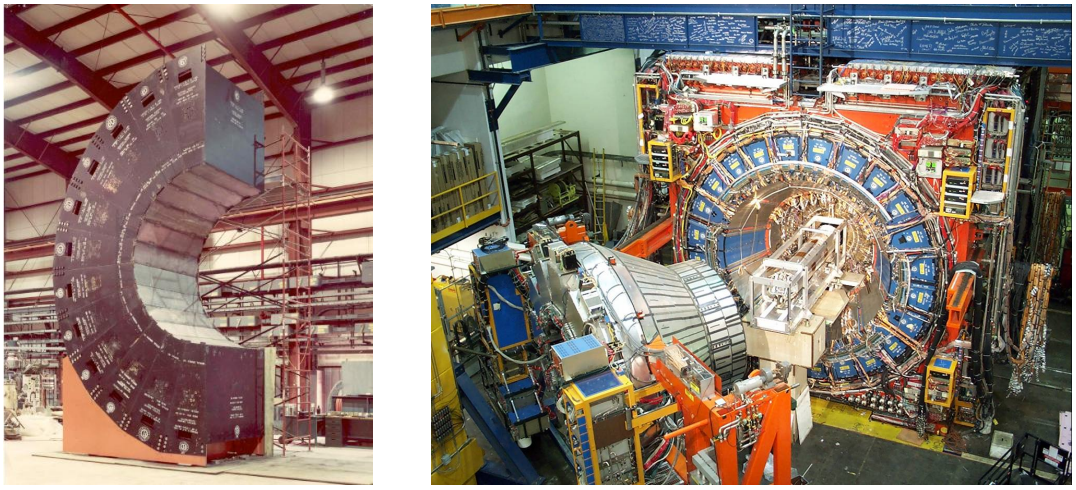

Figure 2.22. An arch of the central calorimeter is shown on the left. It is segmented into 12 wedges. On the right, the plug calorimeter and 48 blue wedges of the wall hadron calorimeter can be seen.

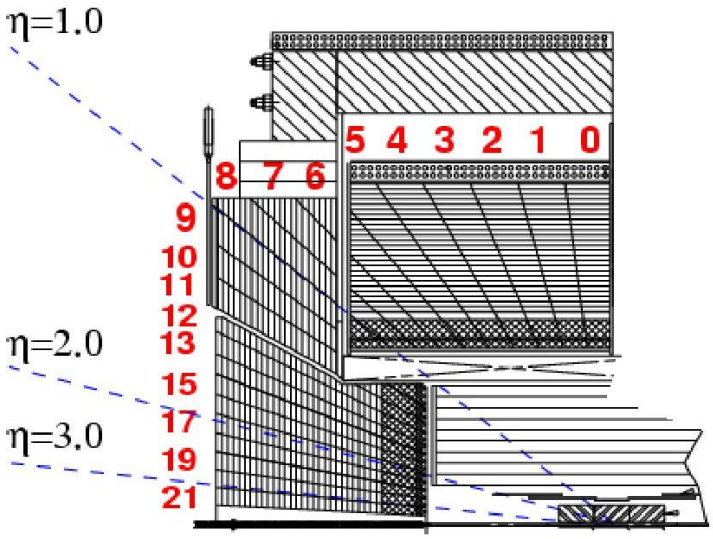

Figure 2.23. Each quarter of the detector has 21 calorimeter towers. Towers 0-5 have both electromagnetic (EM) and hadronic (HAD) parts inside the central calorimeter. Towers 6-9 have EM coverage in the central region, while their HAD information comes from the central and wall hadronic calorimeters. Towers 10-11 have EM parts in the plug, and their HAD parts are only wall hadronic calorimeter towers. Towers 12-21 use the plug EM and HAD calorimeters.

The central electromagnetic (CEM) calorimeter has 10 towers in each wedge (Fig-

ure 2.21). The towers are shown, numbered, in Figure 2.23. Each tower has 31 interleaved layers of 5 mm thick SCSN-38 polystyrene and 3.175 mm of lead. These layers provide 18 X_0 of material.

The central hadronic (CHA) calorimeter is designed with 8 towers per wedge. (The last two EM towers are covered by the wall hadronic calorimeter.) The CHA is made of steel and acrylic scintillator[8] plates, 4.7 interaction lengths deep.

The wall hadronic (WHA) calorimeter fills in the gap between the central and plug calorimeters. It was built at the same time as the central hadronic calorimeter, so its parameters are similar. A wedge of the WHA (visible in Figures 2.22 and 2.23) has only 6 towers with 15 layers of steel and scintillator per tower, 4.5 λ_0 deep.

The plug calorimeters cover the rest of the space between the other calorimeters and the beam pipe. They are found between 1.1 to 3.6 in η (3 to 37 degrees) on either side of the detector. While the central and wall calorimeters have been part of CDF since the 1980's, the plug calorimeters are newer systems, built for CDF Run II. They have the same sampling structure as the others. There are EM and HAD sections (Figures 2.12 and 2.23) made up of towers with wavelength-shifting fibers to carry signals from the scintillator out to PMT's. The plug EM calorimeter (PEM) is made of 23 layers of lead (4.5 mm thick) and SNSC38 scintillator (4 mm). The 12 towers in η are divided into 24 or 48 wedges in ϕ, depending on the proximity to the beam. The plug hadronic calorimeter (PHA) has 23 more layers, alternating 2 inches of iron, and 6 mm of the same scintillator. From 10 to 3 degrees in θ, stainless steel is also used as an absorber. Each plug has 480 channels of EM calorimetry and 432 channels of hadronic calorimetry.

There are two more types of detectors embedded in these calorimeters: preshower detectors and shower-maximum detectors.

[8]The scintillator is Polymethylmethacrylate (PMMA) doped with 8% Napthalene 1% Butyl-PBD and 0.01 % POPOP.

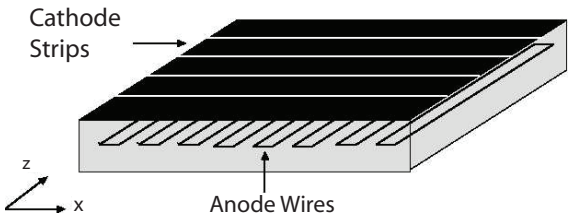

Figure 2.24. This module of the central shower-maximum detector (CES) has wires in the z direction and strips in the x direction.

Preshower detectors are the first layers of scintillator that particles hit in the calorimeter. They can detect lower energy particles that would vanish in the first layer of absorber. They also help discriminate between photons, electrons, and pions. The central preshower detector (CPR) is formed by two wire chambers between the solenoid and each wedge in the calorimeter. The chambers have 32 wires which provide an $r - \phi$ view.[9] The plug preradiator (PPR) is actually the first layer of scintillator in the PEM, behind a 1.27 cm layer of stainless steel. The other layers of scintillator are 6 mm thick, but the PPR is 10 mm thick.

The shower-maximum detectors also aid in discrimination between different particles. They are positioned inside the EM calorimeters in the central and plug regions. The central shower-maximum (CES) detector is a wire chamber, embedded to assist with position determination. It is located between the eighth lead layer and the ninth scintillator layer at 5.9 X_0 (including the solenoid). This distance is chosen because the shower created by an electron in the calorimeter should deposit the most energy at that depth. It is made of 64 anode wires in the z-direction and 128 orthogonal cathode strips, shown in Figure 2.24. The gas mixture is 95% Argon and 5% CO_2. For a 50 GeV electron, the position resolution of the CES is 2 mm. This allows much better track-shower matching than the central calorimeter alone.

The plug shower-maximum (PES) detector is located in the plug EM calorimeter, at about 6 radiation lengths. Each plug has a PES constructed out of 8 wedges, 45

[9]The CPR is being upgraded to a scintillating tile detector during Run II.

degrees each in ϕ. The wedges are double-sided, with 200 scintillating strips at a 45 degree angle on either side, for a total of 3200 strips per plug.

System	CEM	CHA	WHA	PEM	PHA
Coverage in $\|\eta\|$	< 1.1	< 0.9	0.7 to 1.2	1.1 to 3.6	1.1 to 3.6
Towers per Section	10	8	6	12	11
Sections	48	48	48	24/48	24/48
Channels	958	768	576	960	864
Thickness	18 X_0, 1 λ_0	4.7 λ_0	4.5 λ_0	21 X_0, 1 λ_0	7 λ_0
Samples	31	32	15	21 + preshower	23
Active	5 mm	1 cm	1 cm	4 mm	6 mm
Passive	3.175 mm Lead	2.5 cm Steel	5 cm Steel	4.5 mm Lead	2 inch Iron
Resolution	$13.5\%/\sqrt{E} + 1.7\%$	$50\%/\sqrt{E} + 2\%$	$75\%/\sqrt{E} + 4\%$	$14.4\%/\sqrt{E} + 0.7\%$	$74\%/\sqrt{E} + 4\%$

Table 2.1. All of the calorimeter systems are described in detail. The number of sections in ϕ of the PEM and PHA changes as the modules get closer to the beam. Each tower in the central and wall calorimeters has two phototubes, so the number of channels is twice the number of towers.

2.2.3 Muon Detectors

Outside of the calorimeter, the final subsystem looks for those heavier cousins of the electrons, the muons. Muons detectors take advantage of the fact that muons react much less than most other particles produced in the collisions. They are charged particles, so they leave a track in the silicon and central drift chambers, but they pass through the calorimeter without leaving much energy behind. The calorimeters are designed to absorb all the energy of the rest of the particles; no other leptons or hadrons should get through to the muon detectors. There are additional pieces of steel placed outside of the calorimeter to absorb any non-muon particles.

CDF's muon detectors are made of single-wire drift chambers, collected into multi-cell modules. A muon ionizes the Argon-Ethane gas inside the tube. The ions in the gas drift to the central wire, and, just like in the central drift chamber, an avalanche of charge produces a pulse on the wire. Putting together the drift times from several adjacent cells gives the position of the muon as it traversed the chamber (Figure 2.25).

The muon system at CDF is made up of a collection of chambers of different ages and designs, described in Table 2.27. One of the systems is shown in Figure 2.26.

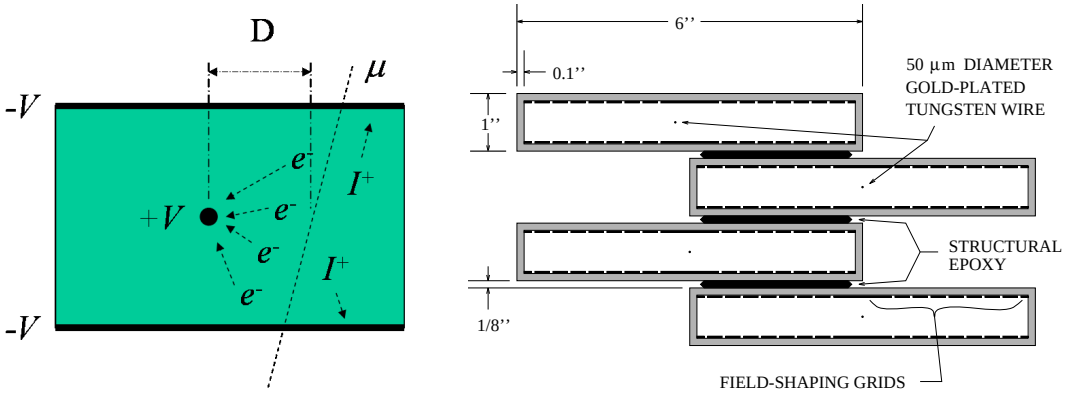

Figure 2.25. A muon (μ) travels through this single cell creating electrons which travel towards the wire and ions which travel to the edges of the cell. The distance (D) is used to calculate the position of the track. On the right, cells from the CMP system are shown.

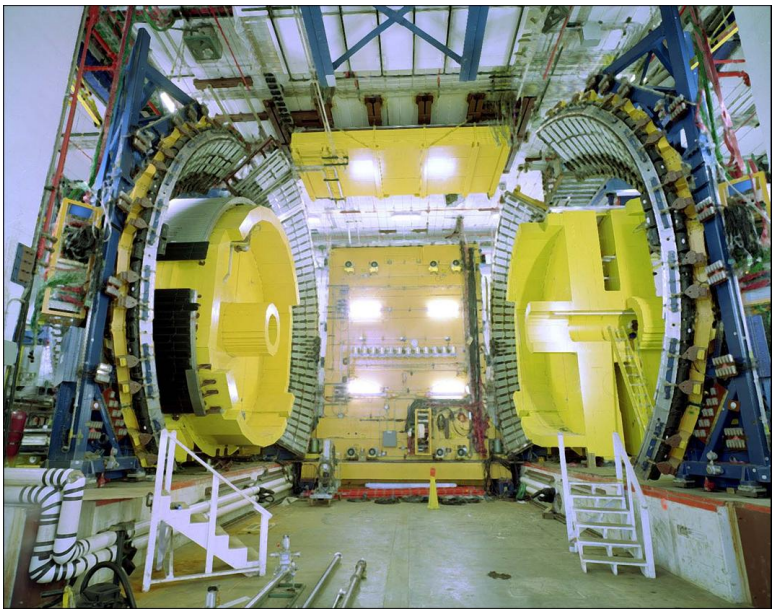

Figure 2.26. The black and white arches of the central muon extension (CMX) system can be seen in the detector hall, before the rest of CDF is put in place in the center.

2.2.4 Measuring Luminosity

The detector that is closest to the beam measures the number of interactions that occur as the beams collide. The intensity of collisions is very important for measuring the rates of processes. The denominator of a rate is the total number of opportunities for a process to occur, which is related to the integrated luminosity. The luminosity (defined in Section 2.1.3) is measured at CDF with a device called the Cherenkov

chambers/counters	$\|\eta\|_{min}$	$\|\eta\|_{max}$	$\Delta\phi°$	T_{drift} (max)	#chan.
Central muon (CMU)	0.0	0.6	360	800 ns	2304
Central muon upgrade (CMP/CSP)	0.0	0.6	360	1500 ns	1076/274
Central muon extension (CMX/CSX)	0.6	1.0	360	1600 ns	2208/324
Intermediate muon (BMU/BSU-TSU)	1.0/1.0-1.3	1.5/1.5-1.5	270/270-360	800 ns	1728/432-144

Figure 2.27. All the CDF muon systems are described. The CMU, CMP, CMX, and BMU are made up of wire drift chambers. The CSP, CSX, BSU, and TSU are scintillating counters that can be used in the trigger to remove out-of-time backgrounds.

Luminosity Counter (CLC).

The system is made up of two identical detectors, placed very close to the beam ($3.7 < \eta < 4.7$) on the east and west sides of CDF (Figure 2.12). Each one has 48 counters, in three concentric rings of 16 counters (Figure 2.28). Each counter is made of a reflective aluminum-mylar cone, surrounding an area filled with isobutane gas. Energetic particles entering the counters emit Cherenkov light,[10] which is directed by the cone to a Photo-Multiplier Tube (PMT). The PMT's convert the light into an electrical pulse, as in the calorimeter.

Several methods are used to convert this information into luminosity measurements. For all of these methods, the rate of proton-antiproton collisions can be calculated from the number of particles entering the CLC modules. Counting channels over some threshold is one measure, but it saturates at high luminosity. Counting the total number of particles entering the CLC is possible, by looking at the energy in each channel. For both of these methods, coincidences in the east and west detectors indicate that a collision has occurred. In another approach, if neither detector has any channels above a threshold, an empty bunch crossing is noted. Counting empty

[10]Cherenkov light is emitted when a particle is traveling through an insulating medium faster than light travels in that medium.

Figure 2.28. The Cherenkov Luminosity Detector is made up of two of these modules, one on each side of the detector.

bunch crossings gives an estimate of the Poisson distribution by measuring the zero bin. More sophisticated treatment of the energies to obtain the final luminosity numbers is done later, offline. Comparisons of the proton-antiproton cross section to other well-known cross sections are also made to verify the luminosity calculations.

It is also important to understand the uncertainty on the luminosity, because it is propagated through to the uncertainty on any rate. The leading systematic is experimentally irreducible. The total cross section of the proton-antiproton collisions is used to calculate the luminosity from the observations of the CLC (Figure 2.29), but it is only known to 4%. The next leading uncertainty is due to the CLC acceptance. Simulation of the geometry of the detector is performed using the PYTHIA and GEANT programs that are described in more detail in Chapter 4. Maps of the detectors and their materials are used, as well as the best understanding of the proton-antiproton collisions, but the acceptance numbers are only certain to 4%. Combining these two uncertainties and other smaller systematics yields a total systematic uncertainty of 6%. The statistical uncertainty is negligible, compared to the systematic uncertainties.

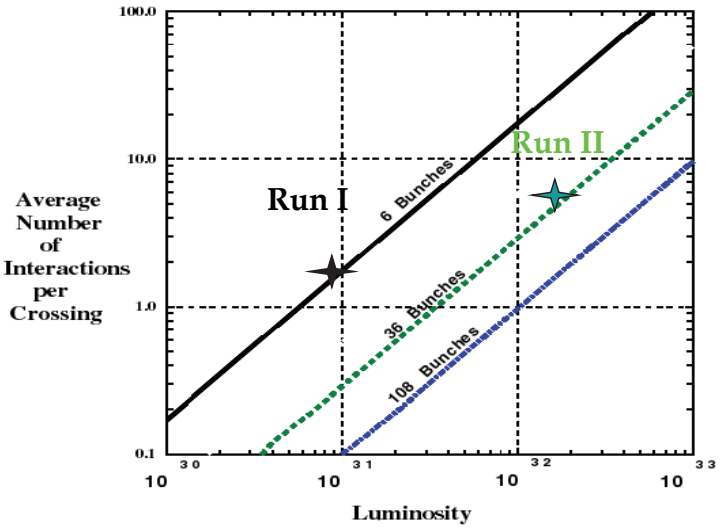

Figure 2.29. The Tevatron's Run I (black line) lasted from 1992-1996. Run II began in 2001 with 36 bunches of protons and 36 bunches of antiprotons colliding at a slightly higher energy. Another scenario with 108 bunches was explored but not put into practice.

2.2.5 Triggering Systems

Each detector subsystem that has been described so far has potential output for every event, but not every event is recorded. The proton and antiproton beams cross in the center of the CDF detector every 396 ns, a rate of 1.7 MHz.

There are several reasons to limit the number of events that are recorded. The speed of incoming events is too fast to read all the data from the detector, and even if all the events could be recorded, the disk space and cost would be prohibitive. If data from every beam crossing were saved, most of the events would be well-known processes, not worth reexamining. Scientists analyzing the data would want to filter the entire dataset into a smaller subsample. The CDF trigger system does some of that filtration as the data is being taken.

The trigger system is divided into three levels. Each event at CDF is examined at Level 1, and if it is deemed sufficiently interesting, it is passed on to Level 2. A Level 2 decision is computed, and if the event still looks interesting, it proceeds to Level 3 for the final decision: whether it is recorded or discarded. The rates of

events at each level are given in Figure 2.30. At each level, they are many reasons that an event can be promoted for further consideration. Interesting features include a high-momentum track in the tracking system, a high-energy cluster of energy in the calorimeter, a muon candidate consisting of hits in the muon chamber and a track that points to them, and a large amount of missing transverse energy in the calorimeter.

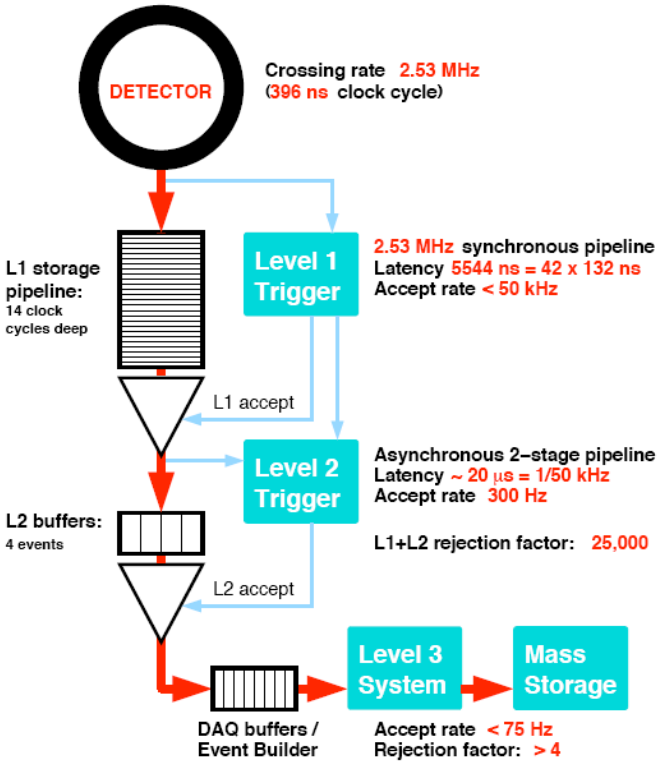

Figure 2.30. A synopsis of the CDF trigger system and its rates. Level 1 output is limited by Level 2 input, Level 2 output is limited by the Event Builder software that comes after it, and Level 3 output is limited by the rate at which events can be written to tape.

There is more time to make a more sophisticated decision as each event progresses through these levels. The Level 1 trigger is a synchronous hardware trigger: events are stored in a pipeline with each event following immediately after the previous one. Each decision must be made in a fixed time, approximately 5 μs after the beams collided that produced that event. At Level 2, there are four data buffers, so four events can be processed in parallel. This is an asynchronous trigger, with an average

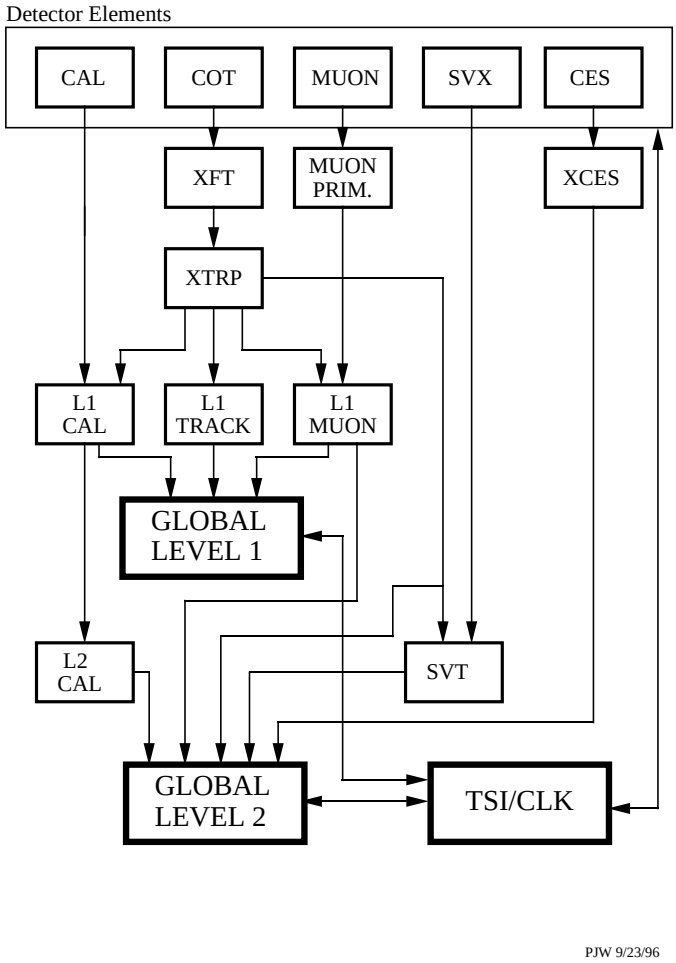

Figure 2.31. A more detailed view of the trigger system shows the detector elements at the top. The arrows show the flow of data from the subsystems used in the Level 1 and Level 2 decisions. The boxes in between (*e.g.* XFT, SVT) represent intermediate trigger systems, which provide information for the final decisions. The TSI/CLK is the trigger supervisor/clock.

decision time of 30 μs. A buffer must be free before another event can be loaded into it, so decision times that are too lengthy lead to full buffers and missed events. At Level 3, all the data from the event are sent to a node in a farm of Linux PCs, so there are as many buffers as nodes. The Level 3 farm runs the full reconstruction software on the events, and the information from all of the subsystems is available. Level 3 has the luxury of 1 second, on average, of processing time per event.

As the event goes through each level of triggering, the objects in the event that

correspond to physical objects are better defined and tighter cuts can be made on them. At Level 1, a calorimeter trigger may pass along any events with any calorimeter tower with an energy greater than some value. At Level 2, the towers are clustered to join adjacent towers into one cluster object. Then, the event is accepted if it has any cluster above some energy. The Level 3 requirements can be the most complex since they have the most time for event reconstruction. If the cluster in the calorimeter matches a track and looks like a high-energy electron, the event that it appears in will be kept. The systems that contribute to the Level 1 and Level 2 triggers are shown in Figure 2.31.

If the trigger choices are too narrow-minded, interesting events could be excluded from the data sample, because they aren't recognized as noteworthy. When designing the trigger, all potentially useful signals must be considered. At the same time, if the trigger is designed too permissively, too many events may be accepted, and they will clog the bandwidth. This could lead to a loss of the few unique and important events that could lead to discovery. Once an event is missed by the triggering system, there is no way to recover it.

Within such a large experiment, trigger decisions must also be based on physics priorities. Very high rate processes, such as some b quark events, will take up all the data space they are allowed. Scientists working on precision measurements must make a case for the amount of data they need, with this process happening so many times per second, not all of the instances need to be recorded. For very rare or unobserved processes, specific triggers are designed to capture every event that comes along. The current data reduction rate is 1 recorded event for every 23,000 events.

CHAPTER 3

Theoretical Foundations and Definition of R

The Standard Model (SM) of particle physics, described in the Introduction, has been very experimentally successful. Physicists expect that new theories will extend its basic ideas, rather than replace them. Since the SM can not explain all of the phenomena that are observed, new theories or extensions are needed. Measurements at large high-energy colliders like the Tevatron help define the SM and other theories by providing information about the types of particles that exist, their properties, and their interactions.

In particular, looking at W and Z bosons at CDF gives us important information about the weak force in the Standard Model. The W's and Z's are the carriers of the weak force, and it essential to understand their production and decay. With well-identified samples of W's and Z's their properties can be examined as part of a program to understand all of the forces.

To put these measurements in context, the particles that make up the Standard Model are described in more detail in this chapter. Then, the interactions between the particles, and the mathematics of their production and decay, are explained. The cross section, branching ratio, and width are defined and the R ratio measurement is introduced in Section 3.3.3.

3.1 The Particle Zoo

3.1.1 Fermions and Bosons

There are two types of basic building blocks: fermions and bosons. All the fundamental particles shown in Table 1.1 can be divided into these two groups. The difference between the two types of particles is best displayed in close quarters. Bosons can be packed closer and closer together, with no limit on the number of the same kind of particles that can be in the same space. Most of our everyday experience with matter happens with objects that are *not* made of bosons. Consequently, the idea of particles occupying the same space seems strange, but very dense collections of bosons have been created in the laboratory (Figure 3.1). While there are many kinds of bosons, the best-known is the photon.

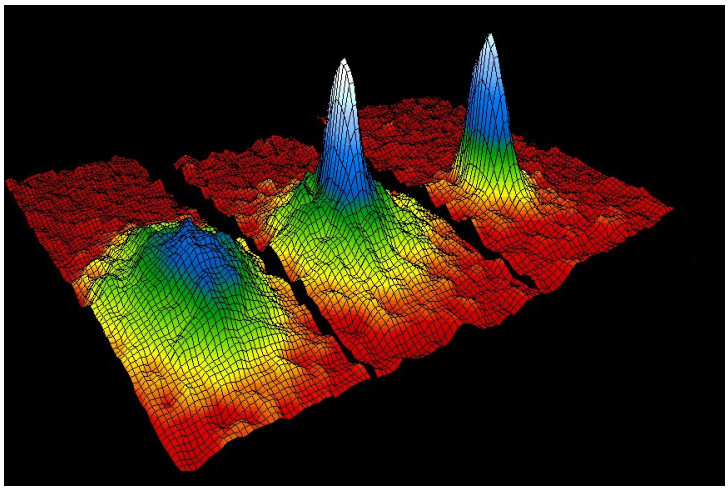

Figure 3.1. As a gas of bosons is cooled towards absolute zero, they enter the same quantum state. The peaks shown here are the velocities of the bosons (rubidium atoms) before they condense (on the left) and as they obtain almost identical velocities (right). The 2001 Nobel Prize was awarded for this observation [15].

Fermions are more familiar particles: electrons, protons, and neutrons are examples of fermions. Unlike bosons, two identical fermions cannot occupy the same space at the same time. This is known as the Pauli Exclusion Principle, and it has far-reaching consequences. For example, the configuration of the different orbital levels

of the atom arises from this principle. Therefore, the exclusion principle determines the reactivity of the elements and the structure of the periodic table of elements (Figure 1.1).

While fermions are the particles that everything is made from (electrons and protons), bosons are the particles that transmit forces (like the photon, the W and the Z). The reason for the different behavior has to do with a property of matter called spin.[1] Bosons have spins that come in integer multiples of the constant $\hbar$ (0, 1, ...) while fermions have spins in half-integer multiples (1/2, 3/2, ...). Although the name seems to indicate that particles are actually spinning like tops or planets, it is better to think of spin as an intrinsic property of fundamental particles, like their electric charge. The name is used because of the mathematical relationship between spin and angular momentum.

Types of Fermions

There are two major groups of fermions, from which all other matter particles are formed. These are the leptons and quarks.

The lepton family is made up of the electron, the electron-like muon and tau particles, and three neutrinos (Figure 1.3). All six leptons have been observed experimentally, with the tau-neutrino as the most recently discovered. It was observed by the DONUT collaboration at Fermilab in 2000 [20]. Electrons are crucial to the formation of atoms, but there are no long-lasting particles formed exclusively of leptons.[2]

In contrast, quarks have not been observed outside of composite particles. Quarks combine into color-neutral arrangements of two or three quarks, called hadrons.

[1] The term "spin" is also used loosely to refer to both the intrinsic angular momentum (all electrons have spin 1/2) and the spin in a particular direction (-1/2 or +1/2, referred to as "spin up" and "spin down").

[2] An electron and a positron can form a particle called positronium, but the oppositely charged leptons spiral towards each other and annihilate quickly.

Hadrons with two quarks ($q\bar{q}$) are called mesons; three-quark objects (qqq) are baryons. The proton (up, up, and down quarks) and neutron (up, down, down) are examples of baryons. Examples of mesons are not as well-known, but they are very copiously produced at collider experiments. The most common ones are the pions (made of up and down quarks and antiquarks) and kaons (*e.g.* $u\bar{s}$).[3]

When quarks and gluons are produced in colliders, they form larger particles immediately in a process called hadronization. These particles decay and interact and form a spray of particles called a "jet." An example of hadronization can be seen in Figure 3.2.

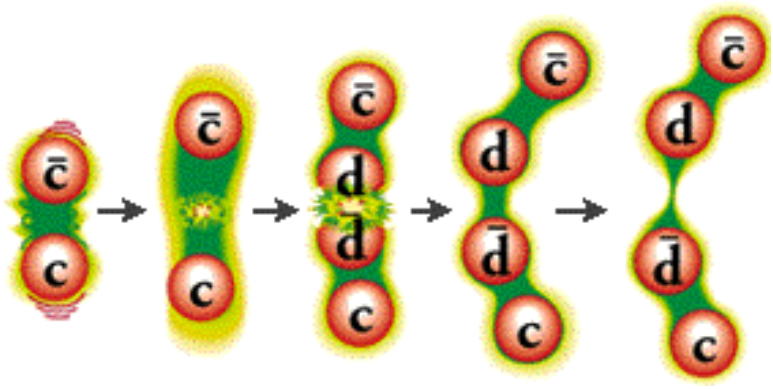

Figure 3.2. As charm and anticharm quarks become separated, the energy of the color field between them increases. When the energy is great enough, a down and antidown quark are created, forming mesons with the original $c\bar{c}$ quarks. [30]

Types of Bosons

As described in the Introduction, each of the fundamental forces must come in discrete units. These quanta can be thought of as the carriers of the force, but they really *are* the force itself. These force-transmitting particles are all bosons. The strong force (also called Quantum Chromodynamics or QCD) has a set of bosons called gluons (g). The electroweak force has four types of bosons: the photon, the W^+, W^-, and the

[3] A particle type with a bar over it indicates an antiparticle. The up quark is u, so the antiup is denoted $\bar{u}$. Some particle-antiparticle sets are conventionally represented by their charges instead of bars, like the $W^+$and W^-.

Z. Gravity has not been successfully incorporated into the SM, but if it is described by a quantum field theory, it will have a spin-2 boson named the "graviton." Gluons, photons, W's and Z's have all been observed, but gravitons have not.

The Higgs boson is another important boson in the SM, as yet unobserved. The Higgs particle is needed to explain the mechanism that accommodates bosons with heavy masses like the W and Z, while the photon remains massless. The search for experimental evidence of the Higgs boson continues at Fermilab and at CERN in Geneva, Switzerland.

Composite particles can also be bosons. When spin one-half particles combine to form a helium atom, their spins also combine. With two electrons, two protons, and two neutrons, ^{4}He is a boson.

3.1.2 Standard Model Interactions

The set of particles above, summarized in Table 1.1, cannot all interact with one another in the Standard Model. The gluons, for example, do not interact with electrons because electrons have no color charge. Interactions between particles in the model are summarized using a Lagrangian density. Each term in the expression relates different particles, with constants in proportion to the strength of the coupling of those particles. The Lagrangian density is used because it is locally defined (a point in time-space is only affected by the time-space around it), and a Lorentz scalar (it is invariant under special-relativistic transformations). To minimize the action of the field, the Lagrangian density is integrated over all space-time.

The Lagrangian for the lightest set of fermions (electron (e) and electron neutrino (ν), up (u) and down (d) quarks) is shown here:

$$
\begin{aligned}
\mathcal{L}_{SM} &= g_1 \sum_{f=\nu,e,u,d} Q_f(\bar{f}\gamma^\mu f)A_\mu \\
&+ \frac{g_2}{cos\theta_w} \sum_{f=\nu,e,u,d} \Big\{(\bar{f}_L\gamma^\mu f_L)[T_f^3 - Q_f sin^2\theta_w] + (\bar{f}_R\gamma^\mu f_R)[-Q_f sin^2\theta_w]\Big\}Z_\mu \\
&+ \frac{g_2}{\sqrt{2}}\Big[\Big\{(\bar{u}_L\gamma^\mu d'_L) + (\bar{\nu}_L\gamma^\mu e_L)\Big\}W_\mu^+ + \Big\{(\bar{d'}_L\gamma^\mu u_L) + (\bar{e}_L\gamma^\mu \nu_L)\Big\}W_\mu^-\Big] \\
&+ \frac{g_3}{2} \sum_{q=u,d} (\bar{q_\alpha}\gamma^\mu \lambda^a_{\alpha\beta} q_\beta) G^a_\mu
\end{aligned} \tag{3.1}
$$

The fermions and antifermions are represented by f and $\bar{f}$. The electromagnetic, weak, and strong interactions are described by different terms, as follows. The first line shows the interaction of a fermion and antifermion with the photon (A_μ). The electric charge of the fermion is Q_f. This term will disappear for the neutrino, since it has $Q_f = 0$; the lack of a non-zero term containing a ν and an A_μ means that neutrinos and photons do not interact. The next two lines describe the interactions with the W and Z bosons, while the last line shows the quarks coupling to the gluons (G^a_μ). T_f^3 is a scalar which describes the coupling of the fermion to the Z. Other important pieces to understand include constants for each of the strengths of the forces (g_i), standard matrices that are used throughout Quantum Field Theory ($\gamma^\mu, \lambda^a_{\alpha\beta}$, defined in [25] for example) and θ_w, which is the Weak or Weinberg angle.

In the Lagrangian above, sometimes the fermions have subscripts of L and R. These reflect the way that the weak force in the Standard Model treats "left-handed" and "right-handed" particles differently. A particle's handedness is defined by its spin and momentum. When the spin is along the direction of motion, a particle is said to be right-handed. If the spin is opposite the motion, it is left-handed. For massless particles, like the photon, the handedness (also called "chirality") is fixed. For a massive particle, it is always possible to switch reference frames so that it appears to switch chiralities. This means that massive electrons are produced left-handed by the weak process, but as they move they can oscillate between left- and right-handedness.

To further complicate the picture, quarks are known to change flavors. The d'

that interacts with the weak force in the Lagrangian is not just a d quark, but a mixture of d, s, and b. The relationship between the quarks is given in the Cabibbo-Kobayashi-Maskawa (CKM) Matrix. It has nine elements, shown below:

$$\begin{pmatrix} d' \\ s' \\ b' \end{pmatrix} = \begin{pmatrix} V_{ud} & V_{us} & V_{ub} \\ V_{cd} & V_{cs} & V_{cb} \\ V_{td} & V_{ts} & V_{tb} \end{pmatrix} \begin{pmatrix} d \\ s \\ b \end{pmatrix} , \tag{3.2}$$

The largest elements are along the diagonal of the matrix. This means that a u quark reacting with a W will most often produce a d, but sometimes it will produce an s, and very rarely, a t.

The recent discovery of neutrino masses and neutrino mixing means that fermion mixing is not confined to the quark sector. A matrix for neutrino mixing has also been formed, called the Maki-Nakagawa-Sakata (MNS) matrix.

3.1.3 Symmetries in the Standard Model

The Lagrangian gives the allowed interactions and their strengths, but it does not explain *why* those interactions are the ones that happen in nature. Similarly, conservation rules are taught to early physics students as laws to be obeyed, but the reason behind the laws may not be stated. The basis for both the form of the Lagrangian and the conservation of energy and momentum has the same root: symmetry.

A symmetry of physical laws refers to a mathematical change which leaves the resulting equations invariant. For example, changing the time in a set of equations of motion from t to $t + \Delta t$ does not affect the result: the equations are invariant under a translation in time. This invariance leads to the conservation of energy. Invariance under translations in space leads to conservation of momentum. Rotational symmetry is reflected in the conservation of angular momentum, and electric charge is conserved because of gauge invariance in the equations of electromagnetism. This relationship between symmetry and conserved quantities is called Noether's theorem [25].

Symmetry in the Standard Model is described in terms of group theory. The representations of the groups that are used are matrices. U(n) is a mathematical group of $n \times n$ unitary matrices. If all the matrices have their determinants equal to 1, the group is called "special unitary," or SU(n).

Using this terminology, the group structure of the Standard Model is SU(3) $\times$ SU(2) $\times$ U(1). The SU(3) portion corresponds to the strong force, and the 8 generators of the group are the 8 gluons. SU(2)$\times$U(1) is the electroweak part. The four generators are not the same as the observed bosons (W^+, W^-, Z, and the photon) but they mix to form them. This interaction of the electromagnetic and weak forces is the electroweak unification.

3.2 Production and Decay

To test the form of the Standard Model, particles are smashed together at great speeds at high-energy collider machines. In the resulting collisions, new particles can be produced. For a given number of collisions, the Standard Model should predict the outcome of the interactions. For every 1000 times a proton and antiproton collide, how many b quarks are expected to be produced? How many t quarks? How many W's and Z's?

To answer these questions, the steps of the process must be examined one at a time. First, how often to the proton and antiprotons collide, and how often do they produce a particular particle or set of particles? Then, if the new particles decay, what particles do they decay into?

3.2.1 Production Cross Sections and Luminosity

In order to understand how often protons and antiprotons collide, one must have information about the beams of particles. The number and density of particles in the beams determine the luminosity. The calculation of luminosity using parameters of

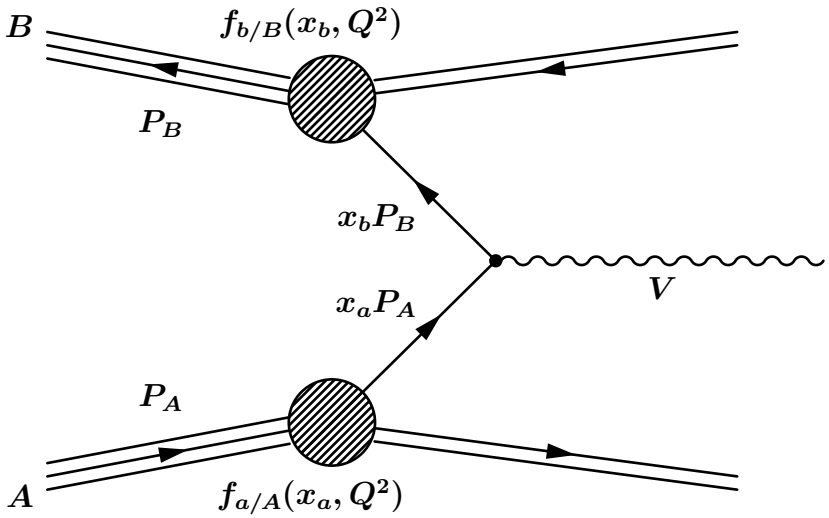

Figure 3.3. The proton and antiproton (A and B) with momenta P_A and P_B interact to form particle V. The two quarks that are annihilated each carried a fraction (x_i) of the momentum of the incoming hadrons (P_A and P_B). The process taking place in the shaded circles will be explained in more detail in Section 3.2.2. In this and other Feynman diagrams, time proceeds to the left. Forward arrows are particles, while arrows going backwards in time are antiparticles. The lines do not represent actual paths that the particles travel.

the accelerator was described earlier in Section 2.1.3.

To get the number of expected collisions, N, the luminosity, $\mathcal{L}$, is needed, and also σ, the cross section.

$$\mathcal{L} \cdot \sigma = \mathsf{N}$$

In general, a cross section describes the opacity of a target. For a solid sphere like a billiard ball, the cross section is simply the cross-sectional area of the ball: πr^2. For a charged particle passing an oppositely charged particle, the cross section is larger than the area alone, since the electromagnetic force is a long-range force.

3.2.2 Proton-Antiproton Cross Section

Proton collisions are complicated, because the protons are made up of smaller particles: quarks and gluons. It's not as simple as calculating how often a proton and antiproton interact; it is important to know which of the constituent particles inside

the proton and antiproton did the interacting, and how much of the energy of the larger particles they were carrying at the time of interaction.

For the creation of a particle V from a proton and antiproton (A and B) collision, as shown in Figure 3.3:

$$\sigma = \sum_{a,b=q,\bar{q},g} C_{ab} \int f_{a/A}(x_a, Q^2) f_{b/B}(x_b, Q^2)\ dx_a dx_b\ \hat{\sigma}. \tag{3.3}$$

The initial particles (a and b) can be quarks, antiquarks, or gluons inside the proton and antiproton. C_{ab} is a color-averaging factor equal to $\frac{1}{9}$ for quark-quark interactions, $\frac{1}{24}$ for quark-gluon, and $\frac{1}{64}$ for gluon-gluon. The two terms of the form $f_{i/I}(x_i, Q^2)$ are the parton density functions (PDF's) for the hadrons. They express the likelihood of finding a particular kind of parton with a fraction x_i of the hadron's energy, if the process has a momentum transfer of Q. The $\hat{\sigma}$ is the cross section for the process in question, for example, $\sigma(u\bar{d} \to W^+)$.

3.2.3 Decay Amplitudes

Most particles that are produced in the proton-antiproton collisions are unstable. They decay quickly, and the decay products are observed in the detectors that surround the point of interaction. Three concepts used in understanding the decay of particles are the width, lifetime, and branching ratio, and they are defined in relation to one another.

The lifetime (τ) is inversely proportional to the decay rate (Γ) which is also called the full width. For a particle with a very short lifetime, there must be a larger spread in the measured energy, observed as a peak with some width (Figure 3.4).

Branching ratios ($Br(V \to X)$) give the fraction of all particles V that decay into a final state X. The branching ratio is used to define the partial width (Γ_X), in terms of the full width:

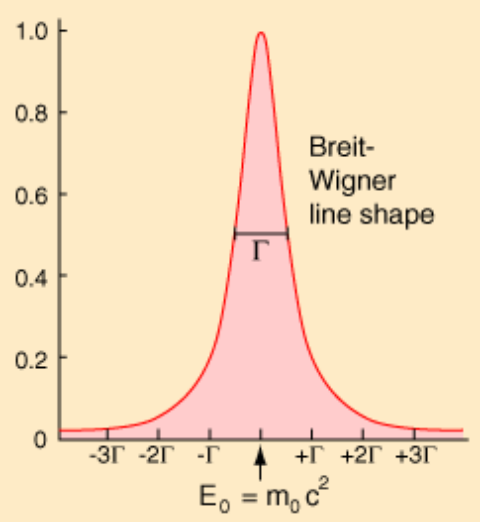

Figure 3.4. For a particle with mass m_0, the measured energies form a Breit-Wigner distribution. The width (Γ) is measured at half of the maximum. For particles with a lifetime too short to be measured directly, the width is used to infer the lifetime.

$$Br(V \to X) = \frac{\Gamma_X}{\Gamma} = \frac{\Gamma_X}{\sum_i \Gamma_i}. \tag{3.4}$$

For any process, the cross section times the branching ratio yields the total number of expected events, per unit of integrated luminosity. It summarizes how often an intermediate particle is produced in the collisions and how often it decays to a particular final state (X):

$$\mathsf{N} = \sigma(p\bar{p} \to V) \cdot Br(V \to X) \cdot \int \mathcal{L} dt \tag{3.5}$$

For example, the cross section times branching ratio for $p\bar{p} \to W \to \ell\nu$, measured at CDF is 2775 $\pm$ 10 (stat) $\pm$ 53 (syst) $\pm$ 167 (lum) pb [8]. In each week of data-taking under the current conditions, about 35 pb^{-1} of collisions are delivered by the accelerator to CDF. Multiplying the two numbers, one can see that almost 100,000 W's that decay in the electron channel are produced at CDF each week. Estimating how many of those interactions should be observed after accounting for detector acceptances and inefficiencies is a major part of measuring cross sections and branching ratios.

3.3 The Electroweak Bosons

At Fermilab, W and Z bosons are produced in $p\bar{p}$ collisions by the Tevatron collider (Figure 3.5) and the decay products of these collisions are measured by the CDF and D0 detectors, as described in the previous chapter.

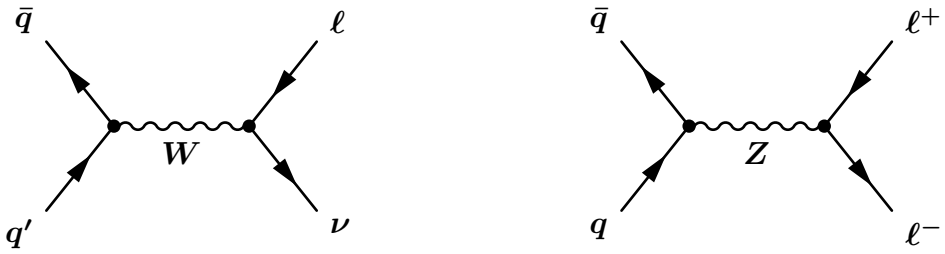

Figure 3.5. These Feynman diagrams show the annihilation of a quark and antiquark to produce W's and Z's which decay leptonically.

3.3.1 The W boson

W Production

To determine the possible ways to produce a particle in the SM, the Lagrangian provides all the information. All the interactions of the W are summarized there, in Equation 3.1.

From the terms involving $W^{\pm}$, the allowed interactions are those involving a W and a pair of leptons $((e, \nu_e)$, (μ, ν_μ), $(\tau, \nu_\tau))$ or a pair of quarks $((u, \bar{d}')$, $(c, \bar{s}')$, $(t, \bar{b}'))$. At the Tevatron, the W is most often produced by up and down quarks, since those are most prevalent inside the protons and antiprotons.

To calculate how often a W boson is produced in a $p\bar{p}$ collision, Equation 3.3 is used. The part of the cross section that depends on the W is given by

$$\hat{\sigma}(u\bar{d} \to W) = \frac{4\pi^2}{3} \frac{\Gamma^W_{u\bar{d}} \Gamma^W_f}{\Gamma_W M_W} \delta(\hat{s} - M_W^2) \tag{3.6}$$

The constants in front depend on the spins and colors of the particles. The partial widths in the numerator are for $W \to u\bar{d}$ and for the W to decay to its final state

(f). The terms in the denominator are the total W width and the W mass. The last term uses a delta function to show that $\hat{s}$, the square of the $u\bar{d}$ center-of-mass energy, must be equal to the W mass squared, otherwise the process can not take place. The derivation of this cross section can be found, for example, in Kane [25].

W Decay and Width

The W lifetime is too short for the boson to be observed before it decays. It must be identified by its decay products. It can decay into the same sets of particles listed in the last section: pairs of leptons and quarks. The top quark (t) turns out to be too heavy for the W to decay into a top and bottom.[4] There are five allowed decays: (e, ν_e), (μ, ν_μ), (τ, ν_τ), $(u, \bar{d}')$, and $(c, \bar{s}')$. In the Standard Model, any one of these five channels would be equally likely, except that there are three different colors of quarks. Each of the quark channels is then three times as likely, so the W decays to $e\nu$ 1/9 of the time. The observation that 2/3 (instead of 2/5) of W decays have quarks in the final state is a verified prediction that there are three different color charges.

The leptonic decay channels of the W and Z (Figure 3.5) where $\ell = e$ or μ are the preferred channels for making precision measurements. The high-energy electrons and muons leave distinct paths in the detector, and few other processes mimic these signals. The third lepton, the τ, is more difficult to identify because it decays within the detector. It can decay leptonically, but the resulting electron or muon will have less energy than the τ that it came from; some energy goes off with neutrinos produced in the decay. There are also τ decays which are hadronic and have multiple high-rate standard model backgrounds. Hadronic decays of the W and Z are also problematic due to other SM background of any event with two quarks in the final state.

[4] There are two processes being discussed, here. One is $W^+ \to t\bar{b}$, and the other is $W^- \to \bar{t}b$. No W can decay into a "top and bottom" quark, because a combination of a top and bottom would have an electric charge of 1/3. It is conventional to refer to two processes at once by dropping the "anti-" prefixes when there should be no confusion.

For $W \to e\nu$, the partial width depends on just a few parameters of the SM [36].

$$\Gamma(W \to \ell\nu) = \frac{G_F\ M_W^3}{6\pi\sqrt{2}} = 227.0 \pm 0.3\ \text{MeV}[32] \tag{3.7}$$

The error is dominated by the uncertainty on M_W. For any of the W decays, the partial width is given more generally by

$$\Gamma(W \to f\overline{f}') = \frac{|V_{ff'}|^2 N_C\ G_F\ M_W^3}{6\pi\sqrt{2}} \tag{3.8}$$

where $V_{ff'}$ is the CKM element for quarks (1 for leptons), N_C is the color factor (3 for quarks and 1 for leptons), G_F is the Fermi coupling, and M_W is the mass of the W.

The total width is the sum of the partial widths, with some corrections due to the hadronization of quarks.

$$\Gamma(W) = 3\Gamma(W \to \ell\nu) + 3\left(1 + \frac{\alpha_s}{\pi} + 1.409(\frac{\alpha_s}{\pi}^2) + \cdots\right) \sum_{\text{[no top]}} |V_{qq'}|^2\, \Gamma(W \to \ell\nu) \tag{3.9}$$

The corrections for the strong force involve α_s which is the coupling strength of the force. It is a free parameter of the SM, related to g_3 in the Lagrangian (Equation 3.1) by $\alpha_s = g_3^2/4\pi$. The momentum scale (Q) of α_s must be specified, as it decreases with increasing Q. The M_W scale is appropriate here, so $\alpha_s = \alpha_s(M_W)$.

The current SM theoretical value for $\Gamma(W)$ is 2092.86 ± 2.8 MeV [32]. The current world average of all measurements is $\Gamma_W^{\text{tot}} = 2139 \pm 44$ MeV [37]. The measurements of the W width still need to be improved before the predictions of the Standard Model will be tested.

W Mass

All of these widths depend on the W mass, which has been recently measured at CDF with new precision. Decays of $W \to e\nu$ and $W \to \mu\nu$ are both examined. The

W mass is measured using the transverse mass:

$$M_T^2 = (E_T^e + E_T^\nu)^2 - (\vec{p}_T^{\,e} - \vec{p}_T^{\,\nu})^2 \tag{3.10}$$

$$= 2p_T^e p_T^\nu (1 - \cos\theta_{e\nu}) \tag{3.11}$$

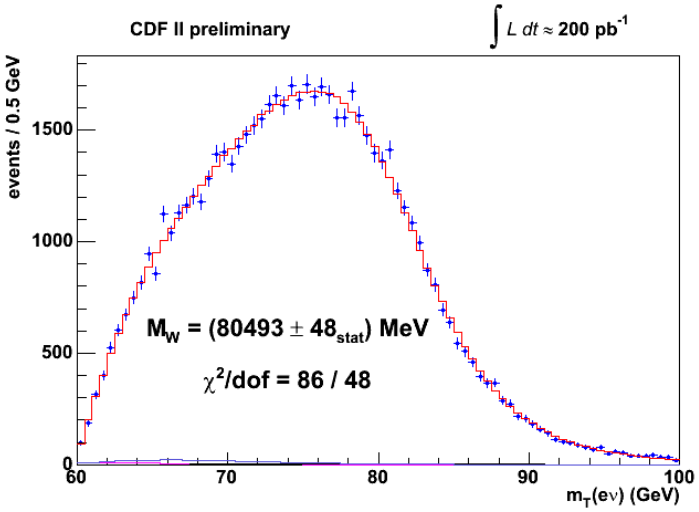

Figure 3.6. This is the transverse mass distribution for the electron channel of the W decays. The blue points show the data, while the red curve is the simulation. Some very small background curves are visible in the bottom left.

Combining the electron and muon channels, they measure $M_W = 80413 \pm 34$ (stat) $\pm$ 34 (syst) MeV/c^2. With a total uncertainty of 48 MeV/c^2, this is the best single measurement of M_W. It brings the world average to 80398 $\pm$ 25 MeV/c^2.

3.3.2 The Z boson

Z Production

Looking at the Lagrangian again, the Z interacts with pairs of quarks (*e.g.* $u\bar{u}$) and pairs of leptons (e^+, e^-). The cross section for producing Z's from quarks at the Tevatron is given by [21]

$$\hat{\sigma}(q\bar{q} \to Z) = \frac{\pi}{3}\sqrt{2}G_F M_Z^2 (g_V^2 + g_A^2)\delta(\hat{s} - M_Z^2) \quad .$$

Most of the terms should be familiar by now, except the g_i terms. They are the vector and axial couplings to the Z:

$$g_V = T^3 - 2Q \sin^2 \theta_W \tag{3.12}$$

$$g_A = T^3 \tag{3.13}$$

where T^3 is defined in Equation 3.1. It can have values of 0 (for right-handed particles) or $\pm$ 1/2 (for left-handed particles).

Z Decay and Width

There are six kinds of leptonic Z decays (Figure 3.5), but only five hadronic ones. Again, the top quark is too heavy for a Z to produce $t\bar{t}$.

The calculation of the partial widths proceeds similarly to the W's widths. Each neutrino pair contributes about 160 MeV to the total Z width. [25] Measuring the Z width allows a calculation of the number of neutrinos, even though $Z \to \nu\nu$ is a nearly impossible process to observe directly. The LEP experiments have measured $\Gamma(Z)$ very precisely, to determine that the number of neutrino families is three. The width is a strong constraint on any model which predicts a new particle that would interact with the Z.

The direct measurement of the Z width is much simpler than the W width, because there is no neutrino from $W \to \ell\nu$ decays to escape detection. The world average for the full width of the Z is 2495.2 ± 2.3 MeV [39].

3.3.3 The Ratio of W's to Z's

The Tevatron program is in a unique position, able to examine the W mass and width more precisely than ever before. The first mass measurement is given above. Both direct and indirect measurements of the W width are in progress. For the direct width measurement, the tail of the transverse mass distribution is used to fit different

width hypotheses. The indirect width measurement is the subject of this thesis, and it proceeds through a ratio, R.

The R measurement gives us information about the production and decay of the weak bosons, since it involves both cross sections and branching ratios.

$$\mathsf{R} = \frac{\sigma(p\overline{p} \to W) \times Br(W \to \ell\nu)}{\sigma(p\overline{p} \to Z) \times Br(Z \to ee)}. \tag{3.14}$$

The leptonic decays are used for this measurement because they provide the best signal to background discrimination. Rearranging the terms using the definition of the width given in Equation 3.15, the W width is in the denominator.

$$\mathsf{R} = \frac{\sigma(p\overline{p} \to W)}{\sigma(p\overline{p} \to Z)} \frac{1}{Br(Z \to \ell\ell)} \frac{\Gamma(W \to \ell\nu)}{\Gamma(W)} \tag{3.15}$$

To extract $\Gamma(W)$, the very precise $Br(Z \to \ell\ell)$ measurements from LEP can be used. The ratio of the cross sections (σ_W/σ_Z) and $\Gamma(W \to \ell\nu)$ can be taken from the SM theory. With these inputs, the total W width can be extracted. This width may be a window into new physical processes: if the W can decay into any non-SM particles, the total width will deviate from the predicted value.

In addition to measuring the W width indirectly, this set of measurements has other uses. By comparing the numerators of R for electrons and muons, lepton universality in W decays is tested. The total width also places a constraint on the CKM elements, as shown in Equation 3.16. The three elements that affect the top quark are not involved, but the other six can be constrained by the width measurement, given the partial leptonic width (Γ^0_W) and the strong coupling constant (α_s).

$$\Gamma_W = 3\Gamma^0_W + 3\left(1 + \frac{\alpha_s}{\pi} + 1.409(\frac{\alpha_s}{\pi})^2 - 12.77(\frac{\alpha_s}{\pi})^3\right) \sum_{\text{[no top]}} |V_{qq'}|^2 \, \Gamma^0_W. \tag{3.16}$$

A Brief History of R

The cross sections and branching ratios of the weak bosons have been measured for over 20 years. The previous work is summarized in Table 3.1, including the recent thesis work of two Michigan graduate students.

Table 3.1. Measurements of the W and Z production cross sections times branching ratios from previous hadron collider experiments are presented along with the measured values of R and the extracted values of $\Gamma(W)$, from [18]. The values of the cross sections change with the center-of-mass energy (as shown, for example, in Equation 3.6). Neither R nor the W width should vary with $\sqrt{s}$. CDF Run II errors are statistical only.

Experiment	$\sqrt{s}$ (TeV)	Mode	$\sigma_W \cdot Br(W \to \ell\nu)$ (nb)	$\sigma_Z \cdot Br(Z \to \ell^+\ell^-)$ (pb)	R	$\Gamma(W)$ (GeV)
UA1 [11]	0.54	e	0.609 ± 0.103	58.6 ± 11.5	10.4 ± 2.0	
UA1 [11]	0.63	$e+\mu$			$9.5^{+1.1}_{-1.0}$	2.18 ± 0.26
UA2 [12]	0.63	e	0.660 ± 0.040	70.4 ± 6.8	9.38 ± 0.86	2.30 ± 0.20
CDF [6, 4, 5, 7]	1.80	e	2.49 ± 0.12	231 ± 12	10.90 ± 0.43	2.064 ± 0.084
D0(Run IA) [1]	1.80	e	2.36 ± 0.15	218 ± 16		
D0(Run IA) [1]	1.80	μ	2.09 ± 0.25	178 ± 31		
D0(Run IA) [1, 3]	1.80	$e+\mu$			10.90 ± 0.49	2.044 ± 0.093
D0(Run IB) [2]	1.80	e	2.31 ± 0.11	221 ± 11	10.43 ± 0.27	2.17 ± 0.07
CDF(Run II) [8, 18]	1.96	e	2.780 ± 0.014	255.8 ± 3.9	10.82 ± 0.18	
CDF(Run II) [8, 18]	1.96	μ	2.768 ± 0.016	248.0 ± 5.9	11.12 ± 0.27	
CDF(Run II) [8]	1.96	$e+\mu$	2.775 ± 0.010	254.9 ± 3.3	10.92 ± 0.15	2.079 ± 0.041
CDF(Run II - AV) [38]	1.96	μ	2.786 ± 0.012	253.1 ± 4.2	11.02 ± 0.18	2.056 ± 0.034
CDF(Run II - JK) [26]	1.96	μ	2.794 ± 0.009	252.1 ± 3.6		

CHAPTER 4

Simulation of the Data

In addition to the data taken with the detector, a great deal of simulated data is used in most analyses at CDF. The simulation contains the current knowledge about the Standard Model physics and the detector implementation. With such complicated detectors and perturbative solutions to the theory, simulations can be used to understand how Standard Model processes will look in the data. The simulated data is used for estimating well-modeled SM backgrounds and detector quantities like geometric acceptance.

Software is used to generate events based on both SM and non-SM processes. Once the events are generated, the outgoing partons undergo showering, where they become sprays of hadronic jets. The final particles are then fed into a detector simulation. The detector simulator takes into account the locations of the subsystems and the different materials in them. It returns simulated data, or "Monte Carlo" (MC) data, that looks like the real data. One advantage to having this simulation is that the modeled data comes with the truth information: after selecting a sample of electron candidates, they can be checked to see how many particles really were electrons.

For this analysis, the simulation is used to study acceptances and backgrounds, as described in the next sections. The PYTHIA program [35] is used to model the hard scattering process, as well as the parton showering. CDF also uses a specific tuning for PYTHIA to model the underlying event [23]. The GEANT program is used to simulate the detector response [17, 10].

150990	154050	154861
151092	154054	155155
151116	154069	168125
151121	154070	175596
151140	154710	176576
151141	154768	176584
151142	154799	176631
151228	154829	176632
151229	154841	176633
151231	154856	177140
151237	154860	178254
		182890

Table 4.1. Run numbers rejected from MC due to generation problem.

Dataset ID	Physics Process	Code Version
`wewkfe`	$W \rightarrow e\nu$	`5.3.3_ewk`
`zewk6d`	$Z \rightarrow ee$	`5.3.3_ewk`
`wewk6m`	$W \rightarrow \mu\nu$	`5.3.3_ewk`
`zewk6m`	$Z \rightarrow \mu\mu$	`5.3.3_ewk`
`wewk9t`	$W \rightarrow \tau\nu$	`5.3.3_ewk`
`zewk8t`	$Z \rightarrow \tau\tau$	`5.3.3_ewk`
`wtop1w`	WW	`5.3.1`
`wtop1z`	WZ	`5.3.1`
`ztopcz`	ZZ	`5.3.1`

Table 4.2. Monte Carlo samples used in the analysis.

The MC samples used here are given in Table 4.2. Both the $Z \rightarrow ee$ and $Z \rightarrow \mu\mu$ samples were generated with the mass of the Z/γ^* greater than 20 GeV/c^2 and a cross section of 355 pb. (The high cross section comes from the low mass Drell-Yan events.)

The samples contain run-dependent information, to model the changes in the luminosity over time. Events occurring in the runs listed in Table 4.1 in the MC were rejected. They were found to have bad generated vertices, due to a misunderstanding about how to use the beam line information to generate the MC vertex position. The luminosity for these excluded runs corresponds to about 9 pb^{-1}, or approximately 2.7% of the Monte Carlo samples. The events in data for these run numbers were not affected, and therefore not rejected from the data sample.

CHAPTER 5

Strategy of this Measurement

$$\mathsf{R} = \frac{\sigma(p\overline{p} \to W) \times Br(W \to \ell\nu)}{\sigma(p\overline{p} \to Z) \times Br(Z \to \ell^+\ell^-)} \tag{5.1}$$

The CDF Collaboration has recently published a measurement of R [8], with a precision of 2%. With an integrated luminosity of only $\mathcal{L} = 72 \pm 4.3$ pb^{-1}, the result was nearly systematics limited. To achieve greater precision, a new approach is needed. This new approach minimizes the major systematics of the previous measurement at the cost of statistical power. The final CDF Run II dataset will be 4-8 fb^{-1}, so the aim of the new method is to take advantage of all the W's and Z's that can be found there.

In this chapter, a summary of the previous measurement is given, followed by a description of the new method.

5.1 The Counting Method

In the previous CDF analysis [8], the products of the cross sections and branching ratios for W's and Z's are computed first, then the ratio is taken to determine R. This is called the "counting method" to distinguish it from the new "shape method," described later in Section 5.2.

In the counting method, the numbers of expected W's and Z's are calculated as follows:

$$\sigma(p\overline{p} \to W) \times Br(W \to \ell\nu) = \frac{N_W^{\mathsf{obs}} - N_W^{\mathsf{bck}}}{A_W \cdot \epsilon_W \cdot \int \mathcal{L}dt} \tag{5.2}$$

$$\sigma(p\overline{p} \to Z) \times Br(Z \to \ell^+\ell^-) = \frac{N_Z^{\mathsf{obs}} - N_Z^{\mathsf{bck}}}{A_Z \cdot \epsilon_Z \cdot \int \mathcal{L}dt} \tag{5.3}$$

The N_i^{obs} is the number of signal events observed for boson i, and N_i^{bck} is the number of background events expected. The acceptance (A_i) is defined in Section 5.1.3, and the efficiencies (ϵ_i) are defined in Section 5.1.4. The integrated luminosity ($\int \mathcal{L}dt$) is the measure of all the data taken over time.

Once those pieces are put into place, any acceptances and efficiencies that are the same for W's and Z's can be canceled, as in Equation 5.4. The luminosities and their uncertainties also cancel. This is a major motivation for the ratio measurement. The luminosity uncertainty alone is on the order of 6%, as described in Section 2.2.4.

$$\mathsf{R} = \frac{\sigma(p\overline{p} \to W) \times Br(W \to \ell\nu)}{\sigma(p\overline{p} \to Z) \times Br(Z \to \ell^+\ell^-)} = \frac{N_W^{\mathsf{obs}} - N_W^{\mathsf{bck}}}{N_Z^{\mathsf{obs}} - N_Z^{\mathsf{bck}}} \cdot \frac{A_Z \cdot \epsilon_Z \cdot \int \mathcal{L}dt}{A_W \cdot \epsilon_W \cdot \int \mathcal{L}dt} \tag{5.4}$$

5.1.1 Measuring the signal (N^{obs})

To assemble the W sample the "missing energy" in an event is used.

Missing transverse energy, abbreviated $\not\!\!E_T$, is a useful quantity for studying events in which a particle escapes detection. Although the momenta of the particles that collided are unknown (even the kinds of particles that collided are unknown for a given collision), there should be no net momentum in the transverse plane.

The transverse plane is the $r - \phi$ plane, perpendicular to the beam, where $r = \sqrt{x^2 + y^2}$. The variables x, y and ϕ are defined in Figure 2.13. Tracks of particles can be projected onto this plane, so that their transverse momentum ($\vec{p_T}$) is defined $\vec{p} \cdot \sin\theta$. The angle θ is the polar angle, also shown in Figure 2.13. Since the beams collide in the z direction, the vector sum of all the p_T in an event should be zero.

Unfortunately, the tracking chambers can only measure the momentum of *charged* particles, while neutral particles leave no trace of their momentum.

Almost all particles leave energy in the calorimeter. The transverse energy is defined $E_T = \sqrt{m^2 + p_T^2}$. The mass of most particles at CDF energies is negligible: an electron used in this analysis has a mass of 0.5 MeV and a p_T of 30 GeV. Therefore, the mass term is very small, and the E_T should approximately equal the p_T. Using all of the calorimeter information, treating the energy in the transverse plane as a vector, the magnitude and direction of the missing transverse energy can be calculated:

$$\vec{E}_T + \vec{\not\!\!E}_T = 0, \quad \vec{\not\!\!E}_T = -\vec{E}_T \tag{5.5}$$

If only one particle escapes, the missing energy is the energy of that particle. If more than one particle goes undetected, the $\not\!\!E_T$ is the vector sum of the two particle's E_T.

A $W \to \ell\nu$ event should have a high-quality lepton and a large amount of $\not\!\!E_T$, carried away by the single neutrino.

For $Z \to \ell^+\ell^-$ candidates, two leptons must be found in the event. One of the leptons must pass a tight set of cuts, while the second lepton is subjected to a looser set of cuts. Requiring a second lepton (of the same type) helps reduce backgrounds. For example, a W event should not have a second charged lepton in it, so no W candidates should be in the Z sample. The invariant mass of the two leptons should be near the Z mass (Figure 5.1), and the two leptons are required to have opposite charges.

5.1.2 Backgrounds for W/Z (N^{bck})

The major backgrounds for this measurement are multi-jet events, *e.g.* $b\bar{b}$ events. Jets can contain leptons, or hadrons from these processes may be misidentified as leptons. The processes $W \to \tau\nu$ and $Z \to \tau\tau$ are also irreducible backgrounds, due to τ decays to electrons and muons. Estimates of these backgrounds can be determined

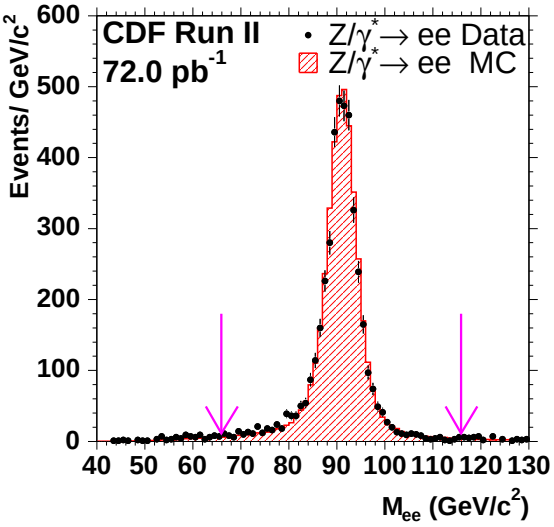

Figure 5.1. The invariant mass distribution for Z events at CDF shows excellent agreement between the data (points) and the simulation. The shaded area indicates the prediction from Pythia 6.203 Monte Carlo with simulation of the CDF detector based on the GEANT package. The area in between the two arrows contains the events used in the analysis [8].

using orthogonal datasets and simulation.

5.1.3 Acceptances (A_W and A_Z)

Unfortunately, it is not possible to measure all of the W's and Z's produced by the $p\bar{p}$ collisions. Counting the number of detected events (and subtracting the number of estimated background events) provides only a fraction of all the signal events that occurred.

The acceptance is the correction applied to compensate for the part of the solid angle not covered by the detector and the kinematic cuts used to find the leptons and $\not\!\!E_T$. The detector does not provide full coverage, so events are lost when the leptons from the W and Z are outside of the instrumented area. There are also cuts on the momenta of the leptons, and other kinematic quantities, to reject backgrounds in the low momentum region for both samples. The full description of all the cuts and acceptances for this counting method can be found in the CDF PRD [18]. Acceptances for both W's and Z's are determined from simulated data.

	Acceptance
$A_{Z\to ee}$	0.3182 ± 0.0041
$A_{W\to e\nu}$	0.2397 ± 0.0039
$A_{Z\to \mu\mu}$	0.1392 ± 0.0030
$A_{W\to \mu\nu}$	0.1970 ± 0.0027

Table 5.1. These are acceptances for the four processes considered in the 72 pb^{-1} R analysis at CDF [8], using the counting method. Uncertainties are statistical only.

The systematic uncertainty on the acceptances is one of the largest systematic uncertainties for the counting method measurement. The uncertainty comes from the Parton Distribution Functions (PDF's), which are discussed in Section 3.2.2. The acceptances depend strongly on the rapidity distribution of the bosons; higher rapidity particles are less likely to have decay products in the central, instrumented regions of the detector. The PDF's chosen have a significant effect on the shape of the $d\sigma/dy$ distribution, and therefore, the acceptance.

The rapidity is defined

$$y = \frac{1}{2}\ln\left(\frac{E+p_z}{E-p_z}\right). \tag{5.6}$$

It is related to the PDF's through x_i, the fraction of the proton's momentum that a quark or gluon carries.

$$x_{1,2} = \frac{m}{\sqrt{s}}e^{\pm y} \tag{5.7}$$

The center-of-mass energy of the collision (s) and the invariant mass of the final state particles also play a role in the the momentum fraction.

The PDF's that are available are calculated by two different groups: CTEQ [27] and MRST [29]. Comparing the cross sections calculated with different PDF's gives 1-2% uncertainties on the acceptances for the counting method.

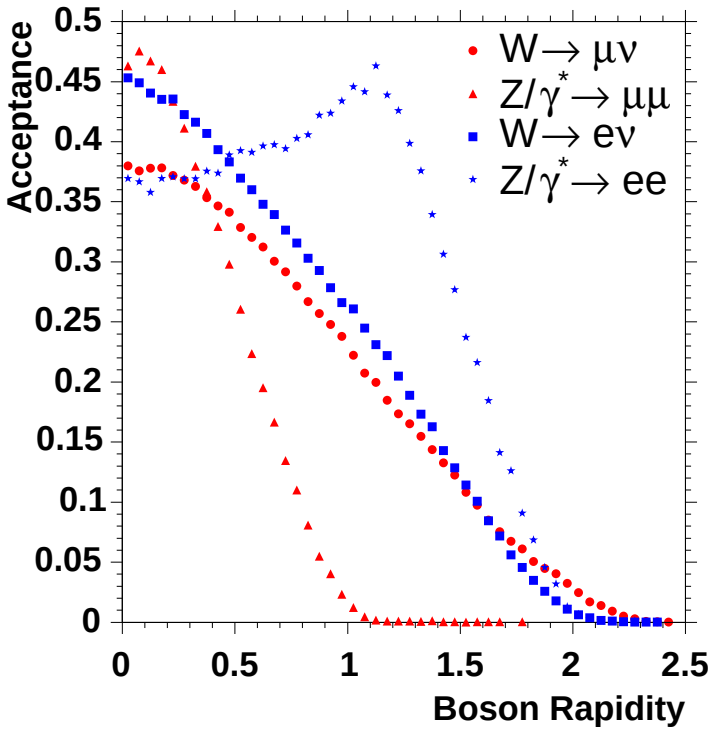

Figure 5.2. The acceptance as a function of boson rapidity is quite different for W's and Z's, for the counting method. For most of the channels, the acceptance falls off as the rapidity increases. The distribution for the $Z \rightarrow ee$ channel has two sources: events with both electrons found in the central calorimeter, and events with a central electron and a plug calorimeter electron.

5.1.4 Efficiencies (ϵ_i)

The efficiency terms describe detector and software inefficiencies that are not included in the acceptances. Examples include the efficiency of the track reconstruction for the electron or muon, the efficiency of the lepton identification cuts, and the efficiency of the triggers.

The efficiencies are studied in data, rather than in simulation. The order of determining the efficiencies is fixed, to take correlations between the different cuts into account. To obtain the total efficiency, ϵ_{tot}, all the ϵ_i are multiplied.

$$\epsilon_{\mathsf{tot}} = \prod_i \epsilon_i$$

Different total efficiencies are obtained for W's and Z's, because of the different requirements: W events have one lepton, while there are two leptons for Z's. There are also different efficiencies for the central electrons and further forward electrons, because of two different calorimeter systems. Several classes of muons are considered separately as well.

For example, for Z events with two central electrons, Equation 5.8 applies. The terms are defined in Table 5.1.4.

$$\epsilon_{\mathsf{tot}}^{\mathsf{CC}} = \epsilon_{\mathsf{vtx}} \cdot \epsilon_{\mathsf{trk}}^2 \cdot \epsilon_{\mathsf{rec}}^2 \cdot \epsilon_{\mathsf{lid}}^2 \cdot [\epsilon_{\mathsf{tid}} \cdot (2 - \epsilon_{\mathsf{tid}})] \cdot [\epsilon_{\mathsf{trg}} \cdot (2 - \epsilon_{\mathsf{trg}})] \tag{5.8}$$

The final terms result from a requirement that only one of two electrons be triggered on, and only one of two must pass more stringent lepton identification cuts. The total efficiency for a W event with one electron is shown for comparison:

$$\epsilon_{\mathsf{tot}}^{W} = \epsilon_{\mathsf{vtx}} \cdot \epsilon_{\mathsf{trk}} \cdot \epsilon_{\mathsf{rec}} \cdot \epsilon_{\mathsf{id}} \cdot \epsilon_{\mathsf{iso}} \cdot \epsilon_{\mathsf{trg}} \tag{5.9}$$

When calculating R, many of the efficiencies will cancel in the ratio, but not all.

$\epsilon_{\mathsf{tot}}^{\mathsf{CC}}$	Total efficiency for Central-Central Z events
$\epsilon_{\mathsf{tot}}^{W}$	Total efficiency for W events
ϵ_{vtx}	Vertex within 60 cm of the origin
ϵ_{trk}	Track reconstruction
ϵ_{rec}	Lepton reconstruction (matching track to energy cluster)
ϵ_{id}	Electron ID cuts for W events
ϵ_{lid}	Loose electron cuts for Z's
ϵ_{tid}	Tight electron cuts for Z's
ϵ_{trg}	Trigger efficiency
ϵ_{iso}	Electron isolation cut

Table 5.2. These efficiencies are taken from the counting method CDF PRD [18].

5.1.5 Statistical and Systematic Errors

After calculating the numerator and denominator, and carefully canceling those acceptances and efficiencies that are common to the two measurements, R is determined.

The most recent measurement for this method uses 193 pb^{-1} of data [38], with central muons only:

$$R_{\mu} = 11.02 \pm 0.14(stat) \pm 0.18(syst).$$

This can be compared with the CDF Run II measurement with 72 pb^{-1}, combining electrons and muons

$$R = 10.92 \pm 0.15(stat) \pm 0.14(syst).$$

All of the systematic uncertainties for this method are given in Table 5.3.

The Standard Model predicts

$$R = 10.69 \pm 0.013[38]$$

with the SM uncertainties coming from the PDF's, next-to-next-to-leading-order splitting functions, and electroweak parameters.

5.2 The Shape Method

The new analysis treats the selection of W and Z events in parallel, forming one dataset that contains both W's and Z's. The value of R is inferred on a statistical basis by looking at an appropriate kinematic quantity, rather than separating W events from Z events and counting them.

The key to lowering systematics is to make the selection of W's and Z's the same, so more uncertainties cancel in the ratio.

5.2.1 Event Selection

The goal of the event selection is to keep as many W and Z events, while eliminating background events. The event selection has two simple requirements.

	Electron	Muon
Central Value ± syst	10.82 ± 0.16	11.12 ± 0.18
Acceptances		
Simulation Statistics	0.0294	0.0480
Boson p_T Model	0.0019	0.0044
PDF Model	0.0704	0.0851
p_T Scale and Resolution	0.0012	0.0170
E_T Scale and Resolution	0.0185	0.0000
Material Model	0.0319	0.0000
Recoil Energy Model	0.0267	0.0384
Efficiencies		
Uncorrelated	0.1203	0.1015
Track Reconstruction	0.0170	0.0445
Backgrounds		
Hadronic	0.0435	0.0397
Uncorrelated Electroweak	0.0089	0.0112
Correlated Electroweak	0.0042	0.0290
Cosmic Ray	0.0000	0.0702

Table 5.3. The largest uncertainties for both channels come from efficiency terms that do not cancel, due to different requirements for the W's and Z's. The PDF Model, discussed in Section 5.1.3, is the next largest contributor, followed by uncertainties on the backgrounds. These are taken from the CDF 72 pb^{-1} PRD [18].

Identifying W's and Z's

The decays of the W and Z are identified in this analysis by a single high-energy lepton. Any event with a lepton that passes tight cuts is in the initial sample. There is no cut on $\not\!\!E_T$, and there is no requirement for a second lepton for Z events.

Without a second lepton in the Z events, the efficiencies (the largest systematic) cancel completely in the ratio. The material uncertainty also cancels.

By creating a sample with the same cuts for W's and Z's, the acceptances for W's and Z's are virtually identical. Any uncertainty from the PDF's comes from genuine differences in the cross sections (W's couple to $u\bar{d}$ while Z's couple to $u\bar{u}$ and $d\bar{d}$).

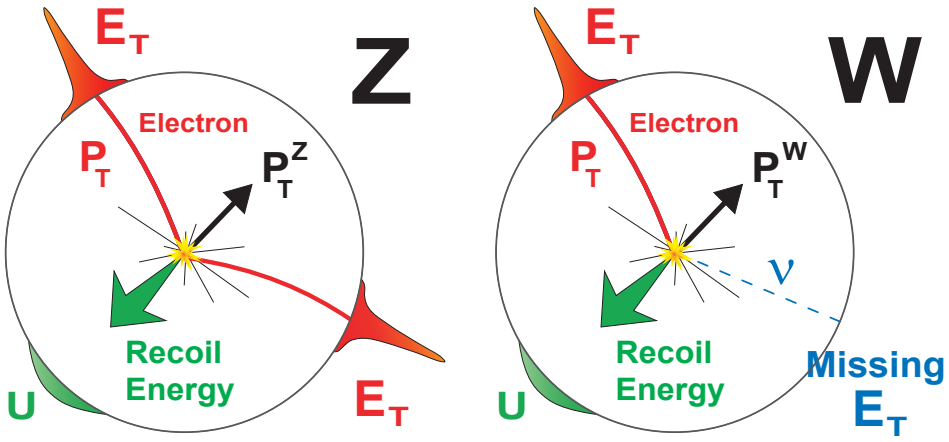

Figure 5.3. To conserve energy in the transverse plane, there must be some recoil energy to balance any transverse momentum carried by the W and Z.

Removing Background

Not all of the events with a high-energy lepton are W and Z decays. It is important to eliminate background events, and estimate the fraction of background that remains.

The largest background is made up of multi-jet events. These events can come from processes with much higher rates than W and Z production, such as $b\bar{b}$ production. Because of the proliferation of events with two or more jets, even a very small acceptance of these events can lead to a large source of background. They are often called "QCD background" events because the strong force, Quantum Chromodynamics, can be involved in both their production and their decay and hadronization into jets of particles. One way that these backgrounds are removed is by requiring that the leptons chosen for W and Z analyses be well-isolated in the detector. This cut rejects events with particles inside jets that are misidentified as leptons.

Examining the recoil energy (Figure 5.3) provides another handle on the QCD background events. Recoil energy is defined by summing all of the calorimeter energy in the event, and subtracting the energy that is associated with the leptons. To remove the energy associated with the leptons, they must be at least loosely identified. This process is described in more detail in Section 6.3. Other possible backgrounds,

diboson production and $t\bar{t}$ final states, are negligible due to their low cross sections and the recoil cut.

All of these backgrounds are described in Chapter 7.

5.2.2 The Fit

Once the sample is selected, a maximum likelihood fit is used to determine the relative fraction of W's and Z's. The fit requires templates for each of the signals and backgrounds, which are fit to the data spectrum. The templates used for the W and Z are taken from simulation, while the background fraction and background template for the multi-jets are obtained from data.

For the electron channel presented here, the fit is a binned one-dimensional fit, performed on the $\not\!\!E_T$ distribution (Figure 5.4). This is very discriminating, since W events naturally have a large $\not\!\!E_T$ from the neutrino, while Z events should have almost no $\not\!\!E_T$. There is a small subset of the Z events which have a large $\not\!\!E_T$ due to detector effects, which will be discussed later.

The measurement in the muon channel is still under investigation. Both the p_T of the muon and the $\not\!\!E_T$ of the event are candidates for the kinematic distribution to be fit. The muon channel is discussed in the Conclusions (Section 11.1), but not in the rest of this thesis.

The process $W \to \tau\nu$ is directly related to $W \to e\nu$, and the same can be said of $Z \to \tau\tau$ and $Z \to ee$. Therefore, the templates for these processes can be combined with the signal templates directly, assuming lepton universality. Consequently, there are only three templates to be fit:

1. $W \to e\nu$, combined with $W \to \tau\nu$
2. $Z \to ee$, combined with $Z \to \tau\tau$
3. multi-jet background from the data

Two fits are performed to extract R. Events with positive and negative leptons

are fit separately, to deal with events in which two (oppositely-charged) leptons pass all of the cuts, including the trigger requirement. The two fits can be combined at the end, taking the correlation into account.

In the following chapters, the event selection and fitting procedure for the electron channel of this new shape method are described in more detail. Then, the value of R is obtained, and the systematics uncertainties of this new method are analyzed.

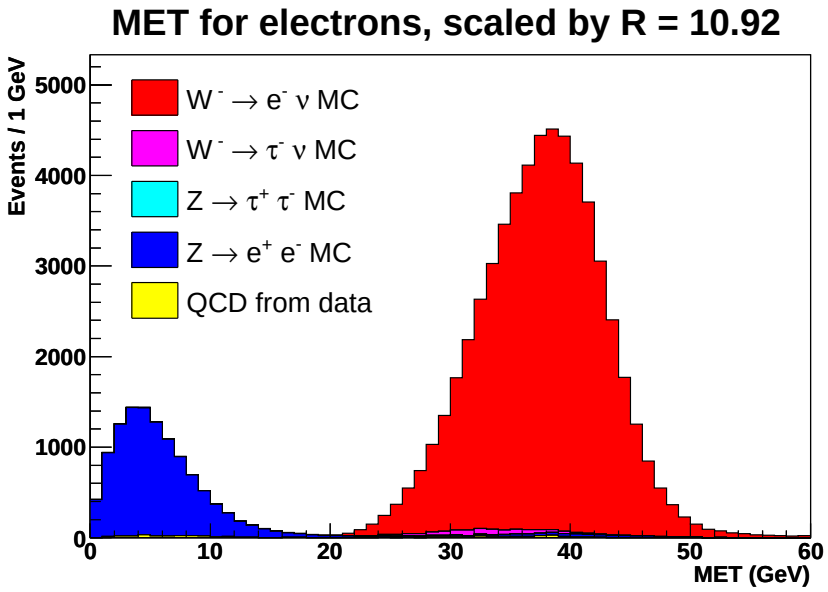

Figure 5.4. Missing energy templates for W's and Z's have very different shapes.

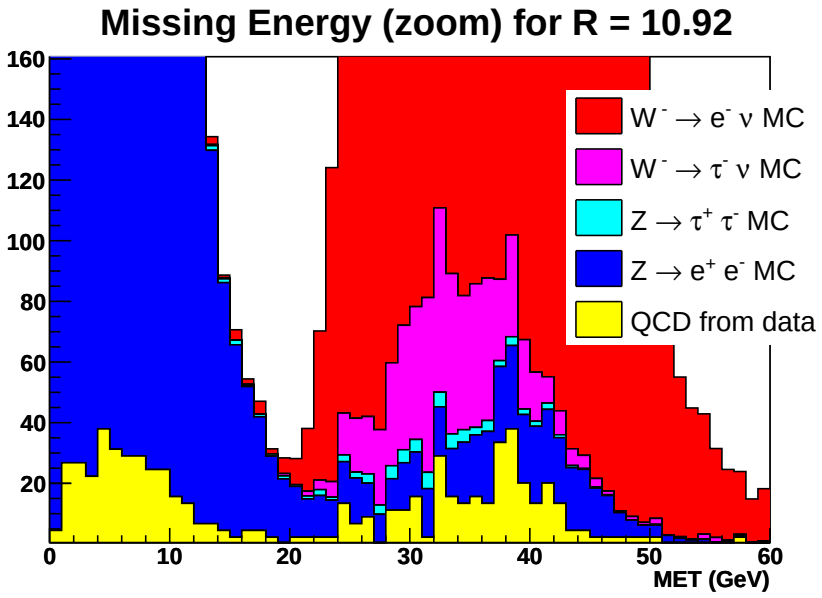

Figure 5.5. This is a close-up view of the missing energy templates in Figure 5.4.

CHAPTER 6

Event Selection

The goal of the event selection is to isolate events with W's and Z's, while restricting the amount of background in the sample. Care is also taken to make similar requirements for W and Z events, in order to minimize systematics for the R measurement. This is accomplished by requiring only one high-energy electron[1] in the event and by cutting on the recoil energy.

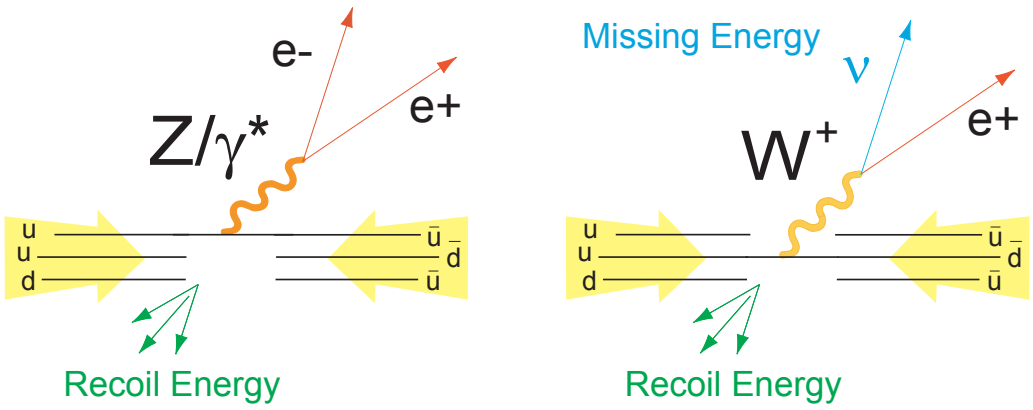

Figure 6.1. Protons and antiprotons collide to form W and Z bosons. The bosons can decay leptonically to electrons and electron neutrinos. Recoil energy in the event balances any transverse momentum that the boson carries.

6.1 Datasets

This analysis is performed on the CDF data, using the tools and parameters listed in Table 6.1.

The first cuts are made at the event level. Portions of the data in which all the

[1]Throughout the following chapters, "electron" is used as a shorthand for "electron or positron."

CDF Data Parameters
Dataset: bhel0d
Data Format: TopNtuple
Software version: 5.3.3_nt5
Good Run List: Version 7, 1001
Trigger: ELECTRON_CENTRAL_18

Table 6.1. These parameters describe the tools and software versions used for the analysis.

key systems were functioning well are included on a "good run list." Only events that occurred in runs on this list are considered.

For each event, the central electron trigger must have fired. This trigger gives some basic indication that an electron was in the final state, and it caused the event to be recorded. This trigger selects events with a cluster of energy in the central calorimeter with an E_T of 18 GeV or greater. A track from the central tracking chamber of 9 GeV or greater must be matched to the cluster. The trigger system is described in Section 2.2.5.

Events are removed from consideration if any electron candidate in the event is flagged as a conversion electron. A conversion is an electron from a photon that interacted with material in the detector to produce an electron-positron pair. Since the goal is to find electrons from W's and Z's, these conversions should be removed. An exception is made for trident events, where a photon is radiated from an electron, and that photon converts again into an electron and positron pair. This process is usually narrow enough in $\eta - \phi$ space to be captured in a single tower of the calorimeter, so most of the energy from the original electron should still be measurable.

6.2 Electron Selection

The CDF calorimeter (Section 2.2.2) has two major sections: the central section and the high-η plug calorimeters. The two systems have different parameters and very different tracking, so electrons at CDF are divided into two groups, based on the calorimeter in which they are detected. In this analysis, only central electrons are

used. Plug electrons may be used in a later version of the analysis, but the higher background rate for plug electrons would be a concern. The central electron cuts are described here, and in Table 6.2. Much more detailed explanations of the electron identification process can be found elsewhere [28].

To find central electrons, the first requirements define the space of the detector that is well-instrumented and efficient at measuring the electron variables.[2]

The next step is to identify candidate electron clusters in the central calorimeter. An energy cluster is made from an electromagnetic tower above some threshold (the seed tower) and at most one additional tower that is adjacent in η and within the same ϕ wedge. For this analysis, requiring electrons to have a calorimeter energy of $E_T > 30$ GeV greatly reduces background.

At these energies, the mass of the electron is negligible; the energy should be close to the momentum. A cut of $E/P < 2$, where E is the EM cluster transverse energy and P is the p_T of the track, helps remove events with poorly measured, lower energy tracks.

If the object is a true electron, it will deposit most of its energy in the EM calorimeter. Therefore, the energy in the hadronic calorimeter will be much smaller than that in the EM. Requiring $E_{HAD}/E_{EM} < 0.055 + 0.00045 * E$ (where E is the total energy) helps remove objects which are actually inside hadronic jets.

Another variable called the lateral shower sharing (L_{shr}) discriminates between electrons and photons inside jets. It measures the amounts of energy in the seed and adjacent towers, and compares the observed energies to those from electron test beam data [28].

[2]Areas that are excluded from consideration are the following: the region of the detector where the two halves of the central calorimeter meet ($|z_{\rm CES}| < 9$ cm), the outer half of the most forward CEM towers ($|z_{\rm CES}| > 230$ cm) where there is substantial electron shower leakage into the hadronic part of the calorimeter, and the uninstrumented region used for cryogenic connections to the magnet ($0.77 < \eta < 1.0$, $75^\circ < \phi < 90^\circ$, and $|z_{\rm CES}| > 193$ cm). The edges of the CES detector are also excluded; the cluster in the CES must lie within 21 cm of the tower center in the $r - \phi$ plane.

For the final calorimeter cut, electrons from W and Z events should be isolated in the calorimeter; they should not have many other particles in nearby towers, as a jet would. The "isolation" is defined as the ratio of energy in a cone of $\Delta R = \sqrt{\Delta\eta^2 + \Delta\phi^2}$ minus the energy of the cluster itself, divided by the energy of the electron cluster. Isolation must be < 0.1.

Next, the electron-candidate must have a good quality COT track associated with it. The origin of the electron track must be within 60 cm of the origin of the detector in the $r - z$ plane. The track cuts ensure that the track is well-measured: there must be at least 5/12 hits in each superlayer of the COT, in at least 2/4 of the axial superlayers and at least 2/4 of the stereo superlayers. High-energy electrons from W and Z decays should have a high-momentum track; a p_T of at least 10 GeV is required. The electron charge is determined from the curvature of the track.

The track must match the high-energy cluster in the calorimeter. The shower-maximum (CES) detectors placed inside the central electromagnetic calorimeter measure the shower profile and help identify the location of the incident particle. The distance in the $r - z$ plane is calculated between the extrapolated COT track and the best matching CES cluster. This distance must be less than 3 cm. The distance between the track and the CES cluster in the $r - \phi$ plane (Δx) is multiplied by the charge of the object, to require that $q \cdot \Delta x$ is between -3.0 and 1.5 cm. The asymmetric cut accounts for possible bremsstrahlung radiation. As a final check on the CES cluster, the $r - z$ view of the shower profile from the CES is compared to an electron shower profile from test-beam data. A chi-squared comparison is performed and a cut is made, keeping electrons with $\chi^2_{\text{strip}} < 10$.

6.2.1 Trigger Requirement for Electrons

To treat W's and Z's in the same way, the two samples of events with positrons and events with electrons are kept separate. This means that every requirement has

Quantity	TopNTuple Variable	Cut
Conversion		$\neq 1$[3]
Region		$= 0$
Fiducial		$= 1$
Transverse Energy		≥ 30
E/P	EP	≥ 2.0 (if TrkPt > 50)
Had/Em Energy	Hadem	$<$ (0.055 + 0.00045 * En)
Lateral Shower Profile	LshrTrk	< 0.2
Isolation	Isol	< 0.1
Track Origin	|TrkZ0|	< 60
Number of Axial SL	TrkAxSeg	≥ 3
Number of Stereo SL	TrkStSeg	≥ 2
Track Momentum	TrkPt	≥ 10
CES-COT ΔZ	|DeltaZ|	< 3
CES ΔX	DeltaX * Charge	$>$ -3
CES ΔX	DeltaX * Charge	< 1.5
Chi-squared for CES	StripChi2	≤ 10

Table 6.2. Tight Central Electron cuts, described in Section 6.2.

to be identical for the e^+ and e^-. In many analyses, it is enough to know that the trigger has fired for the entire event. For this analysis, to treat electrons and positrons identically, each one is required to be a lepton that fired the trigger. Since one of the trigger subsystems (the XFT) has an efficiency of about 97 ± 1 %, there is a non-negligible probability that the event was triggered not by a given lepton, but by the other one in a Z event. According to MC studies, there is a second track with $p_T > 10$ GeV about 52% of the time.

Unfortunately, a portion of the data was missing the trigger information needed to determine which electrons were firing the trigger.[4] This reduces the data available for analysis from 374 to 307 pb^{-1}.

[4]The XFLD banks were dropped for runs 164452-168567, TL2D banks were unavailable in the NTuple.

6.3 The Recoil Energy

The sample of events with one tight lepton contains many W's and Z's, but it also contains background. In most of the background events, the lepton selected is not from a W or Z but from a jet. It may be a real lepton from a semi-leptonic b decay, or it may be another particle like a pion which has passed the electron identification. A W or Z that decays hadronically is included in this background, since only the leptonic decays should be counted as signal. The recoil energy cut excludes most of this background, as shown in Figure 6.2.

The recoil energy (U) is the transverse energy of the recoiling particles produced along with a W or Z boson. In terms of the E_T of the leptonic decay products, $E_T(\ell_1)$ and $E_T(\ell_2)$:

$$\overrightarrow{U} = -\left[\overrightarrow{E_T}(\ell_1) + \overrightarrow{E_T}(\ell_2)\right] \tag{6.1}$$

From a detector point of view, the recoil energy may be defined as the transverse energy in the calorimeter that is not associated with the leptons from the boson decay.

- For W events:

$$\overrightarrow{U} = -\left[\overrightarrow{\not\!\!E_T} - \overrightarrow{E_T}(\ell)\right] \tag{6.2}$$

- For Z events:

$$\overrightarrow{U} = -\left[\overrightarrow{\not\!\!E_T} - \overrightarrow{E_T}(Z)\right] \tag{6.3}$$

For W events, removing the tight electron's energy from the vector-opposite of the $\not\!\!E_T$ yields the recoil energy. Figure 5.3 illustrates the recoil in the transverse plane for W's and Z's.

Z events, however, have a second electron that often deposits a large amount of energy in the calorimeter. If that second leg is not found as a tight, central, isolated electron, and the recoil is calculated by removing only the tight leg, the recoil energy for those events will be centered around the E_T of the second leg.

Consequently, the energy of the highest-E_T second object, if one is found in the

event, is also removed. To select the second object, the following cuts are applied to the collection of energy clusters with $E_T > 15$ GeV in the calorimeter. For objects in the central region, a track matched to the cluster and the Had/Em cut in Table 6.2 are required. In the plug region, the same Had/Em cut applies, but no make a track requirement. At most, one other object is removed from the calorimeter energy. These requirements on the second object are much looser than the ones used in the previous analysis for selecting a second lepton in the Z events.

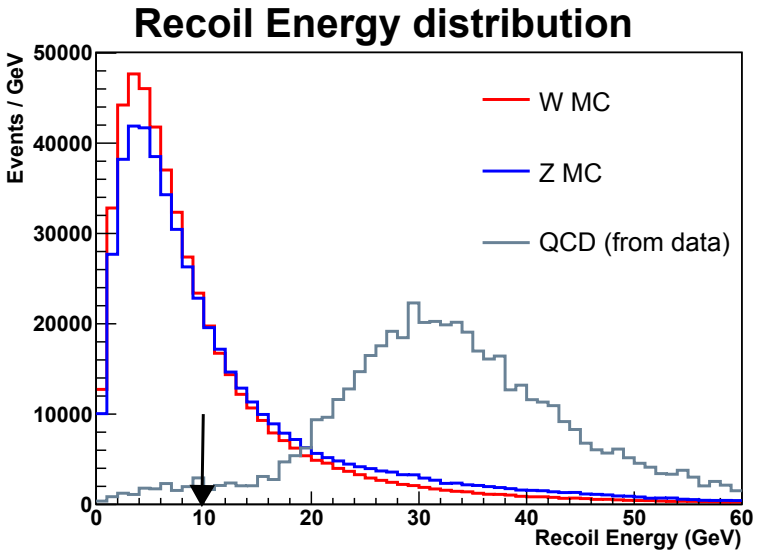

Figure 6.2. Recoil energy distribution for W and Z Monte Carlo, and the QCD background from data. (The QCD selection is described in Section 7.3.) The shapes are normalized to equal area. The events below 10 GeV are used in the analysis.

6.4 Tuning of the Recoil and $\not\!\!E_T$

The W and Z templates from the MC did not match the data very well, at first (Figure 6.4). The absolute scale of the calorimeter calibration, and its reflection in the simulation, are very important to analyses like the W mass. For this analysis, the most important thing is that the shapes of the data and MC match well, regardless of the absolute energy scale. Scale and shift corrections for the $\not\!\!E_T$ in the MC were investigated to provide a better match, and determine the systematic error associated

with the uncertainty in the energy scale.

There are two components to the $\not\!\!E_T$: the electron E_T and the hadronic recoil, so the $\not\!\!E_T$ can be written as the sum:

$$\begin{aligned} (\not\!\!E_T)_x &= -U_x - (E_T)_x \\ (\not\!\!E_T)_y &= -U_y - (E_T)_y \end{aligned} \tag{6.4}$$

where U_x and U_y are the x and y components of the hadronic recoil.

Given the cut $U < 10$ GeV, the electron E_T dominates, so the scale for the electrons is set first. This is done using the narrow peak of the Z resonance. A very small rescaling is found to be appropriate:

$$(E_T)_{\text{corr}} = \alpha \times (E_T)_{\text{raw}} \qquad \text{where} \qquad \alpha = 0.9959 \pm 0.0004 \tag{6.5}$$

and the error on α is statistical only. The χ^2 from this minimization, and a comparison of the tuned simulation to the data are shown in Figure 6.3.

After applying this small correction to tight electrons, the W and Z templates are examined. (The background template does not need to be scaled, since it comes from the data.) Two very pure samples of W's and Z's are defined to use for this purpose. Both have one tight electron, and more restrictive cuts:

- W sample: Veto the event if there is any other electromagnetic object with $E_T > 2$ GeV.
- Z sample: Demand a second tight electron, with charge opposite to the first, and the invariant mass of the two electrons within $66 < M_{ee} < 116$ GeV.

Looking at these two subsamples, the $\not\!\!E_T$ is clearly shifted (Figure 6.4).

There could be a non-zero offset for the $\not\!\!E_T$ coming from operation of the calorimeter or the underlying events. Therefore an offset is allowed, as well as a scale factor for tuning the $\not\!\!E_T$:

$$(\not\!\!E_T)_{\text{corr}} = A + B \times (\not\!\!E_T)_{\text{raw}} \tag{6.6}$$

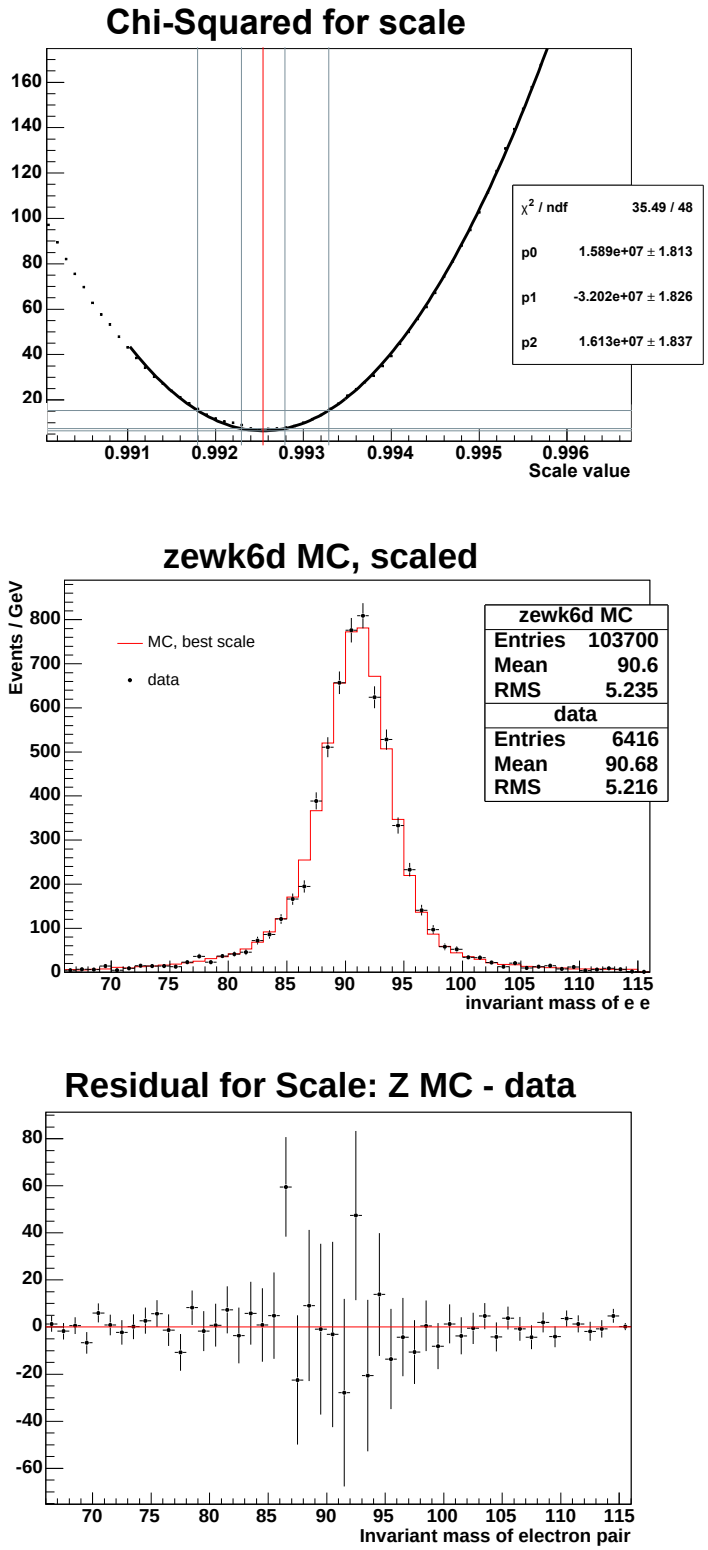

Figure 6.3. These are the results of the fit to set the E_T scale for electrons. The top plot shows the variation of χ^2 with the scale factor. The middle plot shows a comparison of the scaled simulation to the data. The bottom plot shows the residuals of the data with respect to the scaled simulation.

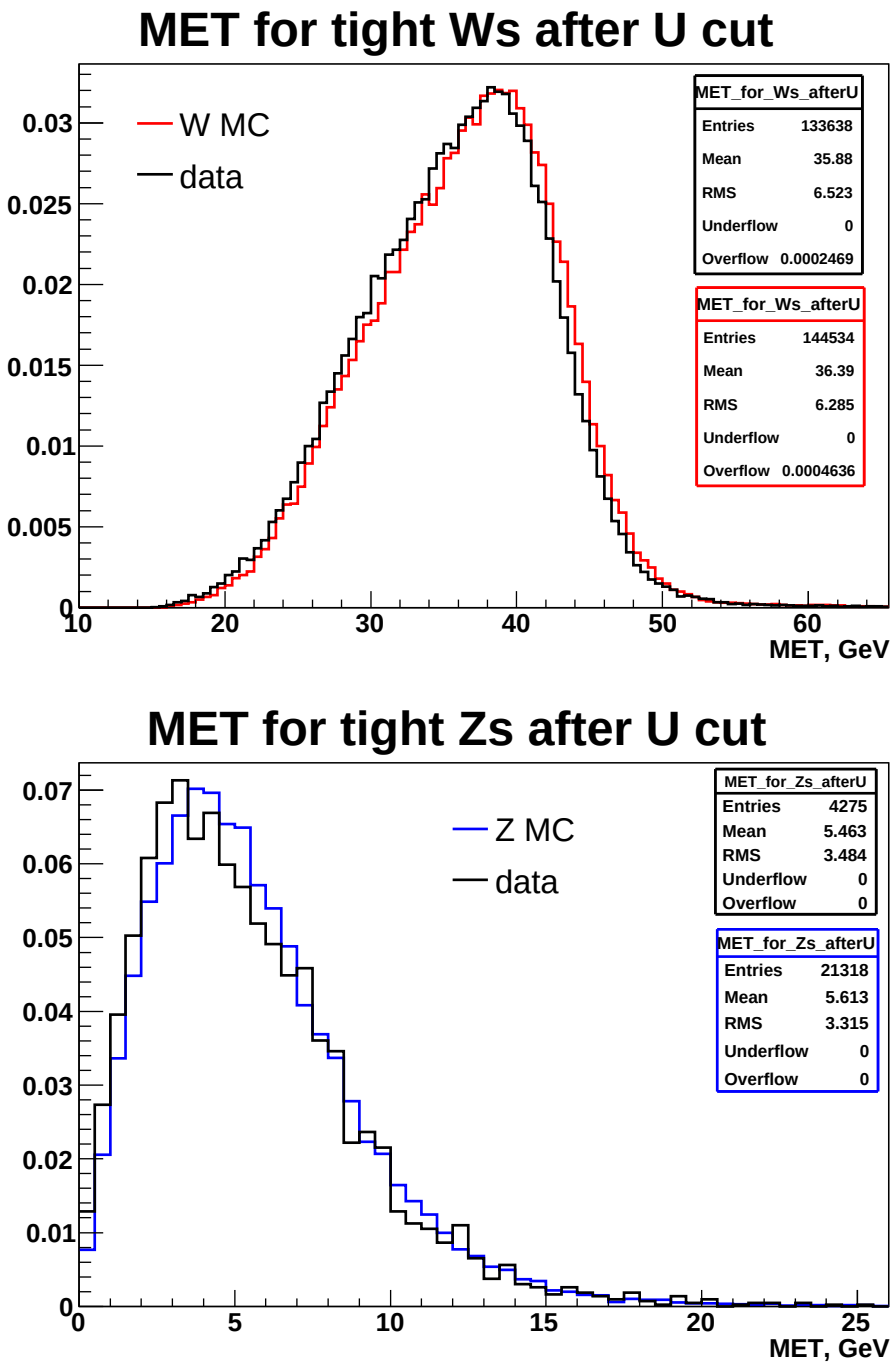

Figure 6.4. The untuned $\not\!\!E_T$ distributions show poor agreement between the MC and data.

where A and B are to be determined by a χ^2 comparison of the data histogram and the MC template. The results are:

$$A = 0.9921 \pm 0.0006 \qquad \text{and} \qquad B = -0.23 \pm 0.04 \text{ GeV}. \tag{6.7}$$

A comparison of the tuned $\not\!\!E_T$ to data is given in Figure 6.5. The tuned templates will be used for the MC in the rest of this analysis. When systematic uncertainties are evaluated, the change in Rdue to the change in the template shapes will be evaluated.

6.5 Removing Events with Muons

Decays of W's and Z's in the electron channel should not have any high-energy muons in the event. A requirement that there be no muon passing the following cuts is made. This also allows an easier combination of the electron and muon channels, since they will have no overlapping events. It also removes the (albeit low rate) background processes which might result in an electron and muon.

Muon Selection Cuts

Based on the standard CDF high-p_T muon selection cuts, a muon candidate must pass all of the cuts listed in Table 6.3. Two types of muons corresponding to different sets of muons detectors are considered, CMUP and CMX. Any event with either type of muon is rejected for this electron channel analysis.

6.6 Acceptance Calculation

Once the sample has been defined, the acceptance is calculated. For a usual counting method analysis, the acceptances relate the number of observed events and the cross sections. For a number of produced events, it shows how many should have been accepted in the area of the detector used for analysis, with the particular cuts used. For this shape analysis, the ratio of acceptances will be the important number.

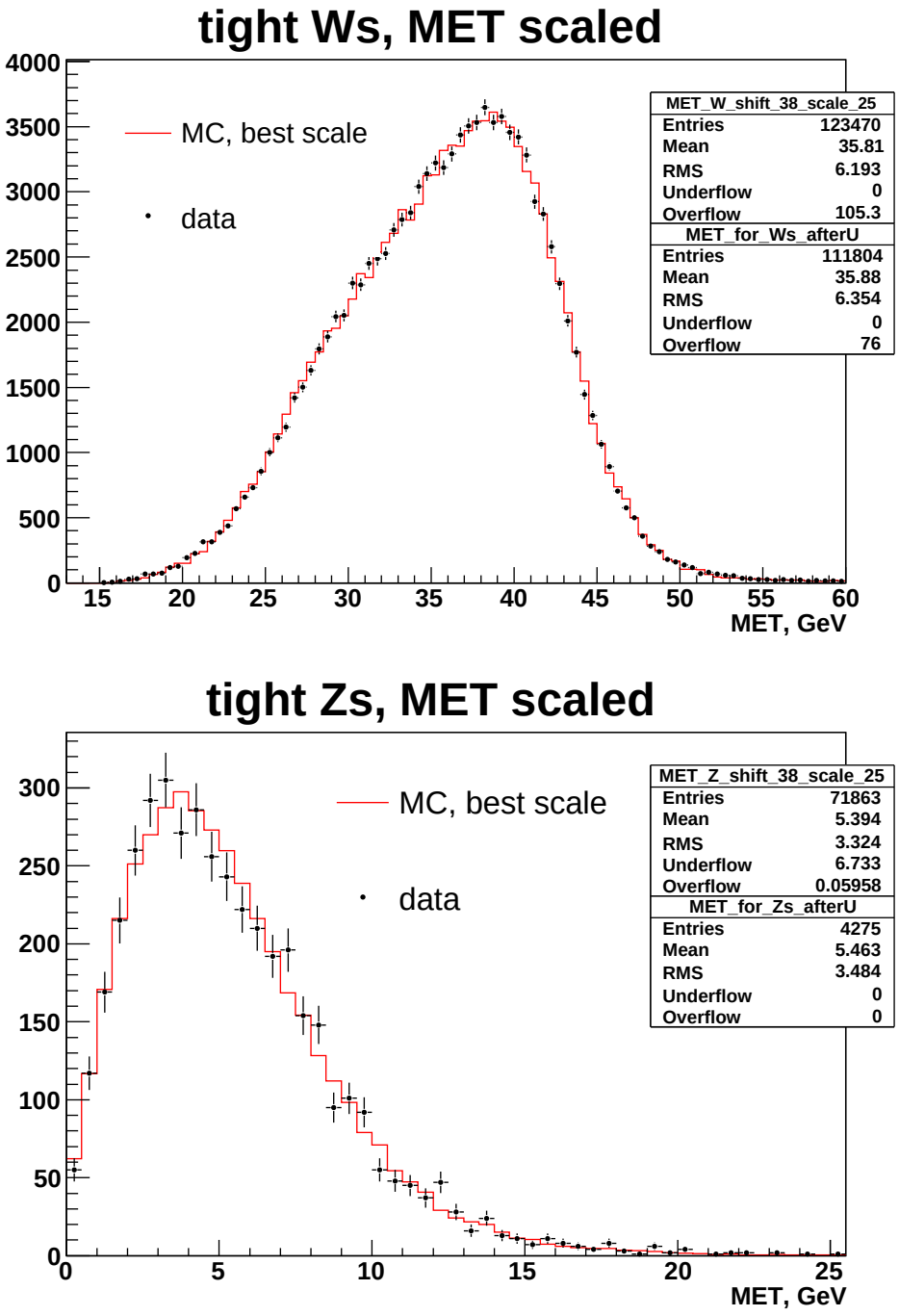

Figure 6.5. The tuned $\not\!\!E_T$ distributions match the data well.

For all muons:	Required Value
p_T	> 20 GeV
$\|z_0\|$	< 60 cm
E_{EM}	< 2 GeV
E_{HAD}	< 6 GeV
COT Axial superlayers	≥ 2
COT Stereo superlayers	≥ 2
Hits per superlayer	≥ 5
If silicon hits: $\|d_0^{(\mathrm{SVX})}\|$	< 0.02 cm
If no silicon hits: $\|d_0^{(\mathrm{COT})}\|$	< 0.15 cm
Isolation: (E_T in cone of $R = 0.4$ around muon)/p_T	< 0.1
Track-χ^2/ndf	< 3
ρ_{COT}	> 140 cm
For CMUP muons:	
$x_{\mathrm{fid}}^{\mathrm{CMU}}$	< 0 cm
$z_{\mathrm{fid}}^{\mathrm{CMU}}$	< 0 cm
$\|dx - cmu\|$	< 7 cm
$x_{\mathrm{fid}}^{\mathrm{CMP}}$	< 0 cm
$z_{\mathrm{fid}}^{\mathrm{CMP}}$	< -3 cm
$\|dx - cmp\|$	< 5 cm
`CMUP18` Trigger	Fired, matches at Level 1
For CMX muons:	
$x_{\mathrm{fid}}^{\mathrm{CMX}}$	< 0 cm
$z_{\mathrm{fid}}^{\mathrm{CMX}}$	< -3 cm
$\|dx - cmx\|$	< 6 cm
`CMX18` Trigger	Fired, matches at Level 1

Table 6.3. Tight Central Muon Cuts

channel	≥ 1 tight electron	$U < 10$ GeV	$\not\!\!E_T < 60$ GeV	net
$W \rightarrow e\nu$	0.0870	0.671	0.996	0.0581
$\gamma^*/Z \rightarrow ee$	0.1097	0.607	1.000	0.0665
$W \rightarrow \tau\nu$	0.00141	0.526	0.995	0.000735
$\gamma^*/Z \rightarrow \tau \rightarrow e$	0.00052	0.266	0.994	0.000524

Table 6.4. The acceptances for the four physics channels are given. The values for the τ-channels include the τ electronic branching ratio.

As a rough approximation, the ratio of the acceptances is expected to be 1 : 2, as there are twice as many chances to find a $Z \rightarrow ee$ event which has two charged leptons, compared to a $W \rightarrow e\nu$ event which only has one. However, the initial momentum and rapidity distributions of the W and Z bosons differ, so there may be some deviation.

The acceptance is calculated from the PYTHIA simulation:

$$A = \frac{N_{\text{acc}}}{N_{\text{lum}}} \tag{6.8}$$

N_{lum} is defined as the number of events generated in the luminous region, with the event vertex within 60 cm of the detector origin. N_{acc} is defined as the number of reconstructed events passing the selection cuts.

The acceptances in Table 6.4 for all the MC samples used in this analysis show what fraction of events are expected to fall in the coverage of the detector, passing the kinematic cuts of this analysis.

CHAPTER 7

Background Estimation

The likelihood fit to the data requires templates for each of the different physics processes. The signal templates are obtained from W and Z Standard Model PYTHIA simulations. The background contributions must also be taken into account.

Backgrounds to the shape method event selection come from the following sources: true W and Z events in which the boson decayed into a τ and a neutrino, diboson events (WW, WZ, ZZ), top quark decays, and multi-jet events (QCD). These backgrounds fall into two categories. The first category scales directly with the W and Z signal cross sections. This category includes the $W \rightarrow \tau\nu$ and $Z \rightarrow \tau\tau$ processes. Assuming that the W and Z decay into taus as often as they decay into electrons, the shape templates for these backgrounds can be added directly to the signal templates, as discussed below. The second background category does not scale directly with the signal. The contribution from these sources is calculated and fixed before performing the fit. This category includes the QCD multi-jet, top, and diboson events. Each of these backgrounds is discussed in more detail below.

7.1 Contributions from τ decays

An event with a high-energy electron and low recoil energy may be the result of decay of an electroweak boson in the τ channel. The τ can decay to an electron and neutrinos, muon and neutrinos, or to jets. If it decays into an electron and neutrinos, the event may enter our selection. The τ decays in the electron channel almost 20%

of the time:

$$Br(\tau^- \to e^- \bar{\nu}_e \nu_\tau) = 0.1784 \pm 0.0006$$

according to the Particle Data Group [39]. The τ's energy is divided amongst the three decay products, so the resulting electrons are rarely energetic enough to meet the 30 GeV energy requirement for this analysis.

The small tau contributions from $Z \to \tau\tau$ and $W \to \tau\nu$ are visible in Figure 5.5.

7.2 Contributions from Diboson Events and Top

The cross sections for diboson and $t\bar{t}$ production very small, compared to those for W's and Z's. The number of accepted events is further suppressed by the U cut, with the result that these backgrounds are negligible: for 307 pb^{-1}, only 1.3 events are expected from $t\bar{t}$, and 14 events from W^+W^-, with smaller contributions from WZ and ZZ. No correction to the templates is made for these small backgrounds.

7.3 Multi-jet (QCD) Background

The most crucial background comes from the QCD multi-jet events. This background is pernicious because it contributes preferentially to the low-$\not\!\!E_T$ region where the Z events fall. It turns out that even a small perturbation on the level of the QCD background has a non-negligible effect on R.

It is especially important that the background selection models the kinematics of our signal sample, since the QCD $\not\!\!E_T$ template is used for the fit. The counting method background estimation comes from placing an anti-cut on the isolation. Electrons inside jets should be less isolated, true, but isolation is related to the E_T of the electron. Requiring the model of the background to have an isolation greater than 0.1 would kinematically bias the sample.

Instead, in this analysis, anti-cuts are performed on variables that are not kinematic. This method was developed at CDF by Cooper & Messina [19]. The presumed

QCD events are modeled using data collected with the same electron trigger as the data. If an event has a tight electron in it, it is rejected, so the background selection and signal samples are mutually exclusive. Then, events are selected with one or more electron objects that seem like they have come from a background process.

For an object to qualify as a fake electron, every kinematic electron cut must be passed, including isolation. The selected electromagnetic objects are then required to fail at least two of the four cuts classified as "ID" cuts. All of the electron cuts are described in Table 6.2. They are subdivided into two sets of cuts:

1. Kinematic: E_T, p_T, central region, fiducial, z_0, E/P, Isolation, Had/Em
2. ID: χ^2, L$_s hr$, CES ΔX, CES ΔZ,

After selecting the sample of events with an electron object from a background process, the U distribution (Figure 7.1) of this sample is examined. There are very few events at low U, which shows the efficiency of the recoil cut. The peak of the distribution is centered around 30 GeV. This agrees with the presumption that the events are primarily dijet events. Something was identified with 30 GeV of energy as an electron, and there is 30 GeV of energy to balance it on the other side.

Next, the QCD U-template must be corrected for the contribution from W's and Z's which make it into the background sample. This correction is significant. The W and Z pieces are normalized according the luminosity of the inclusive electron sample and known cross sections ($\sigma_W = 2775$ pb and $\sigma_{DY} = 498$ pb). The method must be iterated after R is determined, so that R is not used to measure itself. The lower plot in Fig. 7.1 shows the corrected QCD $\not\!\!E_T$ distribution. The U distribution is fit in order to determine the fraction of the background in the data sample. The result is shown in Figure 7.2. Before the U cut, the QCD contribution is 0.088 ± 0.003, where the error comes from the fit. After the U cut, the remaining QCD background is $f_{\rm QCD} = 0.00698$.

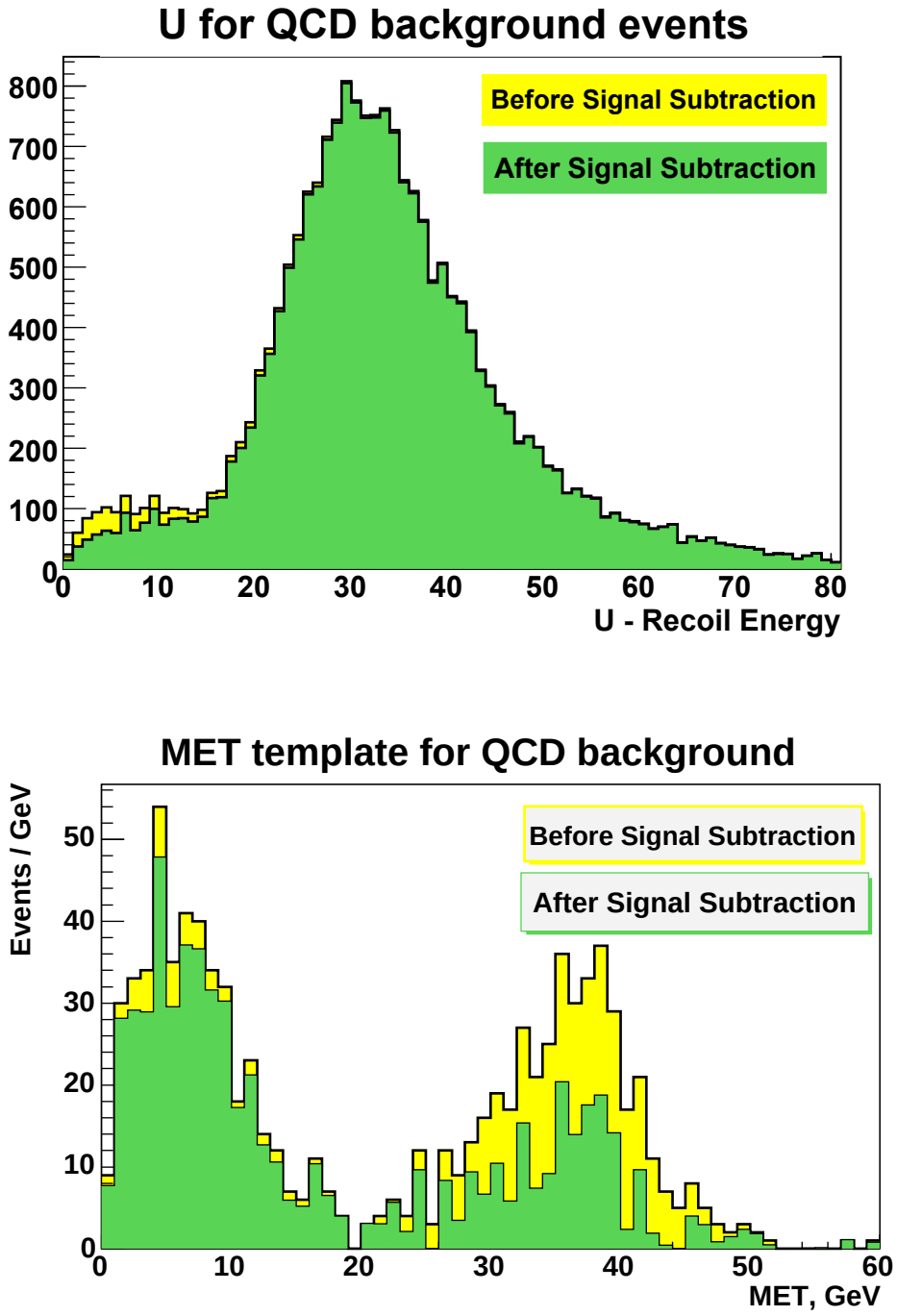

Figure 7.1. QCD U template (top), and the $\not\!\!E_T$ distribution for those events with $U < 10$ GeV (bottom).

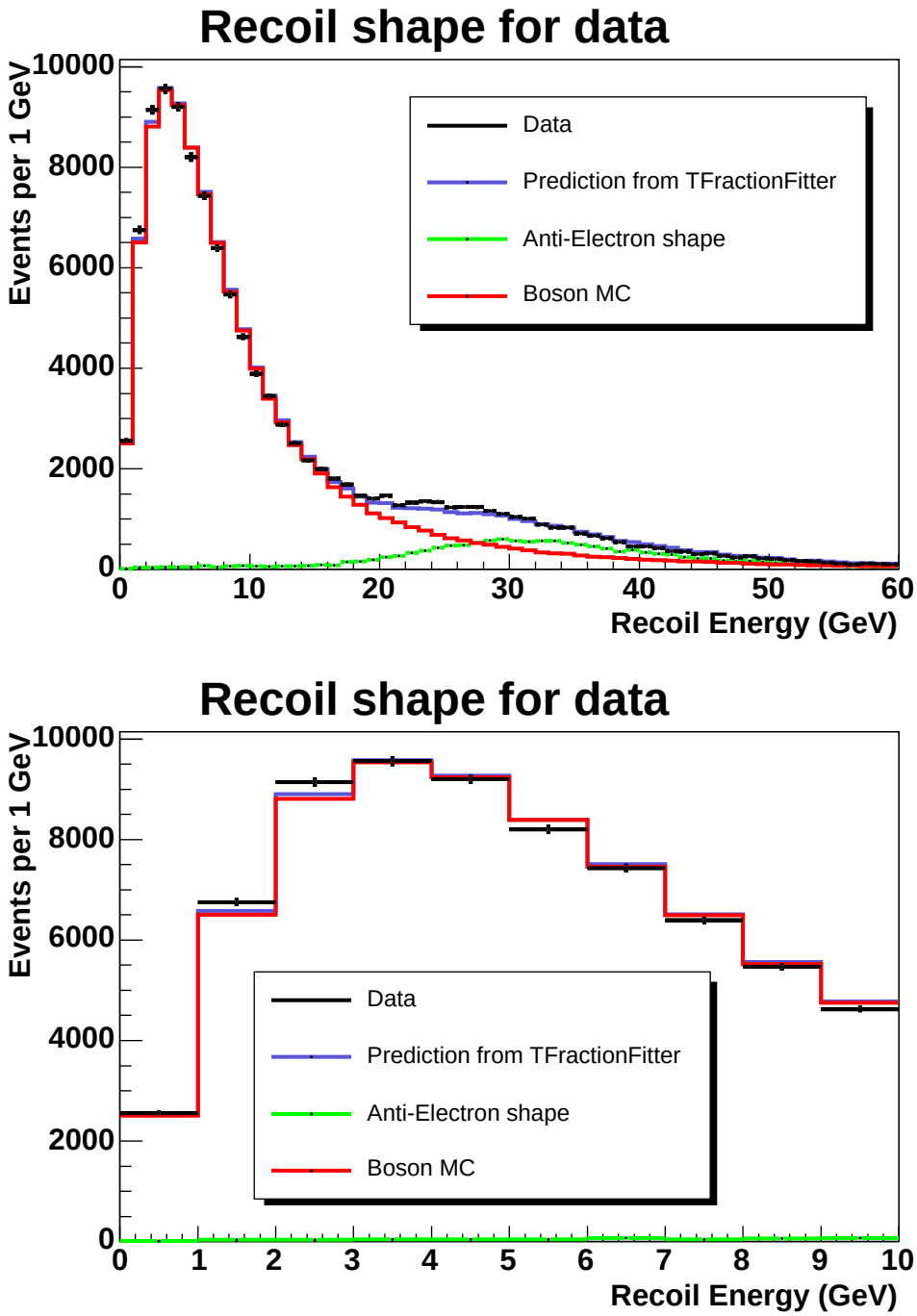

Figure 7.2. Fit to the U distribution to obtain the QCD contribution to the sample. The bottom plot shows the low-U region which is retained for the analysis.

CHAPTER 8

The Likelihood Fit

A maximum likelihood fit is performed to determine the fraction of W's to Z's in the sample. The missing transverse energy ($\not\!\!E_T$) is the variable that is fit, because of the excellent separation between signal and background (Figure 5.4).

8.1 Description of the Fit

A binned maximum likelihood fit takes shape histograms as inputs. The first set of shapes contains one template for each of many processes. The final shape is the data, which is presumed to be a composition of the other input templates, with some fractions. The job of the likelihood fitter is to determine the most likely weight to give to each of the input templates.

For this analysis, the probability density depends on R, on the *relative* acceptance for W and Drell-Yan events (A_W/A_{DY}), on a constant relating the Z cross-section to the Drell-Yan cross section ($C_{Z/DY}$), and on the fraction of QCD background events (f_{QCD}). The probability density is expressed in terms of templates W, Z (for Drell-Yan), and B (for QCD background), all of which are functions of $\not\!\!E_T$:

$$\mathcal{P} = (1 - f_{\mathrm{QCD}})\frac{\mathsf{R}_{\mathrm{eff}}\mathsf{W} + \mathsf{Z}}{\mathsf{R}_{\mathrm{eff}} + 1} + f_{\mathrm{QCD}}B \tag{8.1}$$

where $\mathsf{R}_{\mathrm{eff}} = \mathsf{R} \times (A_W/A_{DY})C_{Z/DY}$. In the actual fit, R is the free parameter and A_W, A_{DY}, $C_{Z/DY}$ and f_{QCD} are fixed parameters. The templates $W(\not\!\!E_T)$ and $Z(\not\!\!E_T)$ are taken from full simulations, and $B(\not\!\!E_T)$ is extracted from data, as described in the previous chapter. All three are normalized to unity for the chosen range of $\not\!\!E_T$, so

that $\mathcal{P}$ is truly a probability density. The range of $\not\!\!E_T$ is $0 \leq \not\!\!E_T < 60$ GeV.

In practice, the negative log-likelihood is used, $L = -\ln(\mathcal{P})$ as it is more convenient numerically. The ROOT routine `TFractionFitter` [16] and our own fitting routine give consistent results.

8.2 Estimated Statistical Error for R

The variation of the negative log-likelihood (L) to set the statistical errors on R. Since L viewed as a function of R is not parabolic, the "negative" and the "positive" errors will be different (asymmetric).

To investigate the statistical error, pseudoexperiments were generated based on the true templates and distributions of the fitted values and the errors were extracted from the likelihood function (Figure 8.1).

8.2.1 The Meaning of R_{eff}

The quantity R_{eff} deserves some discussion. In an ideal situation, R_{eff} would be equal to R. However, for there are some detector-dependent and physics effects which complicate this correspondence. First, the acceptance for $W \to e\nu$ and for $Z \to ee$ is not the same, since a higher fraction of Drell-Yan events passes the cut $E_T > 30$ GeV, and a higher fraction passes the cut $U < 10$ GeV (Table 6.4). Fortunately, our result depends only on the *ratio* of acceptances, A_W/A_{DY}, which is taken from simulations.

The other factor, $C_{Z/DY}$, is needed because the sample includes events which created by Z's, but also indistinguishable events where the two electrons are scattered from a γ^*. These events are off of the Z-peak; since a second electron is not required, cuts around the Z-peak cannot be performed. The templates for the fit include the contribution from the whole Drell-Yan spectrum for $M_{e^+e^-} > 20$ GeV. In fact, the fit is playing the W contribution off the Drell-Yan contribution, as opposed to the pure Z contribution. The fraction of the Drell-Yan template which is attributable to

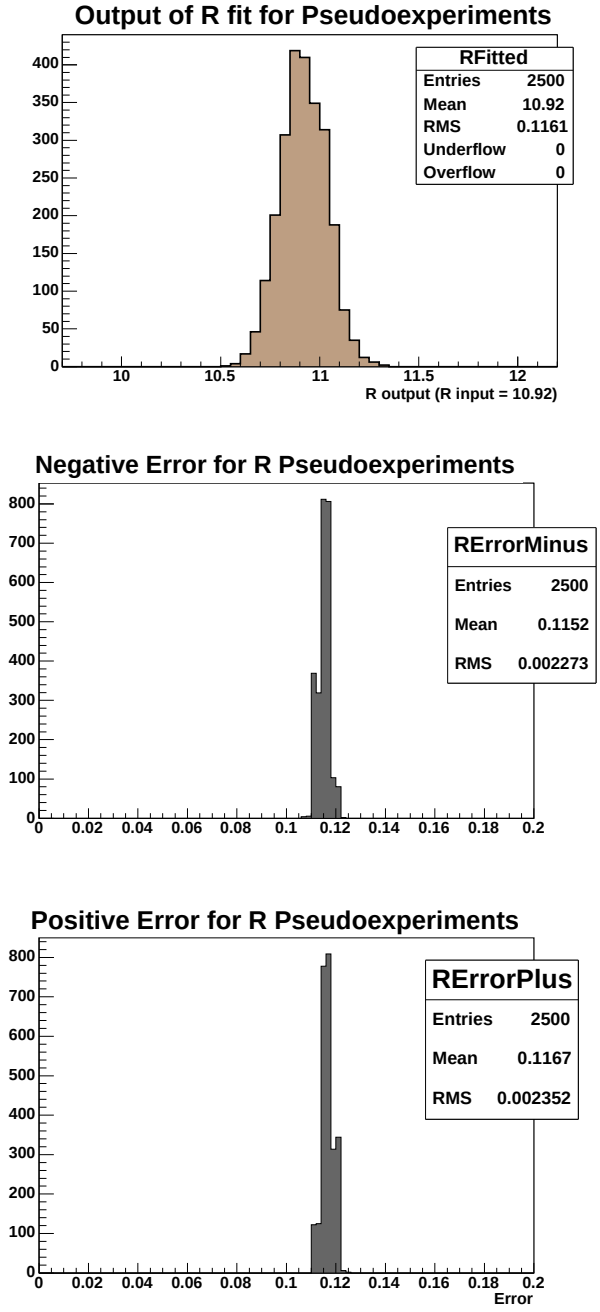

Figure 8.1. These are distributions from 2500 pseudo-experiments of the fitted R value as well as the statistical uncertainties. The statistical uncertainties shown in the bottom two plots were determined for 374 $\text{pb}^{-1}$of available luminosity.

the Z-boson must be taken into account. This amounts to including a factor which is the ratio of cross-sections,

$$C_{Z/DY} = \frac{\int_{20\ \mathrm{GeV}}^{2000\ \mathrm{GeV}} dM\, d\sigma(Z)/dM}{\int_{20\ \mathrm{GeV}}^{2000\ \mathrm{GeV}} dM\, d\sigma(\gamma^*/Z)/dM}$$

which is presently taken from the simulation: $C_{Z/DY} = 0.5122$.

In the future, taking this number from a theoretical calculation would allow better control theoretical uncertainties.

8.3 Combining R^+ and R^-

The electrons and positrons are fit separately, to avoid any kinematic biases that would arise when both have been tagged as tight electrons. The templates for W's and Drell-Yan are independent, but the QCD template is in common. The two measurements, can be combined afterwards, taking into account the correlation between them.

CHAPTER 9

Results

9.1 The Value of R

Given the tuned W and Z templates, and QCD fraction and template, the fit to the data can be performed.

The results from the two fits are:

$$\begin{aligned} \mathsf{R}^{+} &= 10.57 \pm 0.13 \\ \mathsf{R}^{-} &= 10.52 \pm 0.13 \end{aligned}$$

which are consistent and display the expected statistical error for 307. The likelihood scans for both channels are shown in Figure 9.1. The comparison of the fit for the negative leptons to the data is presented in Figure 9.2.

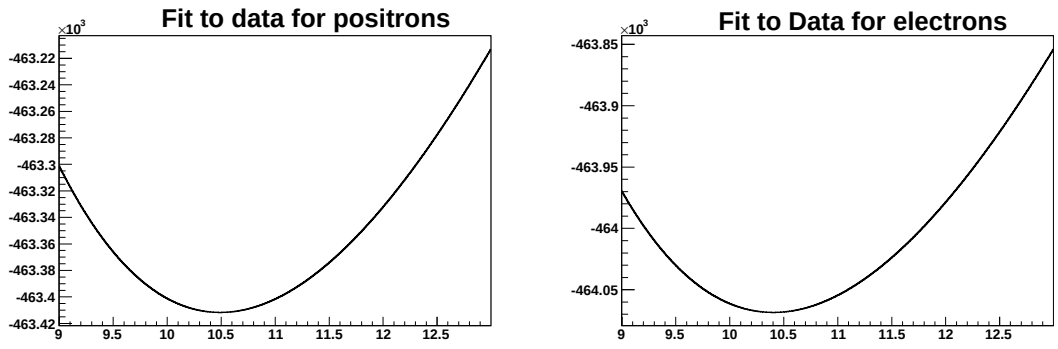

Figure 9.1. Scans of the negative log-likelihood for the e^{+} channel and the e^{-} channel are consistent. The x axis shows the range of Rvalues, while the y axis shows the output of the likelihood procedure.

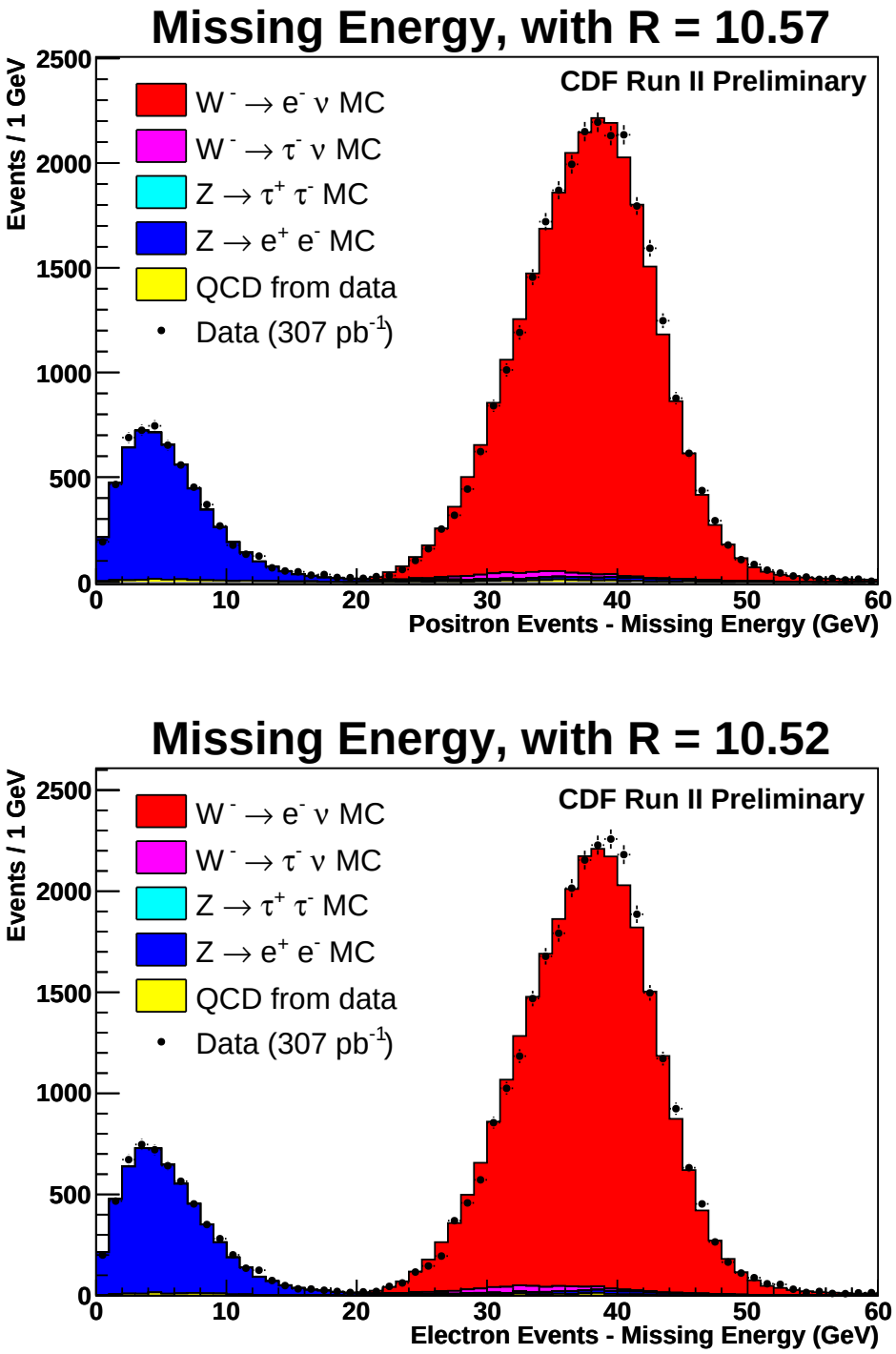

Figure 9.2. The results of the fit to the e^- channel and e^+ channel are compared with the data.

CHAPTER 10

Sources of Systematic Uncertainty

There are several systematic uncertainties that must be considered and evaluated. These are evaluated using pseudoexperiments, in which the quantity in question is varied, and the resulting change in R is observed.

10.1 Tuning of the $\not\!\!E_T$ Distributions

Since the W and Z $\not\!\!E_T$ distributions are so well separated, the exact shape of each template is not crucial. Tuning of the MC shape was performed for a good match, as described in Section 6.4. As an extreme test, pseudo-experiments were generated with the tuned templates and fit them with the raw templates, and found that the fitted value of Rshifts by only 0.5%. Since there is no doubt that the tuned $\not\!\!E_T$ distributions match the data better than the untuned ones, the uncertainty due to the tuning of the $\not\!\!E_T$ templates is no larger than 0.5%.

10.2 Shape of the Templates

Another important aspect of the template shapes to consider is the "tail" of the Z distribution at high $\not\!\!E_T$. About 5% of the Z events fall above $\not\!\!E_T = 20$ GeV. The Z events with relatively large $\not\!\!E_T$ must be well-modeled by the simulation.

Such events occur when the electromagnetic shower that should be produced by the second electron is somehow imperfect or missing. Since the tracking efficiency for high-p_T, isolated electrons is high, the tracking can be used to monitor this effect.

Specifically, searching every event for a second, good-quality track, not associated with the primary tight electron can isolate a sample of Z's. If more than one track has $p_T > 1$ GeV, the one with the highest p_T is considered. The region with $p_T > 20$ GeV is expected to be entirely dominated by Z events, with W events and QCD background events falling mainly in the $p_T < 10$ GeV region. Some standard track-quality cuts are applied as well: $|z_0| < 60$ cm, $|d_0| < 0.2$ cm, $|\eta| < 1$, and at least three axial and two stereo layers with five or more hits. Tracks which are linked to the primary electron are ignored, as are those that fall within a cone of $\Delta R = 0.1$ of the electron track. The calorimeter information associated with the second track is not examined yet; the rate at which that object is missing or flawed is the subject of this study.

Figure 10.1 shows the results of this selection. These distributions are normalized using the most recently measured value, $\mathsf{R} = 10.92$. The plot in the center shows the region where the W's dominate, and indeed the distribution of secondary tracks is well-reproduced by the simulation. The plot on the bottom shows that the Z's dominate for $p_T > 10$ GeV, as expected.

The $\not\!\!E_T$ distribution for those events with $p_T > 20$ GeV is almost pure in Z events, and does exhibit a tail at high-$\not\!\!E_T$ due to failures to measure the shower of the second electron. Figure 10.2 shows the comparison of the simulation to the data. The data are reproduced quite well, without any adjustments. For example, considering the region with $\not\!\!E_T > 20$ GeV, the fraction of events in this region is 0.0687 ± 0.003 in the data, and 0.0727 ± 0.002 in the simulation. The ratio of these two fractions is 0.945 ± 0.005: the simulation reproduces this tail with an accuracy of 5.5%. The induced systematic uncertainty is $\Delta\mathsf{R}/\mathsf{R} = 0.0051$.

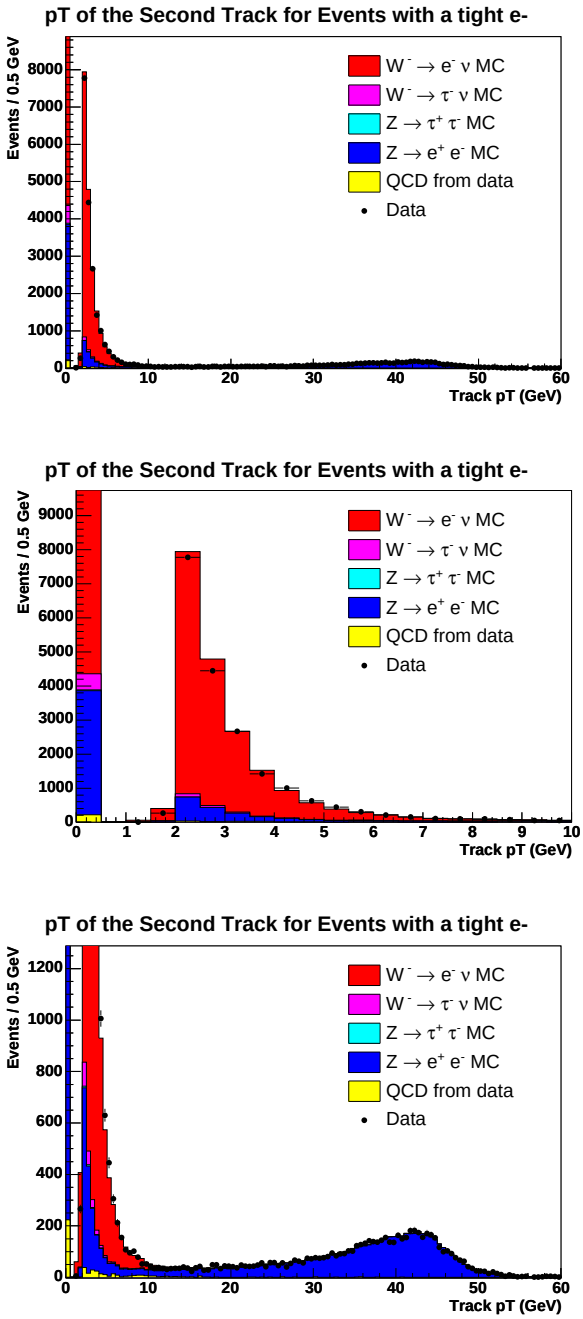

Figure 10.1. The p_T distribution for the most energetic track in an event, aside from the tight electron, is shown.

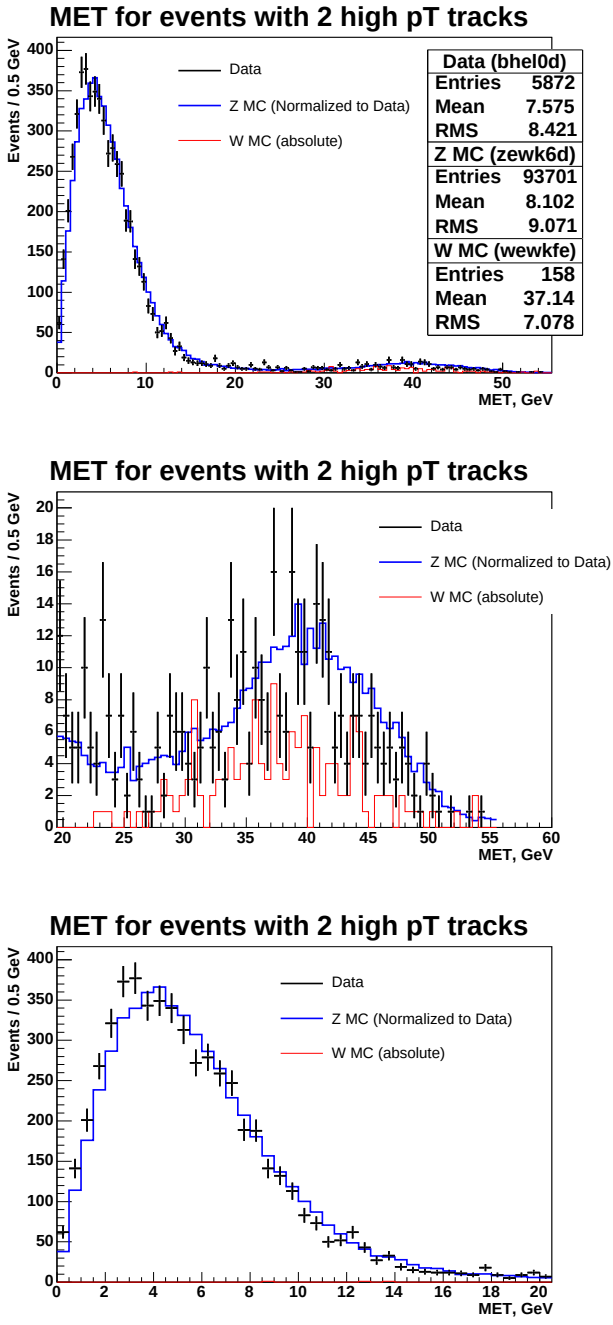

Figure 10.2. The $\not\!\!E_T$ distribution for events with a tight electron plus a second track with $p_T > 20$ GeV. In the middle plot, the red histogram representing W's is about ten times larger than the actual W contribution in this region.

10.3 Backgrounds

The major background comes from QCD multi-jet events, and its contribution is very small number of events, as shown in Section 7.3. The systematic uncertainty for this background is evaluated by means of pseudoexperiments. Sets of pseudodata are generated using the templates for the signal and the background with $f_{\mathrm{QCD}} = 0.00698$. Based on the study of Cooper & Messina, a 25% uncertainty on the background fraction was used. Pseudoexperiments were fit assuming a QCD fraction which is 25% higher, and lower. The resulting shift is $\Delta\mathsf{R}/\mathsf{R} = 0.0098$. This uncertainty on the QCD background fraction is the largest uncertainty for this analysis. With more data and further cross-checks, it should be possible to reduce both the amount of QCD background in the sample, and perhaps the uncertainty on the fraction itself.XS

W and Z events with τ-leptons are treated as signal, but there may be some uncertainty coming from the τ branching ratios. For a window $0 \leq \not\!\!E_T < 60$ GeV, the nominal acceptance for $W \to e\nu$ is $A_W = 0.059485$ after the U cut. For $Z \to ee$, it is $A_{DY} = 0.070410$. The ratio of acceptance for $W^- \to \tau^- \to e^-$ to $W^- \to e^-$ is $f_{W\tau} = 0.01239$, and for Drell-Yan, the corresponding ratio of acceptances is $f_{Z\tau} = 0.00807$. These two ratios of acceptances depend on the τ-branching ratio $Br(\tau \to e\nu) = 0.1784 \pm 0.0006$ which is very well known [39]. Propagating the uncertainty on this branching ratio has a negligible impact on the value of R.

10.4 Acceptance for the U Cut

The U distributions for W and Z events are not exactly the same, as shown in Figure 10.3. Consequently, the cut $U < 10$ GeV eliminates different fractions for events from these two sources. The ratio of the acceptances for this cut is about 0.9, a number obtained from the simulation. If the U distributions are not correctly simulated, however, then this would be the wrong estimate of this ratio of acceptances. This uncertainty is assessed by considering how this ratio A_W/A_{DY} varies with the

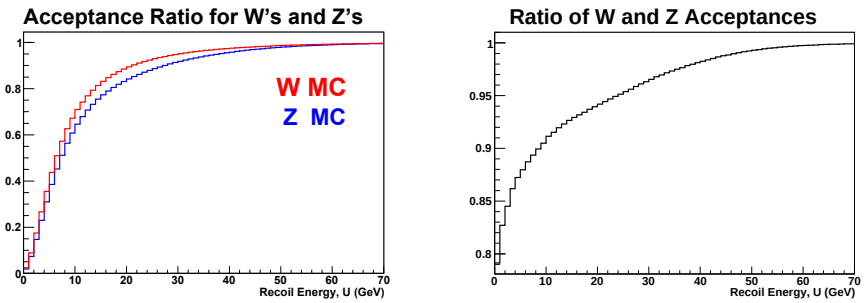

Figure 10.3. The ratio of acceptances A_W/A_{DY} as a function of the cut on U.

cut on U, and the uncertainty on the scale of U. In fact, $\delta(A_W/A_{DY})/\delta U = 0.4\%$ per GeV, and conservatively taking the scale error on U to be $\Delta U = 1$ GeV, a very small uncertainty of 0.4% is the contribution to the acceptance.

10.5 Parton Distribution Functions

The acceptances for $W \to e\nu$ and $Z \to ee$ vary greatly as a function of the vector boson rapidity, y_V. The differential cross sections, $d\sigma/dy_V$, depend on the parton distribution functions (PDF's). For the most part, changes in the W cross section correlate strongly with changes in the Z cross section. However, small differences can be expected, since the W and Z bosons couple to different combinations of quarks. This leads to an uncertainty on the ratio of acceptances, A_W/A_{DY}, which must be quantified. This uncertainty was a major component of the systematic uncertainty from the counting method measurement [8].

Following the method devised for the counting method, the acceptance is obtained from the simulation (Figure 10.4). The shapes are very similar because of the carefully designed event selection in this analysis. A comparison with the acceptance from the counting method event selection is given in Figure 10.5, in which the acceptance functions are represented by the dashed curves. The change in the Z acceptance is dramatic. The degree to which $A_W(y)$ and $A_{DY}(y)$ match is demonstrated in Figure 10.6, which shows the ratio of the two acceptances as a function of y_V.

The acceptances are parameterized as shown in Figure 10.4 with the following analytical functions (here, $y \geq 0$):

$$A_W^e(y) = \begin{cases} A + B(y - 1.0) - C_l \exp(-y/\kappa_l) & \text{for} \quad y < 1.9 \\ (A + B(1.9 - 1.0)) \exp(-(y - 1.9)/\kappa_h) & \text{for} \quad y \geq 1.9 \end{cases} \tag{10.1}$$

for $W \rightarrow e\nu$, and

$$A_{DY}^e(y) = \begin{cases} A + B(y-1) + C(y-1)^2 + D(y-1)^3 & \text{for} \quad y < 1.9 \\ (A + B \cdot 0.9 + C \cdot 0.9^2 + D \cdot 0.9^3) \exp(-(y - 1.9)/\kappa_h) & \text{for} \quad y \geq 1.9 \end{cases} \tag{10.2}$$

where the free parameters are A, B, C, D, C_l, κ_l and κ_h. A good χ^2 was obtained with the parameter values listed in Table 10.1.

With these shape method acceptance functions, the PDF uncertainty was calculated exactly as was done before. The numerical values are summarized in Table 10.2. The shape method uncertainties are smaller than the counting method ones by about a factor of three.

One may have expected a larger improvement in uncertainty on the acceptance ratio. To investigate why the PDF uncertainty remains as large as it is, *exactly* the same functions for W and Z's were tested. The result was $\delta(A_W/A_{DY}) = +0.0030, -0.0053$. This shows that most of the uncertainty is intrinsic, and somehow connected to the way the cross sections vary with the PDF's.

The PDF errors are parameterized by CTEQ into 40 orthogonal "error sets." The CTEQ5L sets are used here. A direct comparison of the contributions to the PDF uncertainty from these sets shows the effect of the change in event selection. The upper plot in Figure 10.7 shows the error contribution for W's (blue) and Z's (red), for the shape method selection (filled circles) and the counting method (hollow circles). Changes in the acceptance usually track between W's and Z's, and they track more closely with the shape method acceptance than with the counting method. The lower plot shows how the ratio of acceptances change from one PDF error set to the

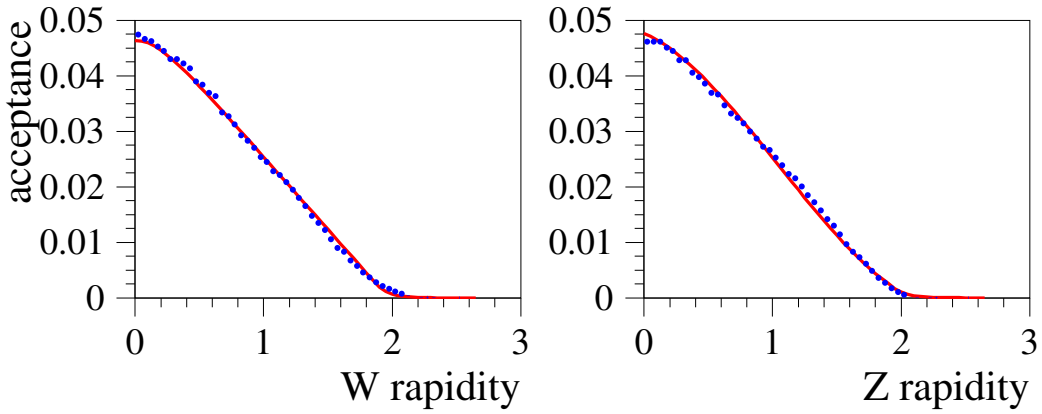

Figure 10.4. The acceptances for W's and γ^*/Z's obtained from the full simulation. The smooth curve shows the parameterization.

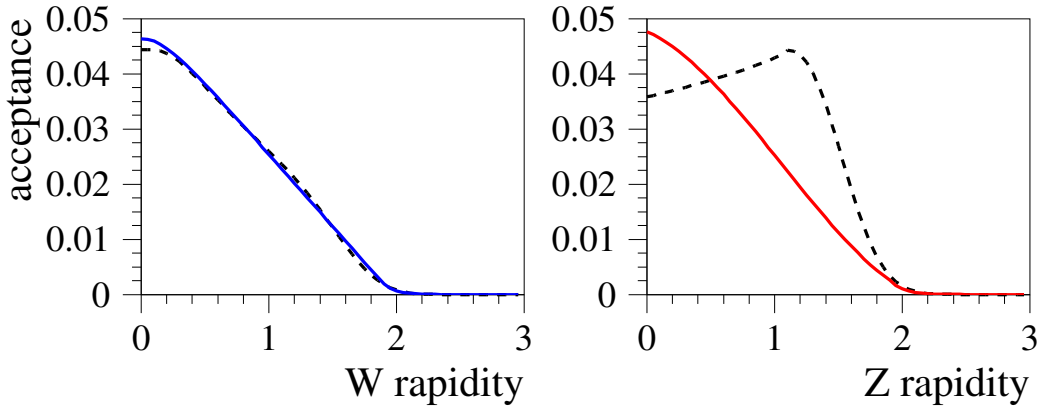

Figure 10.5. A direct comparison of the shape method acceptance function (solid curves) and the counting method ones (dashed curves). The counting method curves have been scaled to match the shape method ones at $y_V = 0$.

next. The filled circles represent the shape result, and they deviate from one less than the counting method results do.

10.6 Theoretical Uncertainties

The cross section used for assessing the acceptance is uncertain due to missing higher orders, and the arbitrariness of the factorization and renormalization scales. Using the calculations from the SLAC group [14], the impact of these uncertainties on the acceptance ratio A_W/A_{DY} was found to be completely negligible (below 0.1%).

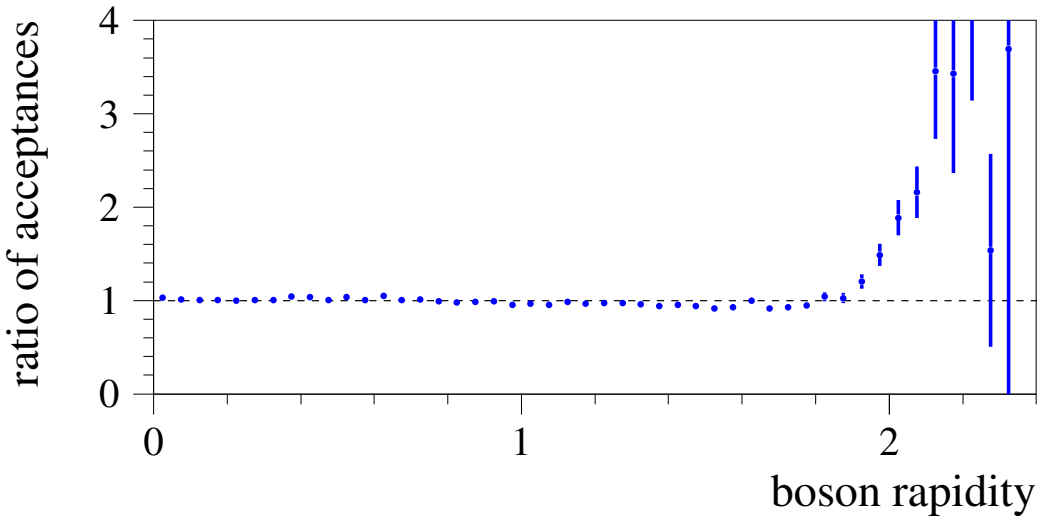

Figure 10.6. The ratio of acceptances $A_{DY}(y_V)/A_W(y_V)$, both from the full simulation (points) and the parameterization (solid line).

parameter	$A_W(y_V)$	$A_{DY}(y_V)$
A	0.02538 ± 0.00008	0.02523 ± 0.00008
B	-0.02610 ± 0.00012	-0.02894 ± 0.00021
C	0	$-(8.951 \pm 1.737) \times 10^{-4}$
D	0	$(5.642 \pm 0.321) \times 10^{-3}$
C_l	$(5.184 \pm 0.428) \times 10^{-3}$	0
κ_l	0.1747 ± 0.0275	0
κ_h	$(9.214 \pm 0.265) \times 10^{-2}$	$(10.77 \pm 0.25) \times 10^{-2}$

Table 10.1. The best fit parameters (Equations (10.1,10.2)) for the W and Z acceptances as a function of y_V

quantity	counting method		shape method	
A_W	$+0.0107$	-0.0130	$+0.0116$	-0.0142
A_{DY}	$+0.0166$	-0.0212	$+0.0102$	-0.0125
A_W/A_{DY}	$+0.0089$	-0.0067	-0.0026	-0.0031

Table 10.2. Relative error on acceptances A_W and A_{DY}, and on their ratio

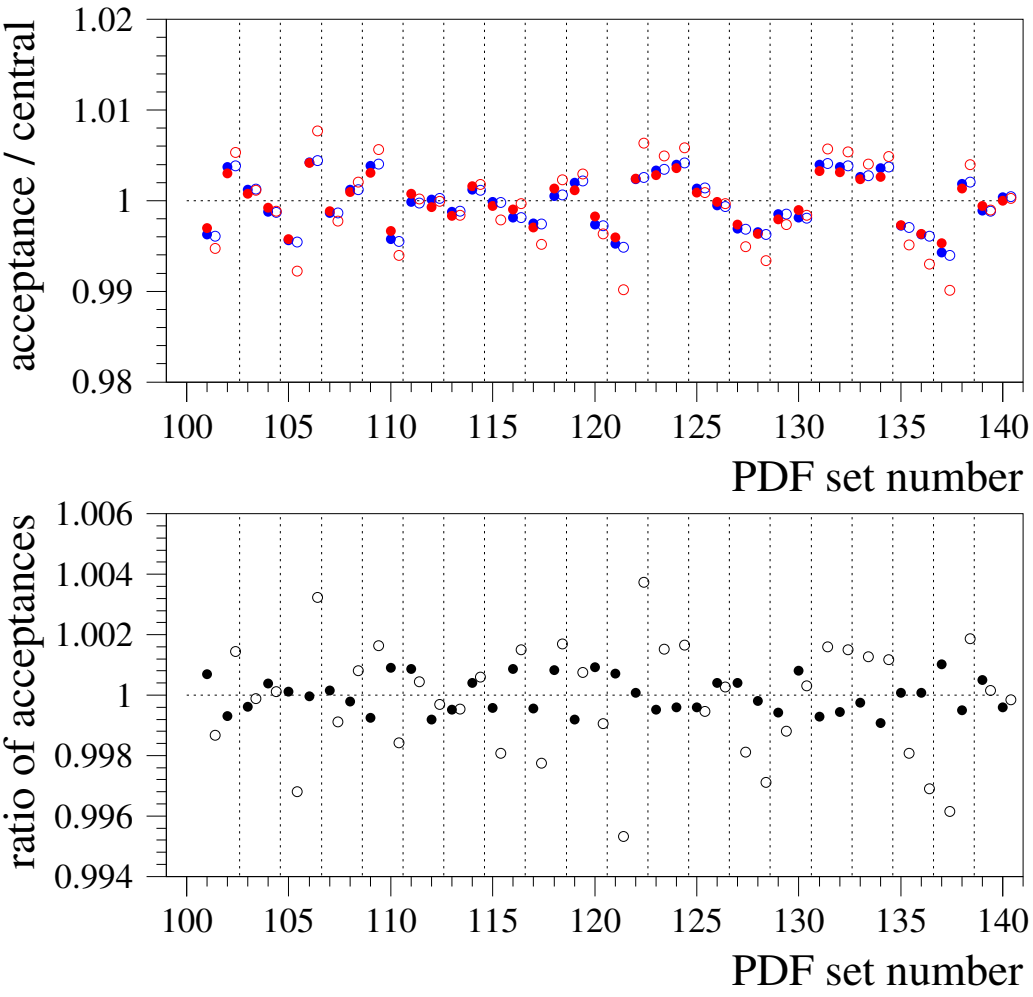

Figure 10.7. Direct comparison of the PDF error contributions from the shape method acceptance functions (filled circles) and the counting method (open circles). The upper plot shows the errors on the acceptances for W's (blue) and Z's (red), while the lower plot shows the errors on the ratio of acceptances.

CHAPTER 11

Summary and Conclusions

The ratio Rhas been measured, using $\mathcal{L} = 307$ pb^{-1} of high-E_T electron data at CDF.

11.0.1 The Value of R

The statistical uncertainty is already below 1% after combining results from the positive and negative channels. Most systematic uncertainties are even smaller. A summary of all uncertainties is given in Table 11.1. The total uncertainty of $\Delta\mathsf{R}/\mathsf{R} = 0.015$, is dominated by the uncertainty on the QCD background fraction, $f_{\rm QCD}$. The result is, therefore:

$$\mathsf{R}_e = 10.55 \pm 0.09(\text{stat}) \pm 0.12(\text{syst}) \quad . \tag{11.1}$$

The previous result for electrons was $\mathsf{R}_e = 10.82 \pm 0.18(\text{stat}) \pm 0.16(\text{syst})$. Combining the electron and muon channels yielded $\mathsf{R} = 10.92 \pm 0.15 \pm 0.14$ [8].

This extraction of the physics quantities closely follows the work done previously [8].

11.0.2 The $W \to \ell\nu$ Branching Ratio

In order to obtain the Br($W \to \ell\nu$), the input values are the leptonic Z branching ratio and the ratio of cross sections. For the first, the PDG value [39] is $Br(Z \to \ell^+\ell^-) = 0.033658 \pm 0.000023$. The inclusive cross sections have been calculated at NNLO [14]. A computation of this ratio using these programs was carried out [33]

category	$\Delta R/R$
statistical	0.009
QCD background	0.010
high-$\not\!\!E_T$ tail of the Drell-Yan template	0.005
acceptance for the U cut	0.004
impact of PDF's on acceptance	0.003
tuning of $\not\!\!E_T$ templates	0.001
τ leptonic branching ratios	negl.
theoretical uncertainties	negl.
all systematics	0.012
systematics and statistical	0.015

Table 11.1. The uncertainties are given as $\Delta R/R$.

for the previous CDF publication [8], with the result

$$\frac{\sigma_W}{\sigma_Z} = 3.370 \pm 0.006 \quad . \tag{11.2}$$

A significant portion of the uncertainty on the ratio of cross sections in Equation (11.2) comes from the PDF's, so when extracting the leptonic W branching ratio, the correlations in the PDF uncertainty for the cross sections and for the acceptances in this analysis, A_W and A_Z, must be considered. It suffices to find the uncertainty on the combination $(\sigma_W/A_W)/(\sigma_Z/A_Z)$. The PDF uncertainty on this quantity is 0.4%.

Inverting Equation (3.14) and using the values for the ratio of cross sections Equation (11.2), the Z leptonic branching ratio, and R (11.1):

$$Br(W \to \ell\nu) = R \cdot \frac{\sigma_Z}{\sigma_W} Br(Z \to \ell^+\ell^-) = 0.1054 \pm 0.0016 \quad . \tag{11.3}$$

This value can be compared to the current one from the PDG [39], which is

$$Br(W \to \ell\nu) = 0.1080 \pm 0.0009 \quad .$$

The Standard Model value is $Br(W \to \ell\nu) = 0.1082 \pm 0.0002$.

11.0.3 The Total W Width

Given $Br(W \to \ell\nu)$, the total W width is determined, given a value for the leptonic partial width. Taking $\Gamma(W \to \ell\nu) = 226.4 \pm 0.4$ MeV [39]:

$$\Gamma_W^{\rm tot} = 2148 \pm 32 \text{ MeV} \quad .$$

This can be compared to $\Gamma_W^{\rm tot} = 2091.2 \pm 2.5$ MeV in the Standard Model, and the current world average $\Gamma_W^{\rm tot} = 2138 \pm 44$ MeV [39].

11.0.4 The CKM Matrix Element V_{cs}

In the SM, the total W width is a sum over partial widths (Γ_W^0) for leptons and for quarks, and the latter involves a sum over certain CKM matrix elements:

$$\Gamma_W = 3\Gamma_W^0 + 3\left(1 + \frac{\alpha_s}{\pi} + 1.409(\frac{\alpha_s}{\pi})^2 - 12.77(\frac{\alpha_s}{\pi})^3\right) \sum_{\text{[no top]}} |V_{qq'}|^2\, \Gamma_W^0 \quad . \qquad (11.4)$$

Only the first two rows of the CKM matrix contribute as decays to the top quark are kinematically forbidden. Thus the relevant CKM matrix elements are $V_{\rm ud}$, $V_{\rm us}$, $V_{\rm cd}$, $V_{\rm cs}$, $V_{\rm ub}$ and $V_{\rm cb}$. Of these, V_{cs} contributes the largest uncertainty. This indirect measurement of Γ_W can be used as a constraint on V_{cs}, given the best world measurements of all the other CKM matrix elements. Therefore,

$$|V_{cs}| = 1.008 \pm 0.029$$

given $\alpha_s = 0.120$ and $\Gamma_W^0 = 226.4$ MeV. The value in the Review of Particle Properties is $V_{cs} = 0.996 \pm 0.013$ [39].

For a more detailed discussion, see the review article by Peter Renton [32].

11.1 Combination with the Muon Channel

The electron analysis presented here has been designed to be combined with a muon measurement. Just as the counting method and shape method cross-check one an-

other, the electron and muon measurements provide cross-checks and further tests of the Standard Model.

For the muon shape analysis in progress, the strategy has been to fit the p_T spectrum, rather than the $\not\!\!E_T$ spectrum (Figure 11.1). The $\not\!\!E_T$ is more complicated in the muon case than in the electron case because lost muons mimic $\not\!\!E_T$. The recoil and the missing energy must both be corrected for every muon in the event. In the electron case, unidentified electrons still deposit energy in the calorimeter, so they need not be identified to correct the $\not\!\!E_T$.

The W and Z shapes are fairly similar for the p_T fit, so it has less statistical power, but the p_T fit for muons has a distinct advantage for the QCD background. The background shape falls off as a function of p_T, so it has a completely different shape than the two signals. Cutting very tightly on the p_T can all but eliminate the background.

For electrons, the analogous procedure would be to fit the E_T. This was investigated, but the E_T scale systematic uncertainty was far above the percent level. Unless the E_T scale of the calorimeter can be determined very precisely, the $\not\!\!E_T$ fit is a better choice for electrons.

11.2 Future Prospects

The shape method provides a new window into electroweak physics at CDF. By treating W and Z events in a similar way, new systematic uncertainties cancel in the R ratio measurement, allowing a path to the most precise measurement of the W width (Figure 11.2). The largest uncertainties in the counting method were difficult, if not impossible, to reduce in the 72 pb^{-1}analysis. With the shape method, the 4-8 $\text{fb}^{-1}$of CDF data should be able to be examined in greater detail. The largest uncertainty in the current shape analysis comes from the QCD background. As more data is integrated, this background can be studied in greater detail. New cuts on the

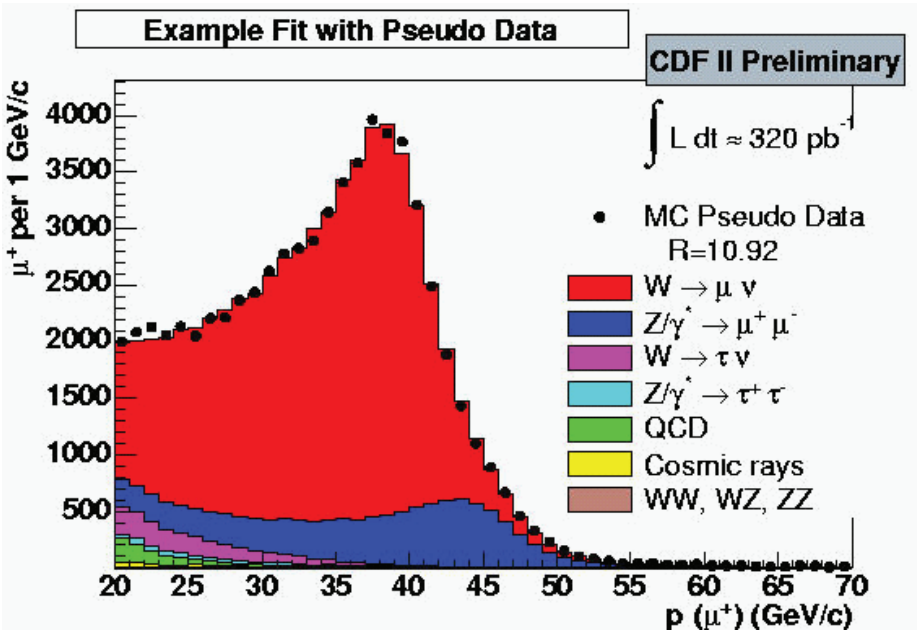

Figure 11.1. The shape method p_T fit for muons is shown, with pseudodata for the black points. The discrimination in the fit comes from the different W ad Z peaks at approximately half the W mass and half the Z mass.

events may reduce the background further, and higher statistics samples will allow a more precise determination of the background fraction.

The shape method and counting method, the electron channel and muon channel, and the $\not\!\!E_T$ fit and p_T fit all provide different ways of looking at the large number of W and Z events produced by the Tevatron. With all of this information, the electroweak force carriers and the Standard Model can be understood at new levels of precision.

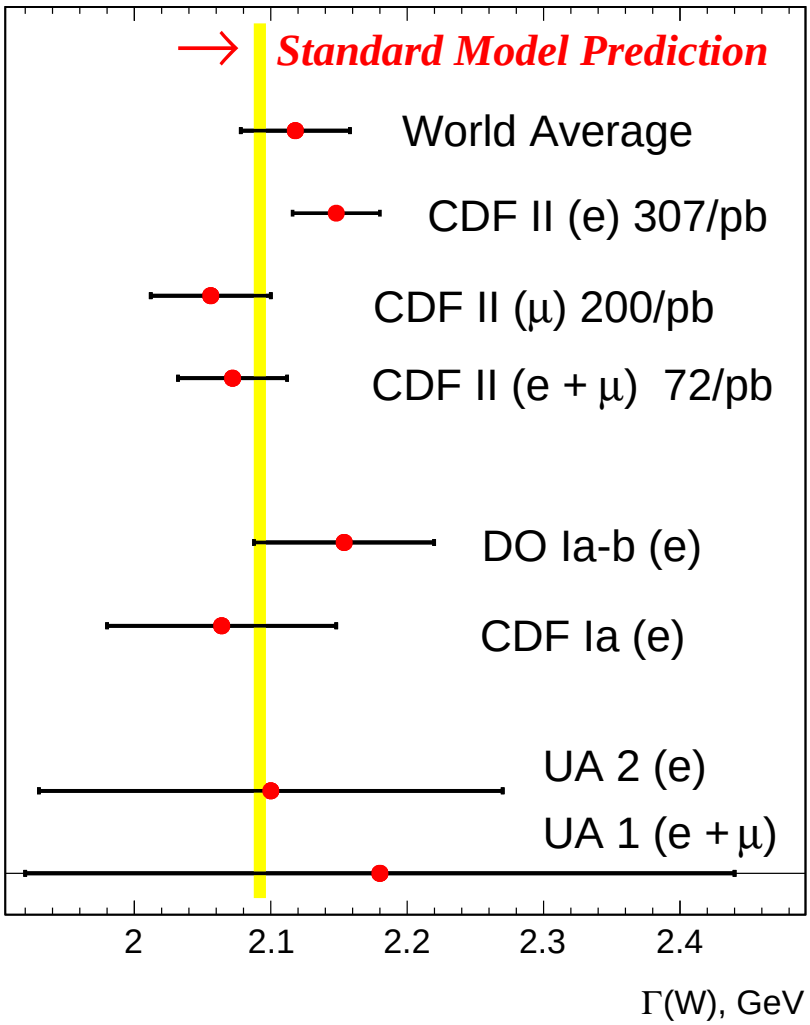

Figure 11.2. This measurement (307 pb^{-1}) is compared with past measurements of the W width.

BIBLIOGRAPHY

[1] S. Abachi et al. *Phys. Rev. Lett.*, 75:1456, 1995.

[2] B. Abbott et al. *Phys. Rev.*, D61:072001, 2000.

[3] Abbott, B. and others. Measurement of W and Z boson production cross sections. *Phys. Rev.*, D60:052003, 1999.

[4] F. Abe et al. *Phys. Rev. Lett.*, 73:220, 1994.

[5] F. Abe et al. *Phys. Rev.*, D52:2624, 1995.

[6] F. Abe et al. Measurement of $\sigma \cdot B(W \rightarrow e\nu)$ and $\sigma \cdot B(Z\ 0 \rightarrow e\ + e\ -)$ in $p\overline{p}$ collisions at $\sqrt{s} = 1.8$ TeV. *Phys. Rev. Lett.*, 76:3070–3075, 1996.

[7] Abe, F. and others. Measurement of Z0 and Drell-Yan production cross section using dimuons in anti-p p collisions at s**(1/2) = 1.8- TeV. *Phys. Rev.*, D59:052002, 1999.

[8] Acosta, D. and others. First measurements of inclusive W and Z cross sections from Run II of the Tevatron collider. 2004.

[9] Affolder, Anthony A. and others. CDF central outer tracker. *Nucl. Instrum. Meth.*, A526:249–299, 2004.

[10] Agostinelli, S. and others. GEANT4: A simulation toolkit. *Nucl. Instr. Meth.*, A506:250–303, 2003.

[11] C. Albajar et al. Measurement of the ratio R=$\sigma_W Br(\mathrm{W} \rightarrow \mu\nu)/\sigma_Z Br(\mathrm{Z}^0 \rightarrow \mu\mu)$ and $\Gamma_{\mathrm{W}}^{tot}$ at the CERN proton-antiproton collider. *Phys. Lett.*, B253:503, 1991.

[12] J. Alitti et al. Measurement of the w and z production cross-sections at the cern $\mathrm{p\bar{p}}$ collider. *Z. Phys*, C47:11–22, 1990.

[13] Amidei, D. et al. The CDF-II detector: Technical Design Report.

[14] Anastasiou, Charalampos and Dixon, Lance and Melnikov, Kirill and Petriello, Frank. High-precision QCD at hadron colliders: Electroweak gauge boson rapidity distributions at NNLO. *Phys. Rev.*, D69:094008, 2004.

[15] Anderson, M.H., J. R. Ensher, M. R. Matthews, C. E. Wieman, E. A. Cornell. Observation of Bose-Einstein Condensation in a Dilute Atomic Vapor. *Science*, 269(5221):198–201, 1995.

[16] R. Barlow and C. Beeston. *Comp. Phys. Comm.*, 77:219–228, 1993.

[17] Brun, R. and Hagelberg, R. and Hansroul, M. and Lassalle, J. C. GEANT: Simulation Program for Particle Physics Experiments. User Guide and Reference Manual.

[18] CDF Collaboration. First measurements of inclusive W and Z cross sections from Run II of the Tevatron collider - submitted. *PRD*, 2004.

[19] B. Cooper and A. Messina. Estimation of the Background to W $\rightarrow$ ev + n Jet Events. 2005.

[20] DONUT Collaboration. Observation of tau neutrino interactions. *Physics Letters B*, 2001.

[21] R. K. Ellis, W. J. Stirling, and B. R. Webber. *QCD and Collider Physics*. Cambridge University Press, 1996.

[22] Feynman, Richard and Leighton, Robert B. and Sands, Matthew L. *The Feynman Lectures on Physics*. Addison-Wesley, 1963. 3 volumes.

[23] Field, Rick and Group, R. Craig. PYTHIA Tune A, HERWIG, and JIMMY in Run 2 at CDF. *Proceedings of the HERA-LHC workshops*, 2005.

[24] S. Glashow. *Nucl. Phys.*, 22:579, 1961.

[25] G. L. Kane. *Modern Elementary Particle Physics*. Westview Press, 2001.

[26] J. Kang. W Cross Section for 193 pb^{-1}, 2004.

[27] Lai, H. L. and others. Global QCD analysis of parton structure of the nucleon: CTEQ5 parton distributions. *Eur. Phys. J.*, C12:375–392, 2000.

[28] G. Manca. A Measurement of the Ratio, R, in $p\overline{p}$ Collisions at $\sqrt{s} = 1.96$ TeV, 2003.

[29] Martin, A. D. and Roberts, R. G. and Stirling, W. J. and Thorne, R. S. MRST partons and uncertainties. 2003.

[30] Particle Data Group. *"The Particle Adventure"*. Available online at http://www.particleadventure.org.

[31] Perricone, Mike. Hitting the broad side of a (classified) barn. *Symmetry Magazine*, 03(01), 2006.

[32] Renton, P B. Precision electroweak tests of the standard model. *Rept. Prog. Phys.*, 65:1271–1330, 2002.

[33] Sakumoto, Willis. W/Z Cross Section Predictions for $\sqrt{s} = 1$ TeV.96 TeV.

[34] A. Salam. Elementary Particle Theory. ed. N.Svartholm (Stockholm:Almqvist,1968), page 367, 1968.

[35] Sjöstrand, Torbjorn and others. High-energy-physics event generation with PYTHIA 6.1. *Comput. Phys. Commun.*, 135:238–259, 2001.

[36] Takeuchi, Tatsu and Grant, Aaron K. and Rosner, Jonathan L. An analysis of nonoblique corrections to the $Zb\bar{b}$ vertex. 1994.

[37] Tevatron Electroweak Working Group. Combination of CDF and D0 results on the W-boson width. 2005.

[38] A. Varganov. The Production Cross Sections of the Weak Vector Bosons in $p\bar{p}$ Collisions at $\sqrt{s}$=1.96 TeV and a Measurement of the W Boson Decay Width, 2004.

[39] W.-M. Yao et al. The Review of Particle Physics. *Journal of Physics*, G 33, 1, 2006.

[40] R. Wallny. The CDF Run II Silicon Detector. *CDF Detector Lecture Series*, 2006.

[41] S. Weinberg. *Phys. Rev. Lett.*, 19:1264, 1967.

[42] Wilson, Robert Rathbun. *Starting Fermilab.* Golden Book Collection. Fermi National Accelerator Laboratory, 1992. Available online at http://history.fnal.gov/GoldenBooks/goldenbooks.html.